Ministero dell'Istruzione, dell'Università e della Ricerca

UNIVERSITY OF SALERNO

Department of Civil Engineering

Doctoral thesis
in

RISK AND SUSTAINABILITY IN CIVIL, ARCHITECTURE AND ENVIRONMENTAL ENGINEERING SYSTEMS

XXXI Cycle (2015-2018)

Experimental investigations on granular flows

Luigi Carleo

Supervisor
Prof. Maria Nicolina Papa
Co-Supervisor
Eng. Luca Sarno

Coordinator
Prof. Fernando Fraternali

Index

Abstract

Granular flows, such as debris avalanches, debris flows and rock avalanches, involve the rapid motion of granular mixtures consisting of sediments, water and air. They occur on steep slopes and in the hydrographic network and can affect anthropized areas causing damage to buildings, roads and, in the worst case, loss of human lives.

Investigating on the initiation mechanism and on the rheological behavior of granular flows is essential in the hydrogeological risk assessment and mitigation. The study of the triggering phase of granular flows is fundamental for estimating the amount of sediments involved in the flowing mass and predicting their occurrence. Rainfall plays a crucial role in the slope stability since it can trigger granular flows through different mechanisms. The knowledge of the granular flow dynamics allows estimating both the run-out distances and the impact forces of such flows. The dynamics strongly depends on the characteristics of the sediments and their concentration in the granular mixture. The boundaries influence the granular flow dynamics inducing the onset of different dissipation mechanisms within the granular body. To date, the effects of the boundaries on the dynamics of granular flows are not completely understood. Furthermore, a unified rheological law, capable to describe all the different dissipation mechanisms, is still an open problem.

This PhD thesis mainly focused on the effects of the boundaries on the dynamics of chute dry granular flows at the laboratory scale. Optical

techniques were employed to study flows not disturbed by measurement devices. The dynamics was investigated through velocity and volume fraction measurements taken both at the sidewall and at the free surface. The open source software PIVlab [Thielicke and Stamhuis, *Journal of Open Research Software*, 2014] was used to measure velocity at the sidewall and at the free surface while the stochastic-optical method [Sarno et al., *Granular Matter*, 2016], developed at the Laboratorio di IDraulica Ambientale e Marittima, (LIDAM), University of Salerno, was employed to get near-wall volume fraction measurements. Several open channel experiments were performed and different mass flow rates were analyzed. The experiments can be divided in two groups: experiments over fixed bed and experiments over erodible bed. The first group of experiments was performed in the same channel to investigate on the effects of both the basal roughness and the inclination angle of the channel in steady flow condition. Five different fixed basal surfaces and two inclination angles of the channel were studied. The second group of experiments was performed over the erodible/loose bed to study the effect of the channel width in uniform flow condition. Two channels with two different widths were employed.

Different layers can be identified: an upper collisional layer, characterized by a decreasing trend of the volume fraction while going toward the free surface; a central frictional-collisional layer, where volume fraction reaches an approximately constant value and about the loose random packing of the granular material (≈0.6); a lower layer, only observed in case of fixed bed, where volume fraction is lower than 0.6 due to the

presence of the fixed bed. Three main shapes of the longitudinal velocity profiles were identified: Bagnold-like, linear and exponential. In the experiments over the fixed bed, the occurrence of such shapes depends on the resistance exerted by the sidewalls, the normal stresses and the kinematic boundary conditions observed at the bed. Such shapes may coexist in a stratified way. This indicates that, in a granular flow, different flow regimes can take place. In the experiments over erodible bed, it was found that, by changing the mass flow rate, namely the flow depth, the velocity profiles collapse into a unique master curve. The inclination angle of the free surface is the only quantity that changes with the mass flow rate and, thus, it could reflect the dissipative forces, namely the active forces, that take place in a granular flow over erodible bed. In both the experimental campaigns over fixed bed and erodible bed, if the flow rate is high enough, a weak secondary circulation takes place within the cross section. Therefore, granular flows should be considered weakly three-dimensional.

The second part of this research was devoted to the study of granular flows at catchment scale. It was conducted during my research period abroad in collaboration with Prof. Marcel Hürlimann (Universitat Politècnica de Catalunya, Barcelona). The goal was to detect and classify all the processes occurred in the Rebaixader catchment (South Central Pyrenees) in 2017. In this way, it was possible to properly distinguish the triggering rainfalls. Data from the monitoring stations installed in the propagation zone (FLOW station) and in the triggering zone (INF station) were analyzed.

Abstract

A classification system, based on ground vibration and flow depth measurements recorded by the FLOW station, was proposed. Three types of process were identified: debris flow processes, fluvial sediment transport processes and erosion and accumulation processes at the end of the scarp. Pore water pressure and volumetric water content measurements, recorded by the INF station, were analysed. Not a clear relation between triggering rainfalls and infiltration data was found due to the strong heterogeneity of the soil and the small observation period.

1. Introduction

Geophysical flows, such as debris avalanches, debris flows and rock avalanches, involve the rapid motion of granular mixtures. Generally speaking, the flowing mass is a triphasic medium consisting of water, sediment and air that propagate along steep slopes and in the hydrographic network due to the gravity. Granular flows can affect anthropized areas causing damage to buildings and loss of human lives. Due to the strong unpredictability and the high amounts of involved momentum, they are high hazardous phenomena and, thus, object of study in the hydrogeological risk assessment and mitigation.

The development of a granular flow involves three zones. The triggering zone is the area characterized by the highest slope angles where the solid material loses stability and starts flowing downstream. In the propagation zone, the flowing mass reaches the highest velocities. In the deposition zone, the granular mixture stops thanks to much smaller inclination angles and the possibility of expanding.

The study of the triggering phase is fundamental for both predicting the occurrence of the process and estimate the amount of sediment which can be involved in flowing mass. The susceptibility of an area to the triggering of granular flows depends on many predisposing factors such as the inclination angle of the triggering area, the soil stratification, the presence of vegetation etc. The main contribution to the slope stability is given by the shear stress offered by the soil (Schofield and Wroth 1968; Lambe and Whitman 1969;

Savage and Baum 2005). In mountain environments, rainfall is one of the most important triggering factor that influences the slope stability (Wieczorek and Glade 2005). In saturated soil, the infiltrated rainfall can induce a decreasing of the resistance forces with respect to the driving forces (Savage and Baum 2005). In unsaturated soil, the further resistance due to the capillarity and absorption phenomena (Fredlund et al. 1978; Rahardjo et al. 1995) vanishes when the volumetric water content increases (Krahn et al. 1989; Ng and Shi 1998). In Literature, two main debris flow triggering mechanisms were identified: mobilization from landslides (Iverson et al. 1997) and progressive entrainment of sediment due to surface runoff (Tognacca et al. 2000; Coe et al. 2008; Gregoretti and Fontana 2008). The knowledge of the infiltration mechanisms of the rainfall is fundamental to understand the main triggering mechanisms of a granular flow.

The study of the propagation phase mainly deals with the resistance mechanisms within the granular mixture. In fact, the presence of a solid component induces different dissipation mechanisms with respect to a monophasic fluid which strongly depend on the concentration of sediments and their physical properties, and on the characteristics of the interstitial fluid (Laigle and Coussot 1997; Coussot et al. 1998; Rickenmann et al. 2006). In case of dry granular flows, or when the presence of an interstitial fluid can be neglected to a leading order approximation (e.g. the stony-type debris flows), the main resistance mechanisms are due to the intergranular actions, namely collisions and friction among the grains. In Literature, different flow regimes were identified depending on the occurrence of the prevailing dissipation mechanism. In the *frictional regime*, solid

concentration is high and the shear rate is very low (Savage and Hutter 1989; Gray et al. 1999). The stresses are mainly transmitted by enduring contacts among the particles. The study of this regime is carried out according to the theories of soil mechanics (Lambe and Whitman 1969; Savage and Hutter 1989). On the opposite, in the *collisional regime*, the resistances are mainly due to collisions among the grains. One of the pioneer theories that aimed to describe the collisional regime was proposed by Bagnold (1954). He found that the stresses were directly proportional to the square of the shear rate. Over the years, new theories, based on different approach and attempting to describe different regimes, have been developed. The *kinetic theories*, for example, are based on the analogy between the motions of the particles and of the gases molecules (Jenkins e Savage 1983; Lun et al. 1984). An intermediate *dense regime* takes place when both friction and collisions occur in the granular flow. The μ(I) rheology (GDR MiDi 2004, Jop et al. 2005), which is one of the most popular rheology employed to describe the dense regime, provides a relation in which the shear stress is proportional to the normal stress by a friction coefficient depending on a dimensionless quantity, the Inertial Number. It expresses the relative importance of the shear deformation and the confinement effect of the normal pressures. Other works highlighted that in the dense regime, force networks may occur and, thus, a different approach should be used to describe the momentum exchanges within the granular body. For example, Mills et al. (1999) proposed a non-local rheology in which force chains are capable of carrying momentum.

Different works highlighted that dry granular flows may exhibit different

flow regimes (Komatsu et al. 2001; Armanini et al. 2005; Doyle et al. 2010; Sarno et al. 2014; Sarno et al. 2018a) and their occurrence in strongly influenced by the effect of the sidewall resistances, normal pressures and the basal roughness (Taberlet et al. 2003; Jop et al. 2005; Sarno et al. 2018a). To date, a unified rheology, capable of describing all the complex resistance mechanisms, is still lacking. Moreover, the effects of the boundaries on the granular flow dynamics are not completely understood.

At laboratory scale, the study of the rheological behavior of granular flows can be addressed by employing different laboratory setups: the annual shear cell (Mueth et al. 2000; GDR MiDi 2004), the rotating drum (Bonamy et al., 2002), the heap flow (Komatsu et al., 2001) and the inclined chute (Pouliquen 1999; Ancey 2001). Velocity and volume fraction field are usually investigated to study the dynamics of such flows.

At catchment scale, experimental investigations can be conducted by installing monitoring stations (Berti et al. 2000; Marchi et al. 2002; Coe et al. 2008; Hürlimann et al. 2011, Bel et al. 2017). The study of the propagation phase of the granular flows can be faced by analyzing measurements of flow depth and ground vibrations produced by the passing mass. The study of the triggering mechanisms of granular flows can be performed by analyzing infiltration measurements taken in the initiation area. Rainfall data are fundamental and are usually recorded by rain gauges.

This work is mainly devoted to study the effects of the boundaries on the dynamics of chute dry granular flows at laboratory scale. Specifically, main goal was to analyze the influence of the inclination angle of the chute, the basal roughness, the channel width, normal pressures and sidewall friction

in order to provide information both on the velocity and volume fraction fields. Several experimental campaigns were performed. Velocity and volume fraction measurements were taken at the boundaries. Optical measurement techniques were employed in order to study flows not disturbed by the measurement devices. The experiments can be divided in two groups: experiments over fixed bed and experiments over erodible bed. The former configuration was used to study the influence of both the basal roughness and the inclination angle of the chute on the velocity and volume fraction fields. Five different rough fixed basal surfaces and two inclination angles were studied both higher than the internal angle of friction of the granular material. The erodible bed configuration permitted investigating uniform flow condition (Taberlet et al. 2003). The effect of the channel width on the granular flow dynamics was studied in this configuration. In both the configurations several runs were performed by varying the mass flow rate, namely the flow depth, so one can study the influence of both normal pressures and sidewall friction.

The second and smaller part of this Ph.D. research was devoted to the study of granular flows at catchment scale. This study arises from my personal need to observe the environment in which they occur and propagate and it was conducted during the short research period abroad at the Universitat Politècnica de Catalunya (Barcelona) in collaboration with Prof. Marcel Hürlimann. Both the propagation phase and the initiation phase were investigated. The study was devoted to the analysis of the data from the monitoring stations installed in the Rebaixader catchment (South Central Pyrenees), already known for the high debris flow activity (Hürlimann et al.,

2014). Main goal of this part of the research was to detect and classify all the processes occurred in 2017 in this catchment through ground vibration and flow depth measurements. This is fundamental for properly distinguishing the triggering rainfalls. Moreover, rainfall and infiltration data were analyzed in order to characterize the triggering rainfalls and find a relation between the increasing of the pore pressure and the occurrence of a process.

The thesis is organized in 10 chapters. The Chapt. 2 introduces the triggering and the dynamic problems of granular flows. The main flow regimes will be illustrated and discussed. Particular attention will be dedicated to illustrate the configuration used in laboratory for studying the dynamics of granular flows and the techniques used for measuring velocity and volume fraction. Chapt. 3, 4, 5, 6 and 7 deal with the laboratory investigations. In the Chapt. 3, the experimental apparatus and the techniques employed for measuring velocity and volume fraction will be carefully described. In Chapt. 4 and 5 results of the experimental campaigns performed on the fixed bed and on the erodible bed, respectively, will be discussed in details. In Chapt. 6, a discussion about the results of the experimental campaigns will be presented. In Chap. 7 an application of the $\mu(I)$ rheology to interpreter the laboratory results is shown. Chapt. 8 and Chapt. 9 deal with the field investigations. In Chapt. 8 the characteristics of the study site and the description of the monitoring system will be presented. Results of the analysis of the monitoring data will be shown in Chapt. 9. In Chapt. 10, the conclusions of the entire Ph.D. dissertation are summarized.

2. Triggering and propagation of granular flows

2.1 Granular flows

Sediments are mainly produced by degradation processes of rocks and by precipitation processes of minerals from solutions. In nature, they can be found in a wide variety of environments, from the deep sea to the tops of the highest mountains.

The process of moving sediment from one place to another is called sediment transport. It occurs due to wind, water, ice and gravity. In mountain catchments and in the hydrographic network, we can identify different modes of sediment transport.

In rivers and torrential flows, the sediment transport is driven by hydrodynamic forces. The sediment concentration, defined as the ratio between the sediment volume and the occupied volume, is typically less than 20-25% (Coussot and Meunier 1996; Ancey 2001a; Heiser et al. 2015). Solid particles may travel longer or shorter distances depending on the intensity of the driving forces, on the morphology and topography.

In granular flows, the main forcing is the gravity. The involved mass is a triphasic medium consisting of sediments, water and air. Unlike fluvial transport, sediment concentration is much higher. The particles play a crucial role in the flow dynamics since they strongly interact by exchanging momentum through collisions and friction.

In a third category, we can group all the slope movements identified with

the words "fall", "topple", "slide", "spread" and "creep" (Hungr et al. 2014). Like in granular flows, the main driving force is the gravity. However, interactions among grains play a secondary role in the characterization of dynamic behavior of such types of movements (Tab. 2.1).

This work focuses on granular flows. Using international terminology, we can include in this category pyroclastic flows, debris avalanches, rock avalanches and debris flows. Pyroclastic flows are flows of hot gases, water and hot pyroclastic fragments that occur in a volcanic environment. They are characterized by having a further upper flow of gas where velocities are

Tab. 2.1 - Classification of the slope movements (Hungr et al. 2014)

Movement Type	**Rock**	**Debris**	**Earth**
Fall	1. rock fall	2. debris fall	3. earth fall
Topple	4. rock topple	5. debris topple	6. earth topple
Rotational sliding	7. rock slump	8. debris slump	9. earth slump
Translational sliding	10. block slide	11. debris slide	12. earth slide
Lateral spreading	13. rock spread	-	14. earth spread
Flow	15. rock creep	16. talus flow 17. debris flow 18. debris avalanche 19. soil fluction 20. soil creep	21. dry sand flow 22. wet sand flow 23. quick clay flow 24. earth flow 25. rapid earth flow 26. loess flow
Complex	27. rock slide debris avalanche	28. cambering, valley bulging	29. earth slump earth flow

high enough to fluidize the transported solid material (Takahashi 2014). Debris avalanches represent a flow of granular mixture, partially or totally saturated, which occurs on steep slopes without confinement (Hungr et al. 2014). Rock avalanches are an extremely rapid slope movement where the involved mass is a dry fragmented rock. Debris flows are a flow of granular material, generally saturated, characterized by high mobility and high sediment transport capacity.

Among the aforementioned granular flows, debris flows are the most studied phenomena as they frequently involve anthropized areas causing damage to structures, bridges, roads and, in the worst case, deaths. The development of a debris flow involves three areas. The triggering zone represents the area in which part of the solid material loses stability and starts flowing downstream. The flowing mass, consisting of sediments and water, can erode and entrain large quantities of sediment. In the propagation zone, represented by a slope or a channel incised in it, debris flows reach their maximum speed. A fully developed debris flow can show velocities of tens of meter per second while volume can cover a range from hundreds to 1 million m^3. At the exit of the channelized area, the flow stops thanks to much smaller inclination angles and the possibility of expanding.

The particle size distribution within a debris flow can be strongly heterogeneous. It depends on the types of sediment present in the triggering areas and in the propagation zone. Huge blocks can be transported over long distances thanks to high bulk densities and high velocities (Fig. 2.1). Boulders and larger sediments are typically transported in the front of a debris flow while the smaller sediments are transported in the body and in

Fig. 2.1 - Boulder transported by a debris flow occurred in December 1999 at Caraballeda, Venezuela (source: US Geological Survey)

the tail.

Granular flows are highly unpredictable and high hazardous phenomena and, thus, object of study in the hydrogeological risk assessment. The areas affected by these types of flow are usually located at the base of the slopes and can be very far from the triggering area. The high velocities and the high solid concentrations make debris flows high destructive phenomena.

2.2 Triggering

The presence of sediments predisposed to mobilization depends on many factors. The geologic history of the slope plays an important role. For example, the Campanian Apennines, in the nearest of the Vesuvio volcano, are covered by soil layers formed by deposition of pyroclastic material from the plinian eruptions of the volcano. They are particularly predisposed to

mobilization (the Sarno 1998 event). Sediments can also come from slow and continuous erosion processes on the slope. They can be transported in small channels and mobilized by occasional floods that can turn into debris flows (Ancey, 2001a).

Generally speaking, the slope stability depends on the relative magnitude of the resistance forces and the driving forces. The main contribution to the resistance forces is given by the shear stress offered by the soil (Schofield and Wroth 1968; Lambe and Whitman 1969). In the slope stability analysis, one of the most used scheme is the indefinite slope. It supposes that the failure occurs on a surface parallel to the soil surface over which frictional forces develop. The analysis is based on the evaluation of the *safety factor* defined as the ratio between the resistance forces, offered by the soil, and the driving forces, due to the weight of the unstable soil layer. According to the Terzaghi's principle (Terzaghi 1943), in case of saturated condition, the effective normal stresses in the soil, σ', can be obtained by subtracting the interstitial fluid pressure, p, from the total normal pressure, σ. When pore water pressure is present, the Coulomb theory, which is one of the most used failure theory, states:

$$\tau_{co} = \tau'_0 + \sigma' \tan\varphi' \qquad (1)$$

where τ_{co} is the critical shear stresses offered by the soil, τ'_0 represents the effective cohesion of the soil, σ' is the effective normal pressure and φ is the internal angle of friction of the granular material (Schofield and Wroth 1968; Lambe and Whitman 1969; Savage and Baum 2005).

In mountain environments, rainfall and rapid snowmelt play the major role in the slope stability (Wieczorek and Glade 2005). In saturated soil, the

presence of the water generally induces a decreasing of the safety factor with respect to the case of dry soil. Only in some cases, depending on the seepage direction with respect to the inclination angle of the slope, the safety factor increases (Savage and Baum 2005). In unsaturated soil, the negative pore pressure, namely minor than the atmospheric pressure, produces further resistance forces, due to capillarity and absorption phenomena (Fredlund et al. 1978; Rahardjo et al. 1995). However, when the negative pore pressure is dissipated due to the infiltrated rainfall, the contribution of the capillarity to the slope stability suddenly vanishes (Krahn et al. 1989; Ng and Shi 1998). In Literature, two main debris flow triggering mechanisms were identified: mobilization from landslides and progressive entrainment of sediment due to surface runoff. According to Iverson et al. (1997), a landslide may mobilize to form debris flows when the following mechanisms occur: Coulomb failure in the soil; partial or complete liquefaction of the mass due to high pore pressures; conversion of the translational energy of the landslide into vibrational energy. The portion of the rain that do not infiltrate in the soil can turn in surface runoff. In the gullies and the rills of the triggering area, surface runoff induces shear stresses on the soil surface. It can entrain sediments, increases its volume and turn into a debris flow (Tognacca et al. 2000; Coe et al. 2008; Gregoretti and Fontana 2008). Two main generation mechanisms were identified: the *infiltration excess* mechanism and the *saturation excess* mechanism. The infiltration excess mechanism (Horton 1933) considers a maximum infiltration capacity of the soil that depends on the water content and the physical properties of the soil. If the rainfall intensity is higher than the infiltration capacity, surface runoff is generated.

This generation mechanism mainly occurs in semi-arid rangelands and in cultivated field, where the infiltration capacity of the soil is low, and in regions characterized by high rainfall intensities (Tarboton 2003). If the soil structure is quite open due to both decaying roots and the activity of the micro fauna, the permeability is quite high. The rainfall intensity generally do not exceeds the infiltration capacity of the soil and the infiltration excess mechanism is rare. In these cases, the water table can raise up to the soil surface and the soil fully saturates. Rainfall cannot infiltrate anymore and surface runoff is generated by a saturation excess mechanism (Dunne and Black 1970).

2.3 Propagation

The presence of a solid component in the mixture makes the dynamic behavior of granular flows very different from that of a monophasic fluid, such as water.

Two different approach can be followed for studying the dynamics of granular flows. In a discrete approach, the dynamic of individual elements defines the dynamics of the entire flowing body. One can obtain information both at a microscopic and macroscopic level. However, in the case of excessively high discretizations, computational costs are high. In a continuum approach, the discrete characteristics of motion are necessarily neglected. The equations comes from the fluid dynamics: mass conservation equation; momentum conservation equation; constitutive equation, namely the relation between the stress tensor and the shear rate tensor of the mixture.

To face the problem of dynamics, one need to use a model that represents the granular mixture. In the single-phase model, the mixture is considered as a single medium for which the constitutive equation, namely the rheological law, is unique and implicitly considers the interactions between interstitial fluid and solid particles. The shear rate stress tensor is defined by its components $\dot{\gamma}_{ij}$:

$$\dot{\gamma}_{ij} = \frac{1}{2}\left(\frac{\partial u_i}{\partial x_j} + \frac{\partial u_j}{\partial x_i} \right) \quad , \quad i, j = 1, 2, 3 \qquad (2)$$

where u_i e u_j represents the velocity components of the mixture in the i and j direction, respectively, in a cartesian coordinate system of axes x_1, x_2 and x_3. In the two-phase models, a solid phase and a liquid phase are considered. The equations involve a further relation describing the momentum exchanges between the two phases.

The problem of the dynamics of granular flows is mainly related to the constitutive equation. The rheological law strongly depends on the characteristics of the sediments, their concentration and the properties of the interstitial fluid so various dissipation mechanisms could arise within a granular flow. To date, different flow regime were identified, each of which corresponding to a particular resistance mechanism. In the following, we will focus on the description of single-phase models. The main flow regimes will be illustrated with particular attention to those regimes for which the resistance mechanisms are mainly due to intergranular actions, namely collisions and friction among the grains, object of the present research work.

2.3.1 Frictional regime

When the solid concentrations is very high and the strain rates are very small, the grains remain in continuous contact. The shear stresses that develop in the mixture mainly arise from the friction among the grains so the contribution of the interstitial fluid can be neglected. The study of this regime is usually carried out according to the theories of soil mechanics (Schofield and Wroth 1968; Savage 1984; Savage and Hutter 1989; Gray et al. 1999). A classical approach is to employ the Coulomb theory, already presented in Sect. 2.2, for the estimation of the critical shear stresses τ_{co}. It is worth underlining that Eq. (1) is not a rheological law since it does not involve a dependence of the shear stress from the shear rate. However, it is a capable to describe the main dissipation mechanisms within a granular body when the grains exhibit long-lasting contacts.
This regime is also called *plastic* or *quasi-static*.

2.3.2 Collisional regime

The *collisional* regime, or *inertial*, or *dilute*, is characterized by high deformations and low concentrations of sediments. The momentum exchanges in the granular mixture are mainly due to collisions among the grains. The effects of the interstitial fluid are irrelevant. Bagnold (1954) observed the inertial regime in experiments on a granular mixture with a Newtonian interstitial fluid. The mixture was sheared between two rotating drums at different solid concentration of particles. The volume fraction, *c*,

was expressed by Bagnold in terms of linear concentration λ defined as

$$\lambda = \frac{1}{(c_0/c)^{1/3} - 1} \tag{3}$$

where c_0 is the maximum possible concentration. Bagnold introduced the concept of dispersive pressure, i.e. a radial pressure generated by collisions between particles. He found that, in the case of linear concentrations λ<12 and relative velocity of rotation of the drums sufficiently high, the shear stresses and the dispersive pressures were directly proportional. Furthermore, the stresses were directly proportional to the square of the shear rate $\dot{\gamma}$. In particular, shear stresses could be defined by:

$$\tau = a\rho_s \left(\lambda d\right)^2 \sin\varphi_d \dot{\gamma}^2 \tag{4}$$

where a is an empiric constant, ρ_s is the grain density, λ is the linear concentration, d is the grain diameter and φ_d is the dynamic angle of friction. In the Bagnold's work, a dimensionless quantity was introduced, the Bagnold number, *Ba*, defined as the ratio between the inertial stresses and the viscous stresses:

$$Ba = \frac{\lambda^{1/2}\rho_s d^2 \dot{\gamma}}{\eta} \tag{5}$$

where η is the viscosity of the interstitial fluid. The collisional regime was identified for $Ba > 450$.

Despite the work of Bagnold was an avant-garde study, some authors pointed out that some aspects need to be revised. Hunt et al. (2002) explained that the height of the cylinders was small compared with the distance between the cylinders. This could have induced vortices in the granular mixture and, thus, an erroneous estimation of the tangential stresses.

Moreover, they showed that only the dispersive pressures exhibit a quadratic dependence on the shear rate while the shear stress depends on the shear rate raised to the 1.5 power. Armanini et al. (2008) showed that if one applies Eq. (4) to solid-liquid mixtures, volume fraction must be constant along flow depth, which is in contrast with the experimental evidences (Armanini et al. 2005). Over the years, new theories have been introduced and developed, for example the *kinetic theories* (Jenkins e Savage 1983; Lun et al. 1984). These theories are based on the analogy between the pressure generated by the agitation of the gas molecules and the pressure due to collision among the grains. The kinetic theories have introduced the concept of granular temperature, *T*. Similar to the thermodynamic temperature, *T* is proportional to the kinetic energy of the granular medium per unit of mass. It depends on the instantaneous fluctuation velocities of the grains $u' = u - \langle u \rangle$, where *u* is the instantaneous velocity and $\langle u \rangle$ is the ensemble-average of the velocity *u*. The granular temperature is defined as:

$$T = \frac{1}{3} \sum_{i=1}^{3} \langle (u_i')^2 \rangle \qquad (6)$$

where u_i' is the component of the instantaneous fluctuation velocity in the *i*-direction and the symbol $\langle \ \rangle$ denotes the ensamble average.

2.3.3 Viscous regime

If the concentration of fine sediments is high and the presence of the interstitial fluid cannot be neglected, the granular flow show a Newtonian

behavior:

$$\tau = \eta_m \dot{\gamma} \tag{7}$$

where η_m is the mixture viscosity and depends on the volume fraction and on the characteristics of the granular material. The *macroviscous* regime was idenfied by Bagnold (1954) in the same experiments described in Sect. 2.3.2. For this regime, he found that the Bagnold Number should be lower than 40.

2.3.4 Transitional regime

The regimes presented in the previous sections represent limit situations in which the momentum is exchanged with a single prevailing mechanism. However, in nature, motion regimes can be characterized by the coexistence of several different resistance mechanisms.

In flows characterized by high sediment concentrations, such as hyper-concentrated flows of water and clay, the friction between grains could generate a threshold shear stress, τ_y, exceeded which movement occurs. The Bingham *viscoplastic* regime describes this rheological behavior through the following relations:

$$\begin{aligned} &\tau \le \tau_y \qquad && \dot{\gamma} = 0 \\ &\tau > \tau_y \qquad && \tau = \tau_y + \eta_b \dot{\gamma} \end{aligned} \tag{8}$$

where τ_y and η_b are the threshold shear stress and the viscosity of the mixture, respectively, and depend on the mixture properties. Bingham rheology was generalized by Herschel-Bulkley, who introduced a further rheological parameter, n, as an exponent of the shear rate:

$$\begin{aligned} \tau \le \tau_y \qquad & \dot{\gamma} = 0 \\ \tau > \tau_y \qquad & \tau = \tau_y + \eta_{hb}\dot{\gamma}^n \end{aligned} \tag{9}$$

Other models have been developed to take into account turbulence and collisions between grains. This is the case of the O'Brien and Julien model (1984) that adds two further terms to the Bingham model.

Several authors proposed rheological models in which different kind of particle-particle interactions govern the dynamics. In the *frictional-collisional* regimes, the classical approach is to define the shear stress, τ, as a sum of a collisional component, τ_c, shear rate dependent, and of a frictional component, τ_f, shear rate independent. Johnson et al. (1990) proposed a model in which the frictional stress is given by a Coulomb relationship and takes place only when the volume fraction is greater than a certain value. Instead, the collisional component is based on the kinetic theory of Lun et al. (1984). Ancey et al. (1999) introduced the Coulomb Number, *Co*, in order to identify various types of regimes in a mixture of granular material and Newtonian fluid. It was defined as the ratio between the collisional stresses and the effective stresses, $\sum$, in the mixture assumed equal to the frictional stresses:

$$Co = \frac{\rho_s r^2 \dot{\gamma}^2}{\Sigma} \tag{10}$$

where *r* is the grain radius. If *Co*<<1 a frictional regime takes place whereas, for *Co*>>1 the collisional regime is predominant. The frictional-collisional regime occurs when $Co = O(1)$. Ancey and Evesque (2000) proposed a frictional-collisional model for granular mixtures for which the shear stresses were the sum of a coulomb frictional stress component and a

collisional component proportional to $\dot{\gamma}^2$ and function of *Co*. Another dimensionless quantity used to distinguish the prevalent resistance mechanism in a mixture is the Savage Number, *Sa*, introduced by Savage (1984). It is defined as the ratio between the collisional and the gravitational stresses:

$$Sa = \frac{\rho_s d^2 \dot{\gamma}^2}{P_b} \tag{11}$$

where P_b represents a characteristic normal pressure value in the sheared region. For Savage Number $Sa>0.1$, collisions become prevalent whereas, if *Sa* is very small, the frictional regime takes place (Savage and Hutter, 1989). Among the most commonly used rheologies to describe intermediate regimes, also called *dense regimes*, the $\mu(I)$ rheology is one of the most corroborated in case of dry granular flows. It was developed by GDR MiDi (2004) and it is based on the use of a dimensionless quantity called Inertial Number, *I*. The Inertial Number, equal to the square root of the Coulomb Number, expresses the relative importance of the shear deformation with respect to the confinement effect of the normal pressures and is defined by the following relation:

$$I = \frac{\dot{\gamma} d}{\sqrt{P/\rho_s}} \tag{12}$$

where *P* are the normal pressures. When *I* tends to 0, the deformations are almost null and the regime is quasi-static. When *I* assumes high values, the dilute regime takes place. For intermediate value of *I* (from 0.01 to 0.5, Jop 2015), both friction and collisions occur. The shear stress is directly proportional to the normal stresses through an effective friction coefficient,

$\mu(I)$:

$$\tau = \mu(I)P \ , \qquad \mu(I) = \mu_s + \frac{\mu_2 - \mu_s}{I_0/I + 1} \tag{13}$$

where μ_s, μ_2 and I_0 are parameters depending on the granular material. In particular, μ_s is the value assumed by $\mu(I)$ when I tends to 0, namely in the quasi-static regime. μ_s can be expressed as tan φ, where φ is the internal friction angle of the granular material. The parameter μ_2 represents the values that $\mu(I)$ assumes when I tends to infinity, namely in the purely collisional regime. It can be expressed as tan φ_{sat}, where φ_{sat} is a value of a dynamic angle of friction for which $\mu(I)$ saturates. The third parameter, I_0, is the value of the Inertial Number for which $\mu(I) = \frac{\mu_s + \mu_2}{2}$. Eq. (13) can be viewed as a constitutive relation where the shear stress is the sum of a frictional stress and a stress in which the effective viscosity depends both on $\dot{\gamma}$ and on the normal pressure P (Jop et al. 2006). $\mu(I)$ rheology is capable to well describe the average characteristics of the motion field in case of dense flows (GDR MiDi 2004). However, fast dense avalanches or high-shear mixing processes cannot be modeled accurately by this rheology (Jop 2015).

Mills et al. (1999) proposed another approach for the constitutive problem. He elaborates a non-local theory where instantaneous force chains and arcs take place in the granular medium carrying most of the stresses while the rest of the grains behave like a fluid. The Mills' rheology introduces an additional stress component due to the interactions of the chains with the surrounding grains as a function of the spatial distribution and of the length of the force chains.

2.4 Field observation

Field observations are fundamental to improve the knowledge of the triggering mechanisms and of the dynamics of granular flows. Field data can be used for the design of Early Warning Systems and for model's calibrations. The study of granular flow at field scale arises from my personal need to observe and study the environment in which they occur and propagate. It was conducted during the short research period abroad at the Universitat Politècnica de Catalunya (Barcelona).

The debris flow monitoring stations at catchment scale are equipped with a series of devices. The use of a rain gauge is essential for rainfall recording, as precipitation is one of the main triggering factors for debris flows. A common approach in dealing with rainfall data is to use mean intensity-duration curves (Caine 1980; Guzzetti et al. 2007; Brunetti et al. 2010). Power law models can define thresholds in terms of different levels of probability of occurrence of triggering rain episodes. In some areas and in some period of the year, snow melting can be the major triggering cause. Once melted, the snow infiltrates in the ground increasing its water content and causing instability in the slope. In this case, sensors for measuring snow depth can be useful for quantifying this contribution. As previously illustrated (Sect. 2.2), the study of soil conditions is important to understand which are the triggering mechanisms for debris flow and, thus, adopt the most suitable mitigation measures. To that scope, the most commonly used devices are pore water pressure, water content and suction sensors. Although

the knowledge of soil conditions is fundamental, few studies have dealt with this measurement (Coe et al. 2008). This is mainly due to the multitude of pathways that water can travel in natural soil making the identification of the prevalent infiltration mechanism difficult (Tarboton 2003). Among the classical devices used in the triggering areas for debris flow monitoring, one have to mention other devices used for landslide monitoring, since landslides can mobilize to form debris flows (Sect. 2.2). Therefore, inclinometers and extensometers can be employed as well as GPS systems for the measurement of ground deformations (LaHusen 2005).

Recently, the study of the propagation phase of debris flows is performed through seismic sensors, such as geophones, accelerometers and seismometers. These sensors are able to measure ground vibrations generating by a flowing mass (Arattano 2000). The geophones represent the most used sensors in debris flow monitoring (Berti et al. 2000; Marchi et al. 2002; Badoux et al. 2009; Hürlimann et al. 2014) thanks to the low power consumption and their robustness. They are mainly used as triggering sensors for other monitoring systems or for identification in alarm systems (Abancó et al. 2012; Abancó et al. 2014). The location of the geophones is a critical factor. The measurements are strongly influenced by the distance between the geophones and the source of vibrations, the characteristics of the soil and the geophone assembly. Geophones can be used to identify and distinguish different types of flow. By using measurements of several geophones located in different position, it is possible to estimate the flow velocity.

In the field, it is also possible to measure flow depth. The techniques involve

the use of radar sensors and laser devices located above the propagation channel. The employment of cameras allows a direct observation of the phenomenon and helps in identifying the type of flow.
Load cells and piezoelectric sensors are used to measure the forces acting on the basal surface so as one can estimate the Coulomb friction coefficient at the bed (McArdell et al. 2007). Moreover, it is possible to deduce the bulk density if flow depths are known.

2.5 Laboratory investigation

Laboratory activity is an important tool as it allows the study of phenomena under controlled conditions and the calibration and validation of theories and models. My doctorate mainly focused on the study of the dynamics of granular flows at a laboratory scale. Main goal is to improve the knowledge of the particle-particle resistance mechanisms and the influence of the boundaries on the dynamics.
The rheological behavior of granular flows can be investigated using several configurations. The most common is the annular shear cell, or Couette cell (Mueth et al. 2000; GDR MiDi 2004). It consists of two concentric cylinders between which the granular mixture is sheared. The outer cylinder remains stationary while a rotational speed is imposed to the inner cylinder by applying a given force. A constitutive relationship can be then obtained by relating the force applied to the inner cylinder with the deformation in the mixture. In the vertical chute configuration (Pouliquen and Gutfraind 1996; Chevoir et al. 2001) the granular material is let flowing down into a vertical

cylinder under the effect of gravity. An opening gate located at the bottom of the cylinder controls the flow rate. It is possible to obtain uniform flow conditions and measure the velocity field and the volume fraction. Another device is the rotating drum. It is filled with grains and rotated so that uniform flow takes place. It is possible to measure different quantities such as the thickness of the flowing layer, its inclination angle, velocity and volume fraction (Nakagawa et al 1993; Bonamy et al., 2002). A configuration similar to the rotating drum is used in the Hele-Shaw cell. It consists of two glass plates separated by a certain distance. The granular material is poured from a hopper above a granular deposit within the two plates (Komatsu et al. 2001). Several laboratory studies are performed in channels where the granular material is let flow down under gravity on a stabilized static pile (Pouliquen 1999; Taberlet et al. 2003). The inclined channel configuration allows investigating the dynamics and influence of the boundaries. This device consists of a channel in which the granular material is let flow down under gravity.

The variables that mostly influence the rheological behavior of granular flows are velocity and volume fraction. The necessity to study undisturbed flows has led to the development of non-invasive measurement techniques. They can be divided into two macro categories: techniques that allow to investigate within the flow domain and techniques that allow to measure only at the boundary. X-ray tomography, magnetic resonance imaging and γ-radiation belong to the first category. The main disadvantages of these techniques are the high installation and maintenance costs. Furthermore, X-ray tomography does not allow high frequency image acquisition (Grudzień

et al. 2011), while magnetic resonance is very sensitive to velocity fluctuations (Nakagawa et al. 1993). The optical techniques provide informations only at the boundaries. Despite the obvious disadvantage, they are very cost-effective techniques and have been used in numerous studies reaching high levels of precision and accuracy.

In the present research work, the experiments were carried out on an inclined channel using granular material and air as interstitial fluid so as to maximize the resistances due to intergranular forces. Velocity and volume fraction measurements were taken using optical devices.

In the following sections, the optical techniques, currently used in the study of dry granular flows, and the main issues in the study of chute granular flows will be presented.

2.5.1 Optical technique for velocity measurements

The most common optical techniques employed for measuring velocity are the Particle Tracking Velocimetry (PTV) and the Particle Image Velocimetry (PIV).

The PTV technique (Jesuthasan et al. 2006) employs a Lagrangian approach. The digital images are used to trace the trajectories of each individual grain and, thus, to measure the displacement. The heart of a PTV algorithm lies in the procedure for identifying the grains. Over the years, different algorithms have been proposed, based on different approaches (Kobayashi et al 1989; Uemura et al 1989; Capart et al. 2002).

The PIV technique (Willert and Gharib, 1991) follows an Eulerian approach.

The images are divided into small sub-images. The brightness patterns are analyzed. The maximum value of the cross-correlation function between two consecutive frames corresponds to the most likely displacement. In case of application to very fast or strongly sheared flows, the PIV technique can produce measures affected by high errors. However, this limitation has been overcome thanks to the introduction of new algorithms which used window deformation technique (Thielicke and Stamhuis, 2014).
Both techniques have been successfully applied to dry granular flows.

2.5.2 Optical techniques for volume fraction measurements

Recently, some optical techniques have been proposed to measure volume fractions. Ahn et al. (1991) used fiber-optic probes in a channel configuration for volume fraction measurement. By measuring the typical distance between the grains, they estimated the solid concentration by a conversion formula. Bonamy et al. (2002) employed a linear transfer function to estimate volume fraction based on the sum of grains visible from a transparent sidewall. Capart et al. (2002) proposed a method based on the partition of images recorded by a video camera via Voronoi tessellation. Each Voronoi cell contains a grain and part of the area around it. Based on Monte Carlo simulations, they indicated three possible indices, depending on the shape, the size and the density of the cells in the image, through which one can estimate volume fraction. Spinewine et al. (2003), who used a stereoscopic setup, extended this approach. Barbolini et al. (2005) proposed the use of a brightness threshold to be applied to grayscale sidewall images..

Spinewine et al. (2011) proposed a methodology based on the use of a laser beam that allowed the measurement of the average distance of the grains from the sidewall of the chute. These measurements can be related with volume fraction. Recently, Sarno et al. (2016) proposed an optical-stochastic method that allows the estimation of the near-wall volume fraction from a two-dimensional quantity, called two-dimensional volume fraction, measurable in sidewall images. Simulations with Monte Carlo provided an exponential stochastic relationship between the two-dimensional volume fraction and the near-wall volume fraction.

2.5.3 Main issues in the study of granular flows

The stress distribution in a granular flow is not well known and this makes the study of the rheology of granular flows even more complicated.
In a newtonian fluid such as water, the stress tensor can be decomposed into a spherical tensor and a deviatoric tensor. In the spherical tensor, the only non-zero elements are in the main diagonal and represent the normal isotropic stresses. In the symmetrical deviatoric tensor, the elements on the main diagonal are zero while the other elements represent the shear stresses. From the soil mechanics, normal pressures in a granular medium are not isotropic (Taylor 1948; Schofield and Wroth 1968). The vertical normal stresses are assumed to be hydrostatic. Normal horizontal stresses are considered scaled quantities of vertical stresses. The scaling factor is a constant and depends on the direction along which the normal horizontal stress is evaluated. It is called earth pressure coefficient K_i, where i is a

generic direction. According to Hungr et al. (1995), in a granular flow, K can vary in the range [K_{act}, K_{pass}], where K_{act} is the active earth pressure coefficient and K_{pass} is the passive earth pressure coefficient of the Rankine theory. Savage and Hutter (1989) developed a model for a dry granular medium sliding on a smooth basal surface. They considered active or passive conditions depending on whether the flow is elongating or compressing. Considering that the failure occurs simultaneously at the basal surface and in the flowing body, the coefficient K in the longitudinal direction, x, can be obtained from the Mohr circles:

$$\begin{aligned} &\frac{\partial u}{\partial x} > 0 \qquad K_{act}^{x} = 2/\cos^2\varphi\left[1-\sqrt{1-\cos^2\varphi/\cos^2\varphi_{gb}}\right]-1 \\ &\frac{\partial u}{\partial x} < 0 \qquad K_{pass}^{x} = 2/\cos^2\varphi\left[1+\sqrt{1-\cos^2\varphi/\cos^2\varphi_{gb}}\right]-1 \end{aligned} \tag{14}$$

where u is the longitudinal velocity, φ is the internal angle of friction of the granular material and φ_{gp} is the angle of friction between grains and the basal surface. Eqs. (14) are valid as long as $\varphi_{gb} < \varphi$. Other authors (Hutter et al. 1993; Gray et al. 1999) proposed relations for the earth pressure coefficient in the transversal direction y:

$$\begin{aligned} &\frac{\partial v}{\partial y} > 0 \qquad K_{act}^{y} = 1/2\left[K_{act}^{x}+1-\sqrt{\left(K_{act}^{x}-1\right)^2+4\tan^2\varphi_{gb}}\right] \\ &\frac{\partial v}{\partial y} < 0 \qquad K_{pass}^{y} = 1/2\left[K_{pass}^{x}+1+\sqrt{\left(K_{pass}^{x}-1\right)^2+4\tan^2\varphi_{gb}}\right] \end{aligned} \tag{15}$$

where v is the transversal velocity. Under the hypothesis of coulumbian relation between normal and shear stresses, different values of K in the x and y direction, does not observe the symmetry in the deviatoric tensor. Iverson e Denlinger (2001) proposed an approach similar to the one of Savage and

Hutter (1989) but using the same coefficient along x and y direction employing the same equations (14). However, they introduced different conditions to identify a locally divergent ($\partial u/\partial x + \partial v/\partial y > 0$) or locally convergent ($\partial u/\partial x + \partial v/\partial y < 0$) flow. As pointed out by Iverson e Denlinger (2001), Eq. (14) represents a more general expression of the earth pressure coefficients of the Rankine theory because they take into account both failure along the bed and within the granular material. Indeed, in case of $\varphi_{gb} = 0$, Eq. (14) reduce to the Rankine active coefficients. If $\varphi_{gb} \geq \varphi$, frictional forces occurs at the bed and K can assume a unique value

$$K^{x}_{\varphi_{gb}=\varphi} = \frac{1+\sin^2\varphi}{1-\sin^2\varphi} \qquad (16)$$

This means that the granular material flows downslope with zero velocity divergence. Despite the various solutions proposed in Literature, the stress distribution in a granular flow still remains an open problem.

The inclined channel configuration allows a better comprehension of the dynamics of the chute granular flows and of the dissipative mechanisms that arise at the boundaries, which influences the flow regime. In literature, a model capable to describe the interaction between a granular flow and the sidewalls is still missing. This is a crucial factor for the validation of rheological models. This issues, already known in the past (Savage 1979, Johnson et al., 1990), has been addressed only in the last decades. Taberlet et al. (2003) studied the flow of dry granular material in narrow channels. A fully developed and uniform flow developed above a stabilized static pile. They noted that the slope of the flowing layer was much larger than the internal friction angle of the granular material. This means that the active

forces had to overcome a further resistance, namely the sidewall friction. Taberlet et al. (2003) elaborated a simple depth-averaged model based on the momentum balance of the flowing layer. They assumed constant volume fraction along the depth, isotropic stresses, hydrostatic distribution of the stresses, and Coulomb friction at the sidewalls and at the interface flowing layer - stabilized pile. Since we are in the case of uniform flow, the momentum conservation reduced to the following force balance:

$$\tan\beta = \mu_g + \mu_w \frac{h_{flow}}{W} \qquad (17)$$

where β is the inclination angle of the free surface, $\mu_g = \tan\varphi$ with φ angle of friction of the granular material, μ_w is the angle of friction between grains and sidewall, h_{flow} is the thickness of the flowing layer, W is the channel width.

Jop et al. (2005) performed a series of experiments in the same configuration of Taberlet et al. (2003) but investigating channel widths up to 570 times the average diameter of the grains. They found that the sidewall effect is never negligible, even in case of very large channels. This can be observed in the velocity measurements at the free surface, which exhibit a minimum, in correspondence of the walls due to friction, and a maximum in the center of the channel. Based on the simplified hypotheses of Taberlet et al. (2003), Jop et al. (2005) proposed a model for a uniform granular flow that flows on a heap that takes into account the friction of the walls. The force balance applied to an elementary slice can be written as:

$$\tan\beta = \mu(\mathrm{I}(z)) + \mu_w \frac{\delta}{W} \qquad (18)$$

where δ is the distance from the free surface of the downward surface of the elementary slice. The first term on the right-hand of the equation represents the resistance of the grains during their motion and depends on the rheology. In their model, they employed the $\mu(I)$ rheology (Eq. (13)). As one can note, in the Eq. (18), the effect of the walls on the entire flow domain, namely velocity variations along the transversal direction, are not taken into account. An attempt to quantify this effect on velocity profiles was proposed by Sheng et al. (2011). By considering a cartesian reference system (0, x, y, z) where the origin is located at the basal surface, x is the longitudinal direction, y is the transversal direction and z is the direction perpendicular to the basal surface, the integration of the velocity u along the width W can be approximately written as:

$$\frac{1}{W}\int_0^W u(x,y,z)dy \approx f(x,z)u(x,z) \qquad (19)$$

where $f(x,y)$ is a scaling factor which takes into account the sidewall effect on the velocity in the y direction and can be obtained from (19)

$$f(x,z) = \frac{\frac{1}{W}\int_0^W u(x,y,z)dy}{u(x,z)} \qquad (20)$$

By using optical techniques, it is not possible to obtain information on the trend of the coefficient $f(x,z)$ along the flow depth. However, in some cases, this coefficient can be considered constant, since the shape of the velocity profiles at the free surface and the basal surface is very similar (Ahn et al 1991, Sheng et al., 2011). Therefore, Eq. (20) can be successfully used to scale the measured profiles at the sidewalls and obtain a representative average profile of the entire cross section.

Another important issue in the study of dry granular flow is related to the rheological stratification. Recent works pointed out that different flow regimes may coexist (Komatsu et al. 2001; Armanini et al. 2005; Doyle et al. 2010) and their occurrence depends also on the effect of the boundaries (Taberlet et al. 2003; Sarno et al. 2014; Sarno et al. 2018a). In order to properly infer on the dynamics of dry granular flows, the evaluation of the effect of the boundaries on the dynamics should be well understood.

3. Methods and experimental setup of the investigation at laboratory scale

The laboratory activity permits investigating on a phenomenon under controlled conditions. One can focus on the effect of few factors while the others are kept constant.

The aim of the laboratory investigation performed during my PhD was to investigate on the effect of the boundaries on the dynamics of steady chute dry granular flows. A unique granular medium was employed in all the experiments. Plexiglas open channels were used. The transparent sidewalls allowed employing optical techniques and study flows not disturbed by the measurement devices. The dynamics was investigated by analyzing velocity measurements, taken both at the sidewall and at the free surface, and volume fraction measurements taken at the sidewall.

The experiments can be divided in two groups: experiments over fixed bed (Pouliquen 1999; Ancey 2001b; GDR MiDi 2004) and experiments over erodible bed (Komatsu et al. 2001; Taberlet et al. 2003; Jop et al. 2005). The first group of experiments was performed within the same channel. Two inclination angles of the chute were investigated. Furthermore, different basal surfaces were used in order to study the effects of different kinematic boundary conditions (KBC) at the bed. The second group of experiments was performed in a configuration that often occurs in nature, where the granular material flows over a loose bed made up by the same granular medium. The effect of the channel width on the granular flow dynamics was

investigated by employing two channels with different widths.
In Sect. 3.1, the experimental apparatus will be carefully described. In Sect. 3.2 and 3.3, the velocity and the volume fraction measurement techniques will be presented, respectively.

3.1 Description of the experimental apparatus

The employed granular material was the same in all the experiments. It consists of acetal-polymeric (POM) beads with mean diameter d=3.3mm (Sarno et al. 2011). The internal angle of friction of the granular material, φ, was estimated using a direct shear cell on a sample of size 10cm x 10cm x 4cm. It was found to be ≈27°. Other relevant properties are shown in Tab. 3.1.
The experiments were performed in 2m-long open chutes with a rectangular cross section (Fig. 3.1). Two channels with a width W = 8cm and W = 3cm were employed. The upper part of the channels is used as a reservoir and it is equipped with an external hopper, with a total capacity of ≈40l in all the

Tab. 3.1 – Properties of the employed granular material.

Material	Polyoxymethylene (POM)
Mean diamater, d	3.3 mm
Density, ρ_s	1410 Kg/m^3
Young's modulus	2700 MPa
Internal angle of friction, φ	≈27°
Coefficient of restitution, e	0.83
Volume fraction at deposit, c_{dep}	0.58÷0.63
Colour	matte white

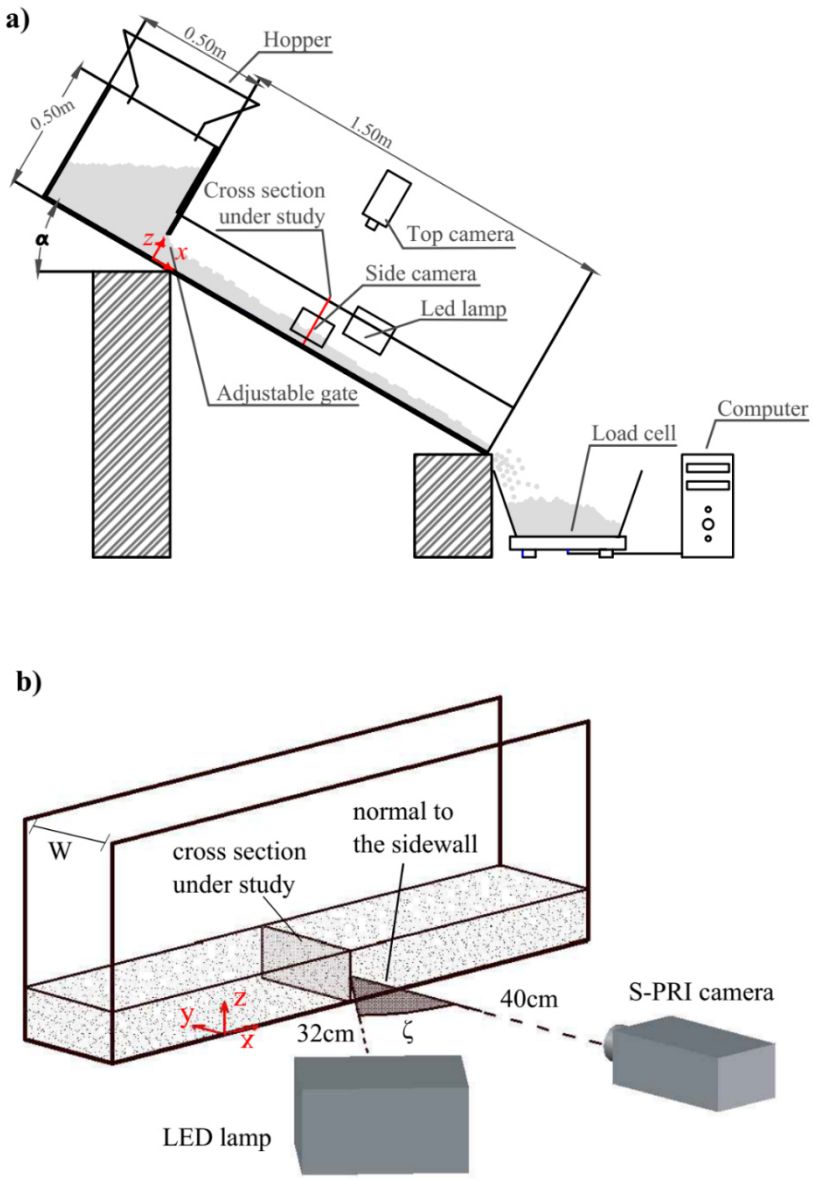

Fig. 3.1 – Sketch of the experimental apparatus: a) side view; b) detail of both the LED lamp and of the side camera (AOS S-PRI) positions with respect to the flume.

experiments. The granular medium was first loaded into the reservoir and,

then, let flow down under gravity through an adjustable gate (maximum allowed gate opening equal to 34cm). Differently from the water, the mass flow rate of granular materials through an orifice weakly depends on the hydraulic head in the reservoir, if the head is sufficiently high compared to the size of the orifice (Nedderman et al. 1982). Therefore, a wide range of steady mass flow rate can be investigated by varying the gate openings. The channels allow the insertion of different basal surfaces so one can explore different kinematic boundary conditions (KBC) at the bed. Furthermore, the channel support permits to tilt the chutes in a wide range of inclination angle, α. An electronic scale (mod. Laumas AZL-50Kg), with an accuracy of 8g, was placed at outlet of the flume to measure the mass flow rate, Q_m.

In the experiments performed over the fixed basal surfaces, the section under study was chosen 40cm downstream the gate. All the runs were performed in a channel of width W = 8cm (≈24d). Two inclination angles of the channel were investigated: α = 30° and α = 35°. We employed five fixed basal surfaces:

- a smooth Bakelite surface (S), with characteristic length of roughness l<<10μm;
- three different sandpaper linings, with l equal to 162 μm (P100 FEPA/ISO 6344), 269 μm (P60) and 425 μm (P40);
- a granular basal surface (G), made up by randomly gluing with silicone the POM beads on the bed, with $l = d/2$ = 1.65 mm.

The angles of friction between the POM granular material and the fixed rough surfaces was estimated using the approach proposed by Savage and Hutter (1991), which is valid for angles of friction less than the internal angle

of friction of the granular material: a small cylinder full of particles was let flow down over the fixed rough surface tilted with a certain inclination angle. The angle of friction between grains and the rough surface is the smallest angle at which steady motion of the cylinder is observed. We found angles of friction of 14.5° and 19.5° for the S-surface and for the Plexiglas walls, respectively, with a standard deviation of the measurements of ≈1° (Sarno et al. 2018a). The angles of friction between grains and the three employed sandpaper linings and grains and the G-surface was found to be more than the internal angle of friction of the POM beads, φ, so they cannot be measured with this method. To my knowledge, in Literature, other techniques developed for measuring the angles of friction between a granular medium and a rough surface are not still present.

The erodible bed configuration was obtained by employing a small weir placed at the end of the channel. The inclination angle of the channel was set in order to allow the formation of a lower wedge of granular material over which the granular material flows. Two channels of width W = 8cm (≈24d) and W = 3cm (≈9d), respectively, were used. The section under study was chosen 100cm downstream from the gate.

Two high speed cameras were used to capture the flow dynamics by recording videos both at the sidewall and at the free surface. The first camera (AOS Technologies, model S-PRI) was placed aside the channel at a distance of 40cm from the sidewall (Fig. 3.1b). This camera allows to record videos with the maximum resolution of 1280 x 1024 pixels and a frame rate of 500 fps (frame per second). By using a lower resolution, one can record videos with a higher frame rate. The second camera (AOS Technologies,

model Q-PRI) was located above the investigated cross section to record the flow at the free surface. Videos can be captured with the maximum resolution of 1696 x 1710 pixels and a frame rate of 500 fps. A high-intensity flickering-free led lamp (model multiLED-LT by Photo-Sonics, luminous output of 8000 lumen) was placed aside the channel at a distance of 32cm and inclined with a certain angle, ζ, between the normal to the sidewall and the normal to the plane of the lamp (Fig. 3.1b). As shown in Sect. 3.3, the inclination of the LED lamp is crucial for the volume fraction measurements.

3.2 Velocity measurements

Particle Image Velocimetry (PIV) was employed for measuring velocity both at the sidewall and at the free surface. This technique was developed for fluid dynamics applications but, recently, it has been extended to granular materials (Lueptow et al. 2000; Eckart et al. 2003; Pudasaini et al. 2005). Differently from the standard PIV application, seeding of particles is not required in granular applications thanks to the optical patterns of the grain surface. Moreover, flashlights (Pudasaini et al. 2005) or flickering-free LED lamps (Sheng et al. 2011; Sarno et al. 2018b) are usually employed in the study of granular flows instead of laser sheets.

PIV algorithms work by calculating the cross-correlation function of two consecutive digital images delayed by a small time interval Δt. Every image is divided in sub-images, called interrogation windows. The discrete cross correlation function $D(m,n)$ is calculated for each interrogation window:

$$D(m,n) = \sum_i \sum_j A(i,j)B(i-m, j-n) \qquad (21)$$

where A and B represent the brightness matrices of two consecutive frames centered in the pixel of coordinates (i,j) and (m,n) is the guessed displacement. The maximum of $D(m,n)$ is the most likely displacement of the interrogation window.

The open source code PIVlab (Thielicke and Stamhuis 2014) is here employed to solve the maximization of the cross correlation function. Two different approaches can be followed. The matrix can be computed in the spatial domain by the direct cross correlation (DCC) or in the frequency domain by the discrete Fourier transform (DFT). In this work, a DFT approach was used to solve (21). Keane and Adrian (1991) suggested that the size of the interrogation window needs to be more than four times the maximum displacement between two consecutive frames in order to limit the *loss-of-pairs* effect. In case of fast flows, the size of the interrogation window could be excessively large causing a very low spatial resolution of the PIV measurements. In order to both respect this limitation and obtain a dense spatial resolution, the DFT approach can be used with a multistep procedure. Several passes of the DFT can be run. The information of the first pass is used to offset the interrogation window in the following passes. The size of the interrogation window can be gradually decreased so a high spatial resolution of the final vector map can be obtained. We employed a 4-step algorithm with size of the interrogation window of 4d-2d-1d-0.5d (spatial scale 1d≈16pixels) for the side view and a 3-step algorithm with size of the interrogation window of 2d-1d-0.5d (spatial scale of 1d≈32pixels) for the top view. The analysis was performed by using 50% overlapping

interrogation windows. The spatial resolution of the velocity measurements was of $d/4$ both at the sidewalls and at the free surface. The spatial resolution of the PIV analysis was intentionally chosen finer than d to reduce errors at the oscillating free surface. Moreover, sub-pixel accuracy can be achieved through a three-point Gaussian interpolation along two normal directions. Thielicke and Stamhuis (2014) reported that, under ideal conditions, PIVlab exhibits a typical random error of ≈0.02 pixel/frame. Considering the length scale and the sampling rate of digital images (1000 Hz), the PIV accuracy is 0.004m/s and 0.002m/s for the sidewall and free surface PIV measurements, respectively.

3.3 Volume fraction measurements

The stochastic-optical method (SOM), proposed by Sarno et al. (2016) and developed at the Laboratorio di IDraulica Ambientale e Marittima, (LIDAM), University of Salerno, is here employed to get near-wall volume fraction measurements in steady chute granular flows.

The SOM method can be employed under high controlled illumination conditions. It allows the evaluation of the near-wall volume fraction, c_{3D}, through an optically measurable quantity, called two-dimensional volume fraction c_{2D}. Monte Carlo generations provided a stochastic exponential relation between c_{2D} and c_{3D} under the hypothesis of random distribution of the grains.

The Monte Carlo investigations involved spherical particles of diameter d, randomly loaded into a virtual cubic box with side length $10d$ without any

particle overlapping (Fig. 3.2a). A light source with parallel rays illuminates the transparent front face, F, with an angle of incidence, ζ. A virtual camera was placed perpendicular to the transparent front face (Fig. 3.2b). The camera is assumed to be infinitely far from F so that the viewing direction is everywhere perpendicular to the front face. In order to reduce the effect of the boundaries of the cubic box that produces a reduction of the volume fraction, an inner cube with side length $6d$ (violet volume in Fig. 3.2a) was considered for the calculations. The two-dimensional volume fraction c_{2D} is defined as the ratio between the projection onto F of all the visible and illuminated portions of particles and the size of the interrogation area (Fig. 3.3). The stochastic exponential relation between c_{3D} and c_{2D} was found

$$c_{3D} = a(\zeta)\exp(b(\zeta)c_{2D}) \qquad (22)$$

where a and b are coefficient depending on ζ. It is worth mentioning that a depends on $1/\cos\zeta$ while b depends only weakly on ζ and probably on the shape of the grains.

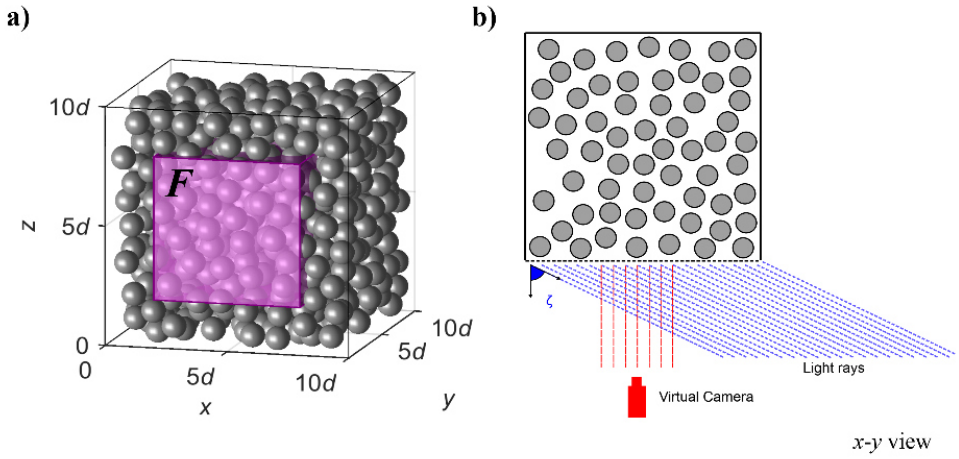

Fig. 3.2 - a) Example of Monte Carlo generation (elaborated from Sarno et al., 2016). b) Geometric set-up employed in the simulations (elaborated from Sarno et al., 2016).

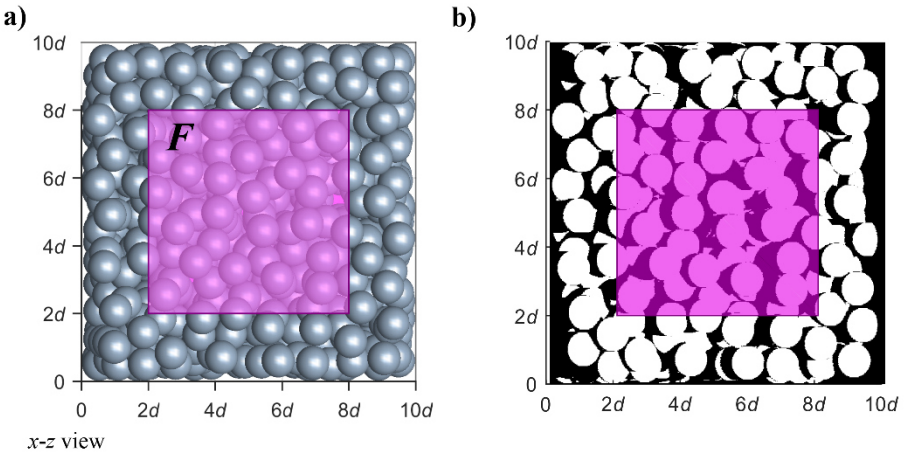

Fig. 3.3 - Example of calculation of c_{2D} in the violet interrogation area: a) Monte Carlo generation of 625 spheres; b) projection onto the interrogation area of all the visible and illuminated portions of particles (elaborated from Sarno et al., 2016).

The best correlation between c_{2D} and c_{3D} was found for angles of incidence of the light rays ζ belonging to the range [10°, 45°]. For $\zeta < 10°$, saturation of c_{2D} at high volume fractions was observed whereas, for $\zeta > 60°$, an increasing data scatter was found.

A local binarization algorithm was employed to measure c_{2D} from gray scale images

$$O_{binary} = \frac{O'_{i,j} - O'_{\min,N(i,j)}}{O''_{\max,N(i,j)} - O'_{\min,N(i,j)}} > s \qquad (23)$$

where $O'_{i,j}$ is brightness value of the generic pixel of coordinates (i,j), $O'_{\min,N(i,j)}$ is the minimum brightness value in a circular neighborhood of the pixel $N(i,j)$ of diameter $2d$, $O''_{\max,N(i,j)}$ is the maximum brightness value in $N(i,j)$ calculated on a smoothed image by applying a mean filter. This operation was necessary because occasional glares on the grain surfaces

induce local maximum brightness peaks and, thus, an underestimation of the c_{2D}. In (23), s is a threshold value which depends on the optical properties of the system (optical properties of the granular material surface and of the sidewalls, type of interstitial fluid, etc.) and it is the only parameter that needs to be calibrated. Once the binarized image, O_{binary}, is available, the two-dimensional volume fraction can be calculated as

$$c_{2D} = \frac{\sum_{N} O_{binary}}{N} \tag{24}$$

where N is the total number of pixels of O_{binary}. The local binarization algorithm has the great advantage of taking into account different local illumination conditions that can occur within the interrogation area.

By using an experimental set-up analogous to the one used in the simulations, the approach (23) was validated on POM granular material in a high-viscosity high-density sucrose solution. The granular material, at known volume fractions, was poured in a box containing the sucrose solution. Successively, the container was manually shaken and placed in a specific location to record the image. The high intensity and the high viscosity of the solution allowed obtaining random distribution of the grains avoiding the sedimentation of the granular material. In this way, it was possible to investigate volume fraction values less than the volume fraction at deposit of the granular material, c_{dep} = 0.58÷0.62 (Tab. 3.1). The investigated range was [0.05, 0.62]. 50 different dispersions for each investigated volume fraction and different inclination angles of the light rays were analyzed. An excellent agreement between experimental measurements of c_{2D} and numerical data was found. Different sizes of the

interrogation window were tried. As expected, it was found that the higher is the size of the interrogation window the lower is the root mean square error (RMSE) on the estimation of the c_{3D}.

In this research study, the SOM method was applied to steady dry granular flows. First application of the SOM method was reported in the work of Carleo et al. (2018), which is under revision.

As shown in Tab. 3.2, three different configurations were used. The first experiments were performed using Configuration 1 (Conf. 1) for which the angle incidence of the light rays, ζ, was chosen equal to 30.4°. According to Sarno et al. (2016), in order to reduce effect of the glares on the volume fraction estimation, a mean filter was used with a square neighborhood of size 3 x 3 pixels ($\approx d/5$ x $d/5$). Based on the error analysis carried out by Sarno et al. (2016), the RMSE on the estimation of c_{3D} for the interrogation window area of $16d^2$ is of order of 0.033. Successively, for practical reasons and because the errors on the estimation of c_{3D} were found to be lower, ζ was chosen equal to 25° (Conf. 2). Since information on the errors were not available for ζ = 25° from Sarno et al. (2016), a further experimental investigation in sucrose solution was performed using the same experimental setup of Sarno et al. (2016). For this angle of incidence, the RMSE on the estimation of c_{3D} is of order of 0.023.

Tab. 3.2 - Configurations used in open channel experiments.

Configuration	Inclination of the light rays ζ [°]	Mean filter	RMSE
1	30.4	3 x 3 px	0.033
2	25	3 x 3 px	0.023
3	25	15 x 15 px	0.021

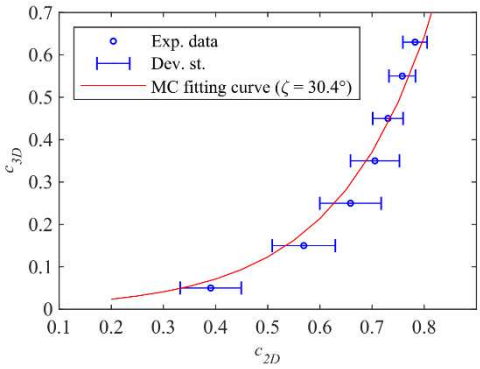

Fig. 3.5 - Comparisons between the experimental data and the relationship obtained with Monte Carlo generations for $\zeta = 30.4°$ (size of the mean filter 3 x 3 pixels). RMSE on c_{3D} is of order of 0.033.

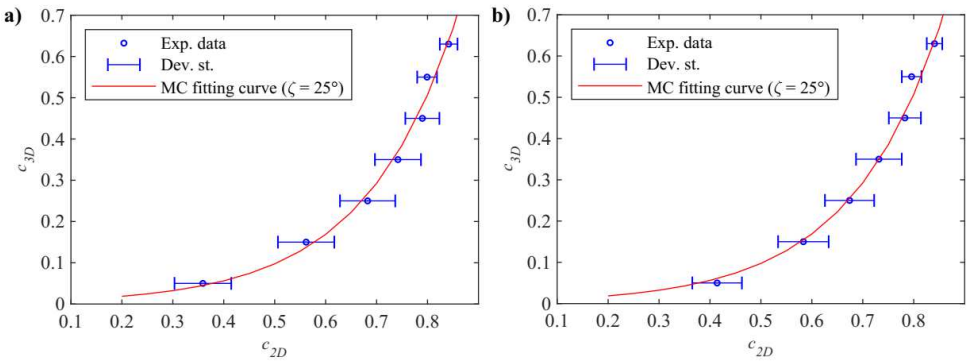

Fig. 3.4 - Comparisons between the experimental data and the relationship obtained with Monte Carlo generations for $\zeta = 25°$: a) size of the mean filter 3 x 3 pixels, RMSE on c_{3D} is of order of 0.023; b) size of the mean filter 15 x 15 pixels, RMSE on c_{3D} is of order of 0.021.

More accurate results were obtained by using a mean filter with square neighborhood of size 15 x 15 pixels, namely $\approx 1d$ x $1d$ (Conf. 3). Comparisons between the experimental data obtained in water-sucrose solution and the exponential stochastic relationship obtained with Monte Carlo generations are shown in Fig. 3.4 for $\zeta = 30.4°$ and in Fig. 3.5 for $\zeta = 25°$.

In order to apply the SOM method in open channel experiments, a preliminary investigation on several grain distributions at the volume fraction at deposit, c_{dep}, is needed to calibrate the threshold s. In the experiments performed in the channel of width W = 8cm, all the three configurations of Tab. 3.2 were used. The calibrations provided s=0.50, s=0.49 and s=0.73 for Conf. 1, Conf. 2 and Conf. 3, respectively. As one can see, the threshold value weakly depends on the inclination angle of the light rays (Conf. 1 and Conf. 2) thanks to the robustness of the local binarization algorithm. However, it significantly changes if one use a different size of the interrogation window of the mean filter (Conf. 3). In the channel of width W = 3cm, Conf. 3 was used and the calibrated threshold was s=0.73. It is worth underlining that the threshold needs to be periodically recalibrated since the optical properties of the Plexiglas sidewall could change in time.

In order to obtain near-wall volume fraction profiles with an appropriate spatial resolution, the interrogation window needs to be as little as possible along the flow depth. Therefore, the images recorded at the sidewall were binned in slices of width 16d and height 1d with an area of the interrogation window of $16d^2$. 50% overlapping slices were used so that the spatial resolution of the volume fraction measurements was d/2.

3.4 Experimental procedure and list of the experiments

Before each run, the gate opening was carefully adjusted and the granular material was loaded into the reservoir. Then, the shutter was manually

removed and the granular medium was let flow down under gravity in the channel. After an initial transient state, steady state flow conditions were reached. A preliminary test was carried out to measure flow depth, h, and the mass flow rate, Q_m so as to detect the steady state time interval. At this stage, the sole side camera was used to record the flow at a sampling rate of 100 Hz. A steady state time interval lasting several seconds was observed in all the experiments. Once h was determined (length scale $\approx 2 \times 10^{-4}$ m/pixel), the LED lamp was positioned in order to properly illuminate both the sidewall and the free surface. After this test, four repetitions were performed. Both cameras were employed to record the flow at the higher sampling rate of 1000Hz.

The experiments performed over the fixed bed are presented in Tab. 3.3 and 2.4. All the runs were carried out in the 8cm-wide channel. The investigated gate openings ranged from 5cm to 14cm. In the experiments with an inclination angle of the channel equal to 30° (Tab. 3.3), three different fixed basal surfaces were studied: a smooth Bakelite surface (S); a rough sandpaper surface (P40); a granular surface (G). In the experiments with an inclination angle of the channel equal to 35° (Tab. 3.4), five different fixed basal surfaces were investigated: a smooth Bakelite surface (S); three different sandpaper surfaces (P40, P60 and P100); a granular surface (G). Since the SOM method was developed for chute applications after some experiments were already performed, volume fraction measurements were not available for the P40_30 and the G_30 experimental campaigns (Tab. 3.3). The list of the experiments performed over the erodible bed is shown in Tab. 3.5.

Tab. 3.3 - List of experiments performed over the fixed basal surface with an inclination angle of the channel $\alpha = 30°$. l represents the average characteristic length of roughness of the employed basal surface.

Experimental campaign ID	Exp. ID	Gate opening [m]	Basal surface	Inclination angle of the channel α [°]	SOM configuration
S_30	5S_30	0.05	Bakelite (S), $l << 10$ μm	30	Conf. 1
	6S_30	0.06			
	7S_30	0.07			
	8S_30	0.08			
	10S_30	0.10			
	12S_30	0.12			
	14S_30	0.14			
P40_30	5P40_30	0.05	P40 Sandpaper (P40), $l = 425$ μm	30	Volume fraction measurements not available
	6P40_30	0.06			
	7P40_30	0.07			
	8P40_30	0.08			
	10P40_30	0.10			
	12P40_30	0.12			
	14P40_30	0.14			
G_30	5G_30	0.05	Grain (G), $l = 1.65$ mm	30	Volume fraction measurements not available
	6G_30	0.06			
	7G_30	0.07			
	8G_30	0.08			
	10G_30	0.10			
	12G_30	0.12			
	14G_30	0.14			

Tab. 3.4 - List of experiments performed over fixed basal surface with an inclination angle of the channel α = 35°. l represents the average characteristic length of roughness of the employed basal surface (continued on the next page).

Experimental campaing ID	Exp. ID	Gate opening [m]	Basal surface	Inclination angle of the channel α [°]	SOM configuration
S_35	5S_35	0.05	Bakelite (S), l << 10μm	35	Conf. 2
	6S_35	0.06			
	7S_35	0.07			
	8S_35	0.08			
	10S_35	0.10			
	12S_35	0.12			
	14S_35	0.14			
P40_35	5P40_35	0.05	P40 Sandpaper (P40), l = 425 μm	35	Conf. 2
	6P40_35	0.06			
	7P40_35	0.07			
	8P40_35	0.08			
	10P40_35	0.10			
	12P40_35	0.12			
	14P40_35	0.14			
P60_35	5P60_35	0.05	P60 Sandpaper (P60), l = 269 μm	35	Conf. 2
	6P60_35	0.06			
	7P60_35	0.07			
	8P60_35	0.08			
	10P60_35	0.10			
	12P60_35	0.12			
	14P60_35	0.14			
P100_35	5P100_35	0.05	P100 Sandpaper (P100), l = 162 μm	35	Conf. 2
	6P100_35	0.06			
	7P100_35	0.07			
	8P100_35	0.08			
	10P100_35	0.10			
	12P100_35	0.12			
	14P100_35	0.14			

Tab. 3.4 - List of experiments performed over fixed basal surface with an inclination angle of the channel α = 35°. l represents the average characteristic length of roughness of the employed basal surface (continued from preceding page).

Experimental campaing ID	Exp. ID	Gate opening [m]	Basal surface	Inclination angle of the channel α [°]	SOM configuration
G_35	5G_35	0.05	Grain (G), l = 1.65 mm	35	Conf. 2
	6G_35	0.06			
	7G_35	0.07			
	8G_35	0.08			
	10G_35	0.10			
	12G_35	0.12			
	14G_35	0.14			

Tab. 3.5 - List of the experiments performed over the erodible bed.

Experimental campaign ID	Exp. ID	Gate opening [m]	Channel width W [m]	SOM configuration
E_8	6E_8	0.06	0.08	Conf. 3
	8E_8	0.08		
	10E_8	0.10		
	12E_8	0.12		
	14E_8	0.14		
	16E_8	0.16		
	18E_8	0.18		
E_3	16E_3	0.16	0.03	Conf. 3
	18E_3	0.18		
	20E_3	0.20		
	22E_3	0.22		
	24E_3	0.24		
	26E_3	0.26		
	28E_3	0.28		
	30E_3	0.30		
	32E_3	0.32		
	34E_3	0.34		

4. Results of the laboratory investigation on granular flows over fixed bed

The laboratory investigation was mainly devoted to study of the effects of the boundaries on the dynamics of steady chute dry granular flows. The experimental campaigns performed over fixed bed are listed in Tab. 4.1. All the runs were carried out in the same Plexiglas channel with width W = 8cm. Five different fixed basal surfaces and two different inclination angles of the chute permitted to study the influence of various kinematic boundary conditions (KBC) at the bed. Seven gate openings in the range [5cm, 14cm] were investigated for each experimental campaign. Four repetitions were performed for each analyzed gate opening for a total of 224 runs. A steady state time interval, lasting several seconds, was observed in all the runs. All the measurements were taken within the steady state. The two main variables which influence the dynamics of dry granular flows were investigated, namely velocity and volume fraction. Velocity was measured at the sidewall

Tab. 4.1 – List of the experimental campaigns performed over fixed bed.

Fixed bed, W = 8cm		
Slope angle / Basal surface	**30°**	**35°**
Bakelite	S_30	S_35
P40	P40_30	P40_35
P60	-	P60_35
P100	-	P100_35
Granular bed	G_30	G_35

and at the free surface while volume fraction was measured at the sidewall. The phenomenon under study exhibited some features that are in common in all the experiments, included the experiments on erodible bed. In order to enlighten these characteristics, the non-processed measurements related to a repetition of the 7S_30 experiment are presented as an example. Such measurements were taken in a time interval of 1s within the steady state. We observed that, choosing a different time interval in the steady state does not induce any significant variation in the values of all the measured quantities. The instantaneous PIV measurements at the sidewall are shown in Fig. 4.1. The longitudinal component of the sidewall velocity, namely along the x-axis (see the reference system in Fig. 3.1), u_x, is plotted against the dimensionless distance from the basal surface along the z-axis, z/d, where d is the grain diameter. The u_x velocity profile is shown in Fig. 4.1a. The grey point cloud corresponds the instantaneous PIV measurements. The blue line corresponds to the time averaged velocity, obtained by averaging the instantaneous velocities over the chosen steady state time interval. The

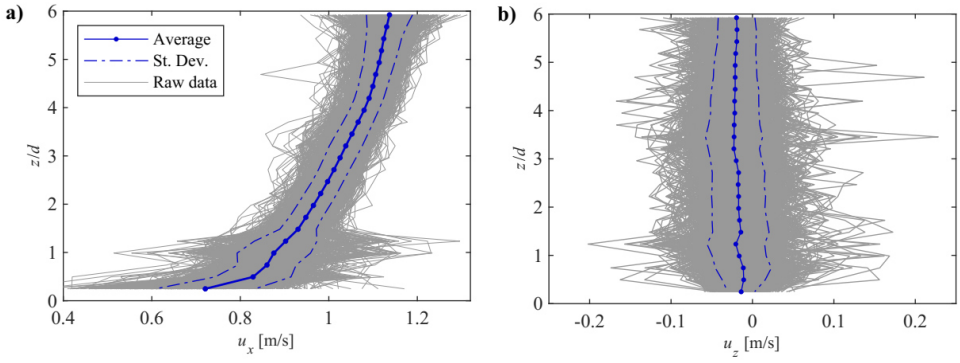

Fig. 4.1 - Non-processed sidewall PIV measurements for a repetition of the 7S_30 experiment: a) longitudinal velocity measurements, b) vertical velocity measurements.

scatter of the cloud is one order of magnitude larger than the PIV accuracy indicating that velocity fluctuations occur in the *x*-direction. It should be kept in mind that, very close to free surface, the PIV measurements could be affected by some errors due to small fluctuations of the free surface level. As you can see, the time averaged u_x profile is a strictly increasing function (i.e. $\partial u_x / \partial z \geq 0$).

In Fig. 4.1b, the vertical component of the sidewall velocity, u_z, is plotted against z/d. Velocity fluctuations can be also observed along the *z*-direction. The time averaged u_z profile reveals that, on average, the grains tend to go toward the basal surface ($u_z < 0$). This means that momentum and mass fluxes occur along the flow depth, as well. By comparing the order of magnitude of u_x and u_z, one can say the motion develops prevalently in the *x*-direction.

The time averaged one dimensional shear rate, $\dot{\gamma}$, can be calculated using Eq. (2) in a discretized form, according to the spatial resolution of the PIV measurements, Δz. The central difference formula is applied:

$$\dot{\gamma}(z) = \frac{u_x(z + \Delta z) - u_x(z - \Delta z)}{2\Delta z} \qquad (25)$$

At the free surface and at the basal surface, the backward and forward formula was used, respectively.

The granular temperature, *T*, can be calculated using the standard deviation of the velocity measurements (Eq. (6)). Since velocity fluctuation measurements along the *y*-direction are inaccessible, except at the free surface, similar to Jesuthasan et al. (2006), we assumed that $\left\langle \left(u_y'\right) \right\rangle \approx \left\langle \left(u_z'\right) \right\rangle$. Furthermore, the statistically stationary system under study is assumed to

be ergodic so the ensamble averages of the fluctuation velocities are equivalent to the respective time averages. The ensamble averages of the fluctuation velocities can be estimated using the instantaneous measurements of $u_i^{'}$, where i is a generic direction, averaged within the steady state time interval. By neglecting the rotational and vibrational terms, the granular temperature T at the sidewall can be estimated as follows

$$T(z) = \frac{\left\langle \left(u_x^{'}(z)\right)^2 \right\rangle + 2\left\langle \left(u_z^{'}(z)\right)^2 \right\rangle}{3} \qquad (26)$$

Since the relative error on the velocity measurements is about 0.004 m/s and the minimum velocity fluctuations are typically of order of 0.02 m/s (Sect. 3.2), the typical relative error on the granular temperature estimation is less than 4% (Capart et al. 2002).

The instantaneous PIV measurements at the free surface are reported in Fig. 4.2. In Fig. 4.2a, the longitudinal component of the velocity at the free surface, $u_x|_{z=h}$, is plotted against the dimensionless distance from the

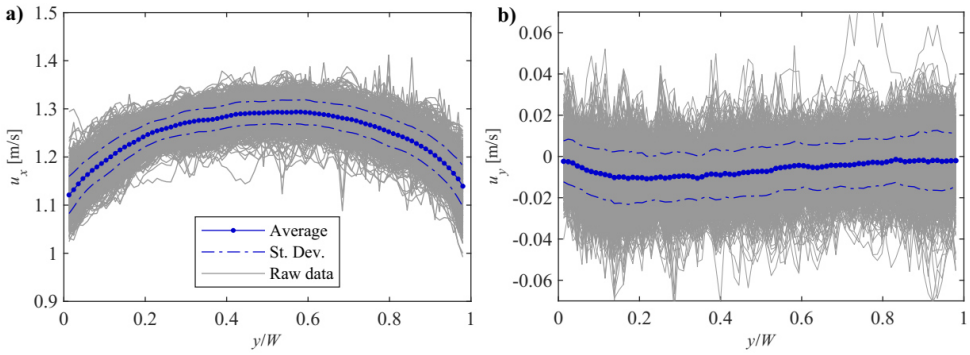

Fig. 4.2 - Non-processed free surface PIV measurements for a repetition of the 7S_30 experiment: a) longitudinal velocity measurements, b) transversal velocity measurements.

sidewall y/W, where y is the dimensional distance from the sidewall and W is the channel width. The time averaged velocity profile exhibits a typical parabolic shape: the maximum velocity is observed at $y=W/2$ while the minimum velocities at the sidewalls, accounting for a non-negligible sidewall effect, due to the friction, on the velocity field. This profile is qualitatively in agreement with other experimental works on dry granular flows (Jop et al. 2005; Baker et al. 2016). In Fig. 4.2b, the transverse component of the velocity at the free surface, $u_y\big|_{z=h}$, is plotted against y/W.

Very small values of the time averaged transverse velocity were measured at the free surface, confirming that the shear mainly occurs in the x-z plane.

Four repetitions were performed for each experiments. The experimental repeatability was tested through the relative standard deviation of the values of both the mass flow rate, Q_m, and the flow depth, h, measured in each repetition within the same steady state time interval. By considering the entire data set related to the experimental campaigns of Tab. 4.1, the relative standard deviation of Q_m and of h was less than 4% and less than 1.5%, respectively. In Fig. 4.3 and Fig. 4.4, sidewall and free surface profiles corresponding to the four repetitions of the 7S_30 experiment are presented, respectively. As you can see, the profiles strongly overlap indicating an excellent repeatability among the four repetitions.

All the measured quantities presented in the following sections are thus the result of two averages: a time-average over the steady state time interval of 1s and an ensamble-average over the four repetitions.

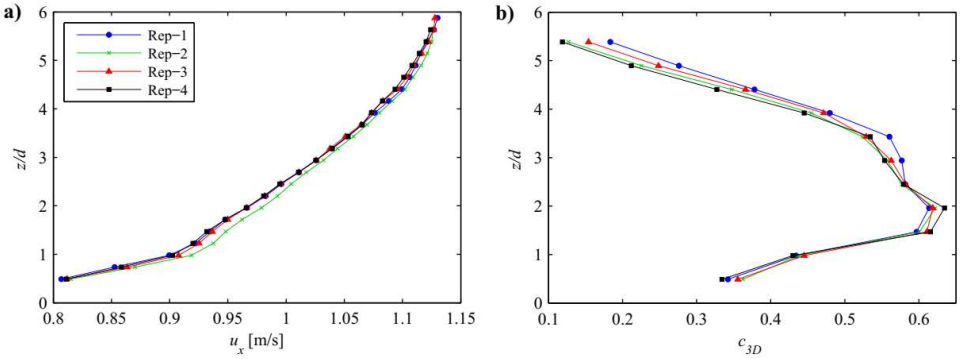

Fig. 4.3 - Sidewall profiles corresponding to all the four repetitions of the 7S_30 experiment: a) longitudinal velocity profiles, b) volume fraction profiles.

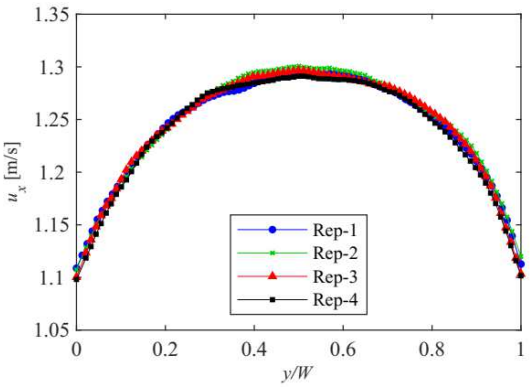

Fig. 4.4 - Free surface longitudinal velocity profiles corresponding to all the four repetitions of the 7S_30 experiment.

It is worth remembering that for the P40_30 and G_30 experimental campaigns volume fraction measurements were not available, since the SOM method was developed later for chute applications. We decided to first present the results related to the experiments for which volume fraction measurements are available, namely those carried out with $\alpha = 35°$, and then the others, namely those with $\alpha = 30°$. Despite the order of presentation does not correspond to the chronologic order of performance of the experiments,

this allowed a better explanation of some aspects of the dynamics for the experiments performed with $\alpha = 30°$.

In Sect. 4.1, results of the experiments carried out over the fixed bed with an inclination angle of the chute $\alpha = 35°$ are presented. Such results were recently submitted to the 7th International Conference on Debris-Flow Hazards Mitigation.

In Sect. 4.2, the experiments carried out over the fixed bed with an inclination angle of the chute $\alpha = 30°$ are presented. Results of the velocity measurements were published on Rock Mechanics and Rock Engineering Journal (Sarno et al. 2018a, DOI: 10.1007/s00603-017-1311-2). Results of the first application of the SOM method to chute dry granular flows over the smooth bed were recently submitted to Advanced Powder Technology Journal (Carleo et al. 2018, in the references).

4.1 Experiments over fixed basal surface: inclination angle of the chute $\alpha = 35°$

In this section, the experiments performed over the fixed bed in the 8cm-wide channel tilted with an inclination angle $\alpha = 35°$ are presented.

The employment of different fixed basal surface allows investigating different kinematic boundary conditions (KBC) at the bed. In case of smooth Bakelite surface (S), a slip condition, namely a sliding of the grains on the basal surface, was analyzed. The fixed granular bed (G) imposed a no-slip KBC. By employing three different sandpaper linings (P40, P60 and P100)

an intermediate no-slip KBC with rolling and small saltation of the grains was studied. In the entire data set, a steady state time interval lasting several seconds was always observed. All the measurements presented here were thus time-averaged over the steady state time interval of 1s and, then, ensamble-averaged over the four repetitions. In Tab. 4.2, the mass flow rate, Q_m, the flow depth, h, and the inclination angle of the free surface with respect to the inclination of the chute, $\beta = \arctan(\partial h/\partial x)$, are reported for each experiment. The small values of $|\beta|$ indicate that all the flows are close to the fully developed uniform state. In Fig. 4.5, flow depth is plotted against the mass flow rate for each experiment. As one could expect, for a fixed flow depth, the higher is the basal roughness the lower is the mass flow rate. Moreover, in case of smooth bed, Q_m seems to increase linearly with h while, in case of sandpaper and granular fixed bed, it increases less than linear. One can observe that the curves corresponding to the analysed sandpaper linings overlap themselves. The inclination angles of the free surface show similar values with a fixed gate opening, as well. This strong correspondence among the flow quantities can be also seen by both looking at the velocity and volume fraction profiles. In Fig. 4.6, the profiles related to the gate openings of 7cm (Fig. 4.6a, b, c) and 12cm (Fig. 4.6d, e, f) are reported for the analyzed sandpaper linings as an example. As one can see, all the quantities measured both at the sidewall and at the free surface show no significant variations. This means that, in the range of analyzed characteristic length of roughness l (l/d = 0.05÷0.13, where d is the grain diameter), a change in the bed roughness did not induce significant

Tab. 4.2 - List of all the experiments performed over the fixed bed in the 8cm-wise channel tilted with inclination angle $\alpha = 35°$ (continued on the next page).

Experimental campaign ID	**Exp. ID**	**Gate opening [m]**	**Basal surface**	Q_m **[g/s]**	h **[m]**	β **[°]**
S_35	5S_35	0.05	Bakelite (S), $l << 10$ μm	1084	0.009	-0.15
	6S_35	0.06		1417	0.012	-0.24
	7S_35	0.07		1725	0.016	-0.63
	8S_35	0.08		2124	0.02	-0.8
	10S_35	0.10		2717	0.027	-1.32
	12S_35	0.12		3332	0.034	-1.74
	14S_35	0.14		4243	0.044	-2.44
P40_35	5P40_35	0.05	P40 Sandpaper (P40), $l = 425$ μm	858	0.018	1.04
	6P40_35	0.06		1146	0.021	0.45
	7P40_35	0.07		1440	0.023	-0.03
	8P40_35	0.08		1799	0.027	-0.24
	10P40_35	0.10		2353	0.035	-0.87
	12P40_35	0.12		2819	0.042	-1.16
	14P40_35	0.14		3399	0.05	-1.55
P60_35	5P60_35	0.05	P60 Sandpaper (P60), $l = 269$ μm	896	0.017	0.57
	6P60_35	0.06		1181	0.02	0.24
	7P60_35	0.07		1510	0.023	-0.23
	8P60_35	0.08		1780	0.027	-0.61
	10P60_35	0.10		2463	0.036	-1.19
	12P60_35	0.12		3037	0.045	-1.6
	14P60_35	0.14		3550	0.057	-1.98
P100_35	5P100_35	0.05	P100 Sandpaper (P100), $l = 162$ μm	912	0.017	0.71
	6P100_35	0.06		1206	0.02	0.24
	7P100_35	0.07		1511	0.023	-0.13
	8P100_35	0.08		1861	0.027	-0.51
	10P100_35	0.10		2541	0.035	-1.24
	12P100_35	0.12		3153	0.045	-1.42
	14P100_35	0.14		3730	0.053	-1.92

Tab. 4.2 - List of all the experiments performed over the fixed bed in the 8cm-wise channel tilted with inclination angle $\alpha = 35°$ (continued from the preceding page).

Experimental campaign ID	Exp. ID	Gate opening [m]	Basal surface	Q_m [g/s]	h [m]	β [°]
G_35	5G_35	0.05	Grain (G), l = 1.65 mm	773	0.019	0.84
	6G_35	0.06		1038	0.023	0.15
	7G_35	0.07		1297	0.027	-0.60
	8G_35	0.08		1555	0.031	-0.58
	10G_35	0.10		2263	0.040	-0.87
	12G_35	0.12		2635	0.050	-1.60
	14G_35	0.14		3066	0.059	-1.91

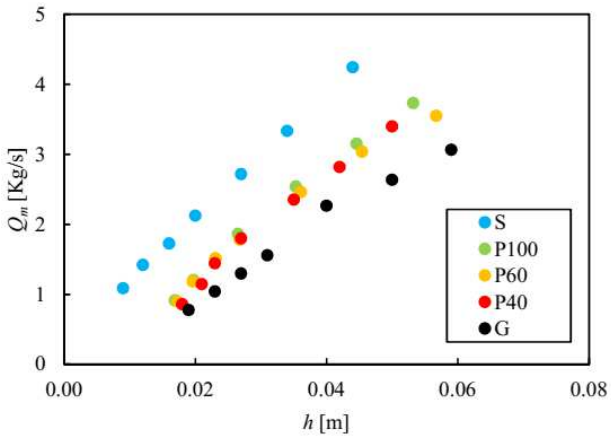

Fig. 4.5 - Flow depth plotted against the corresponding mass flow rate for all the analysed basal roughnesses.

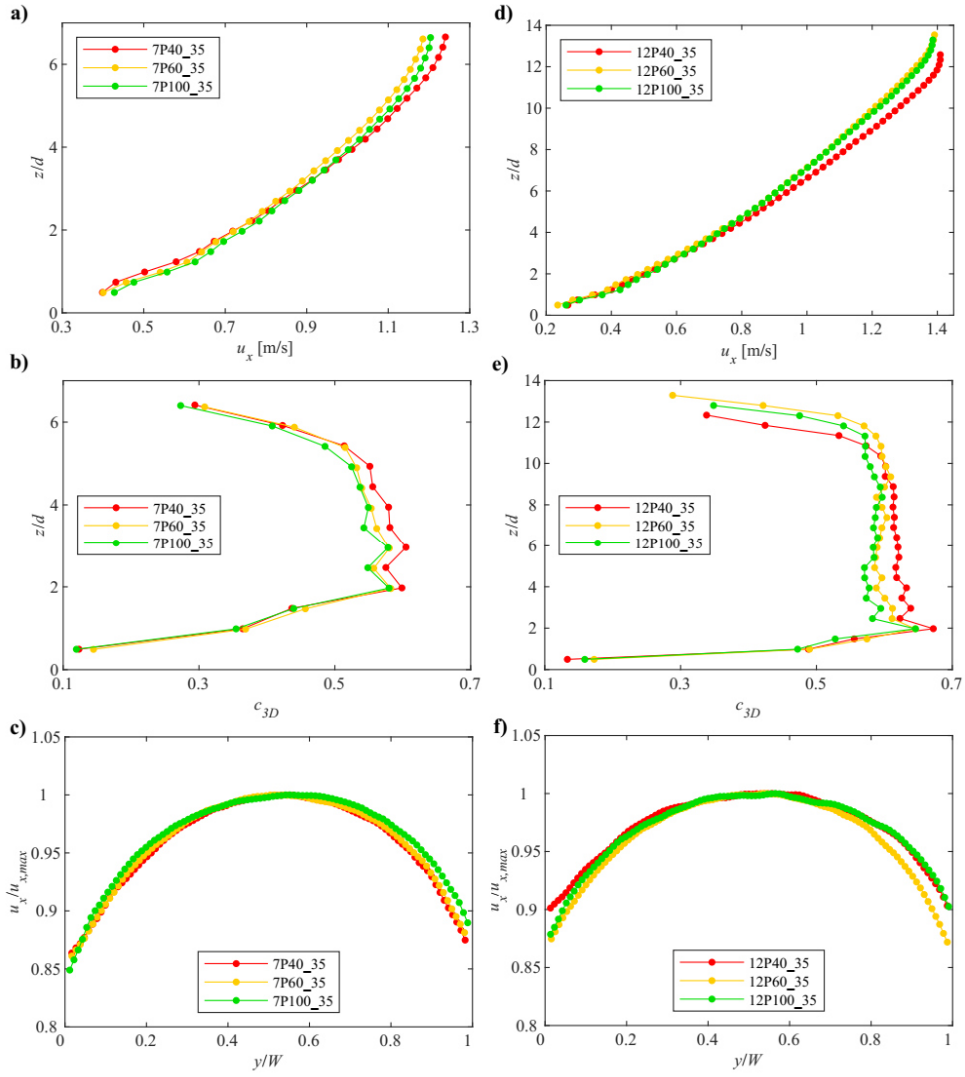

Fig. 4.6 – Examples of profiles related to the analysed sandpaper linings P40, P60 and P100. Sidewall longitudinal velocity, volume fraction and free surface longitudinal velocity profiles for the gate openings of 7cm (a, b, c) and 12cm (d, e, f).

variations in the dynamics. The KBC occurring at the bed is qualitatively the

same for all the analyzed sandpaper linings inducing the same dissipation mechanisms within the granular body.

In the following, the different KBCs will be analyzed in detail. Since the sandpaper basal surfaces show very similar profiles according to the same KBC at the basal surface, only the measurements related to the P40 bed will be presented.

4.1.1 Sidewall measurements: experiments over smooth bed (S_35)

The employment of the smooth Bakelite basal surface permitted to investigate a slip condition with negligible grain rolling at the bed. All the sidewall profiles are presented in Fig. 4.7. For some experiments, few PIV measurements immediately below the free surface are not reported, since the strong oscillation of the free surface induced some inaccuracies.

By looking at the sidewall profiles, three regions can be identified:

- a lower region, approximately 1d-thick, near the basal surface, where a shear band occurs and volume fraction is small due to the dilatancy and due to the presence of the fixed bed;
- a middle region (hereafter called *core region*), spanning from $z \approx 1d$ to $2d \div 4d$ below the free surface, where the sidewall longitudinal velocity exhibits an approximately linear trend and volume fraction is

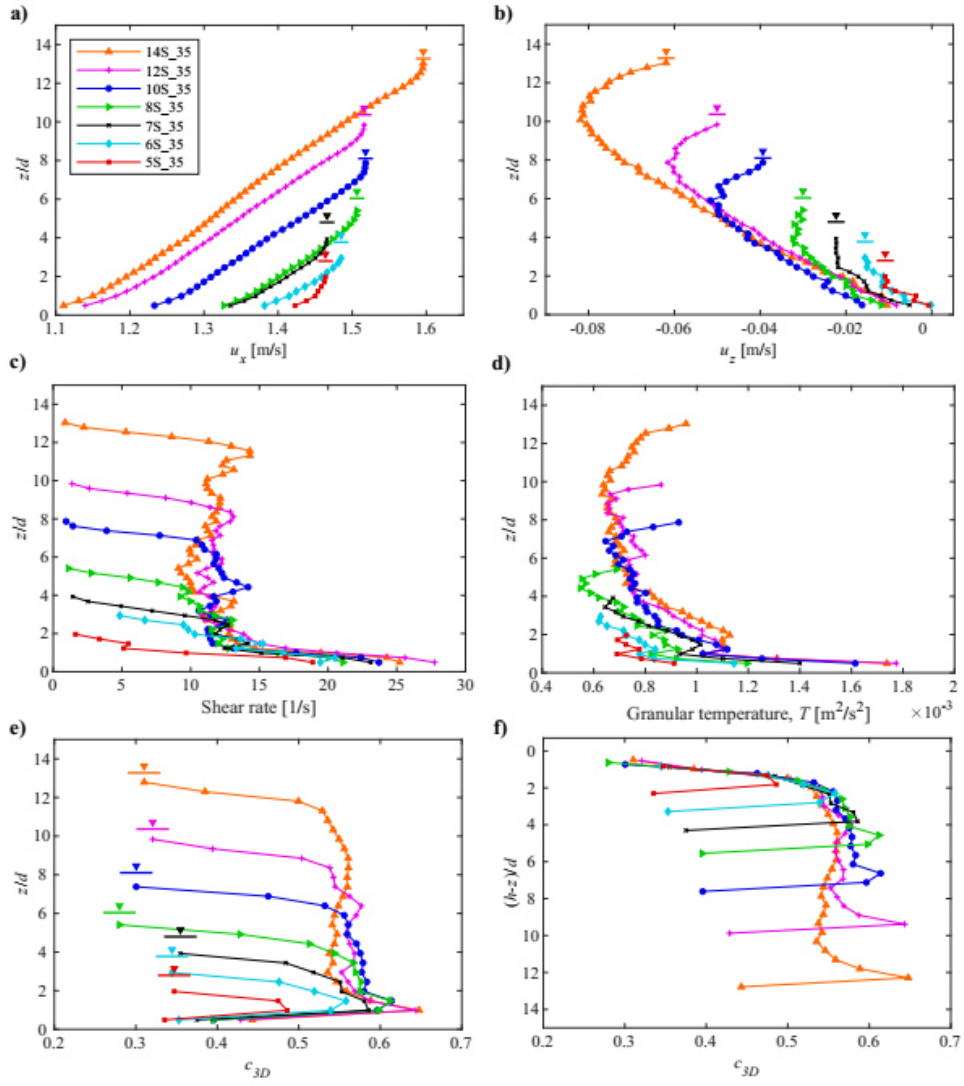

Fig. 4.7 - Sidewall profiles for the S-bed with inclination angle of the chute α = 35°: a) longitudinal velocity profiles; b) vertical velocity profiles; c) shear rate profiles; d) granular temperature profiles; e) volume fraction profiles; f) volume fraction profiles aligned at the free surface.

approximately constant and slightly lower than the loose random

packing of the granular material, namely ≈0.6;

- an upper region, where the sidewall longitudinal velocity increases less than linear and volume fraction reaches lower values.

In the lower region, a shear band occurs. This is clearly visible in Fig. 4.7c, where the shear rate, $\dot{\gamma}$, shows the highest values. Grain agitation is high as confirmed by the high values of the granular temperature, T (Fig. 4.7d). In this region, volume fraction, c_{3D}, is small due to the presence of the shear band (Fig. 4.7e). The basal slip, also verified by naked-eye observations of the recorded videos, is due to the small angle of friction between grains and Bakelite (φ_{gb}=14.5°) compared with the internal angle of friction of the POM material (φ=27°). The exact value of the basal slip velocity, u_{slip}, is inaccessible with the PIV technique due to the spatial averaging. We found that longitudinal velocity at d/2 from the basal surface, $u_x\big|_{z=d/2}$, gives a good estimation of the slip velocity since the first layer of grains exhibit almost no-rolling, so $u_{slip} \approx u_x\big|_{z=d/2}$. In Fig. 4.8, u_{slip} is plotted against h. The clear decreasing trend with the flow depth can be explained by the effect of the sidewall friction, which is comparable with the friction exerted by the bed (angle of friction Plexiglas walls-grain φ_w = 19.5°). When the flow depth, namely the vertical normal pressure, σ_z, increases, the resistance exerted by the sidewall increases, as observed by Sarno et al. (2018a). In order to balance momentum along the x-direction, shear stress at the bed, $\tau_{xz}\big|_{z=0}$, should decreases. This means that the effective friction at the basal surface, $\mu_{eff} = (\tau_{xz}/\sigma_z)\big|_{z=0}$, should decreases with h, as the slip velocity does. This is in accordance with the numerical investigations performed by Artoni

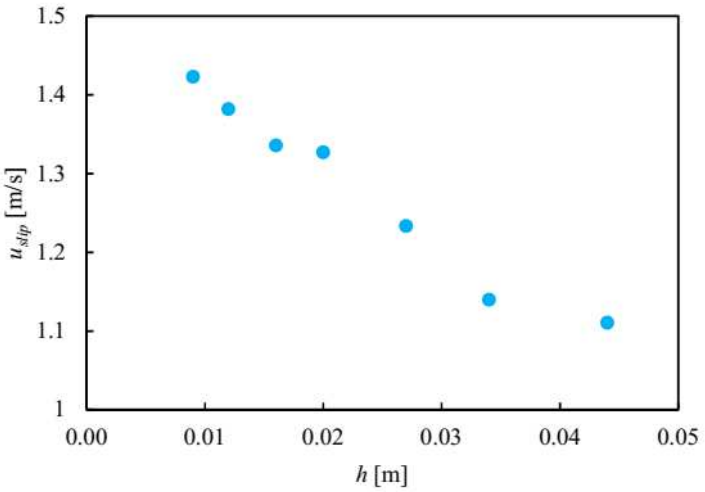

Fig. 4.8 - Flow depth plotted against the slip velocity.

et al. (2009, 2012, and 2015), in which a strictly increasing relationship between μ_{eff} and the slip velocity was found.

Immediately above the lower region, a dense frictional-collisional regime takes place. Volume fraction shows a slightly lower value than the loose random packing of the granular material (≈0.6) and it keeps approximately constant along z. In the core layer, all the c_{3D} profile collapse into a unique profile so c_{3D}=0.6 could be viewed as a saturation value. The volume fraction profile is substantially in agreement with other volume fraction measurements in free surface granular flows on rough inclined plane (Pouliquen 1999). In the core region, the u_x-profile exhibits an approximately linear trend with z, as confirmed by the approximately constant values of the shear rate ($\dot{\gamma} = 10 \div 15$ 1/s). In this layer, the grain dilatancy is weak and non-local effects, such as the force chains (Mills et al.

1999; da Cruz et al. 2005), could develop. As shown by Sarno et al. (2018a), both non-local effects and the sidewall resistances can induce different shapes of the velocity profiles. In the 5S_35, 6S_35 and 7S_35 experiments, the core layer has not room enough to develop. Volume fraction do not reach its saturation value while velocity exhibits a more concave profile ($\partial_{zz} u_x \leq 0$), as shown by the decreasing trend of $\dot{\gamma}$ with z. As soon as the flow depth is high enough and the resistance exerted by the sidewalls becomes relevant, a core layer takes place and the velocity shows a linear trend with z. Granular temperature keeps approximately constant along z exhibiting values of $\approx 0.5 \div 1$ m^2/s^2.

In the upper region, a more dilute regime occurs. Higher velocity and lower normal stresses cause more grain collisions. Velocity increases less than linear, as shown by the decreasing trend of the shear rate with z, while volume fraction rapidly decreases with z. The decreasing trend of the volume fraction below the free surface is accordance with other experimental works on dry granular flows (Ahn et al. 1991; Ancey 2001b). To underline the similarities in the volume fraction profiles in different experiments, all the c_{3D} profiles were aligned at the free surface, as shown in Fig. 4.7f. As one can see, the upper part of the profiles collapse into a unique profile. Moreover, the upper collisional layer exhibit an approximately constant thickness of about $2d \div 4d$. In Fig. 4.7b, the u_z profiles are presented. The grains tend to go toward the basal surface exhibiting a non-null downward velocity at the free surface. The downward velocity shows its maximum at about $2d \div 4d$ from the free surface, namely in the nearest of the interface between the dilute layer and the core layer. This occurs because a dense core

layer with high volume fraction establishes so the downward velocity cannot further increase. The more collisional behaviour of the granular flow in the upper layer can be also observed in the T values, which are slightly higher with respect to the core region.

4.1.2 Sidewall measurements: experiments over P40 bed (P40_35)

By increasing the basal roughness, a different KBC can be observed at the bed. The employment of the analyzed sandpaper linings allows studying a no-slip condition with rolling and small saltation of the grains on the basal surface. Such phenomena occur because the investigated characteristic lengths of roughness, l, are significantly smaller than the grain size ($l/d \approx 0.05 \div 0.13$). Rolling and saltation are progressively inhibited by increasing the flow depth, namely by increasing the normal pressures at the bed.

As previously shown, with a fixed gate opening, no significant variations in both velocity and volume fraction measurements were observed in the experiments performed over the different analyzed sandpaper beds. Therefore, only the sidewall profiles related to the P40_35 experimental campaign are reported (Fig. 4.9). A rheological stratification slightly different from the slip KBC (Sect. 4.1.1) can be observed. In the lower region, with a thickness of $\approx 1d \div 2d$, a strong agitation of the grains occurs and high values of the shear rate can be seen (Fig. 4.9c and Fig. 4.9d). Soon

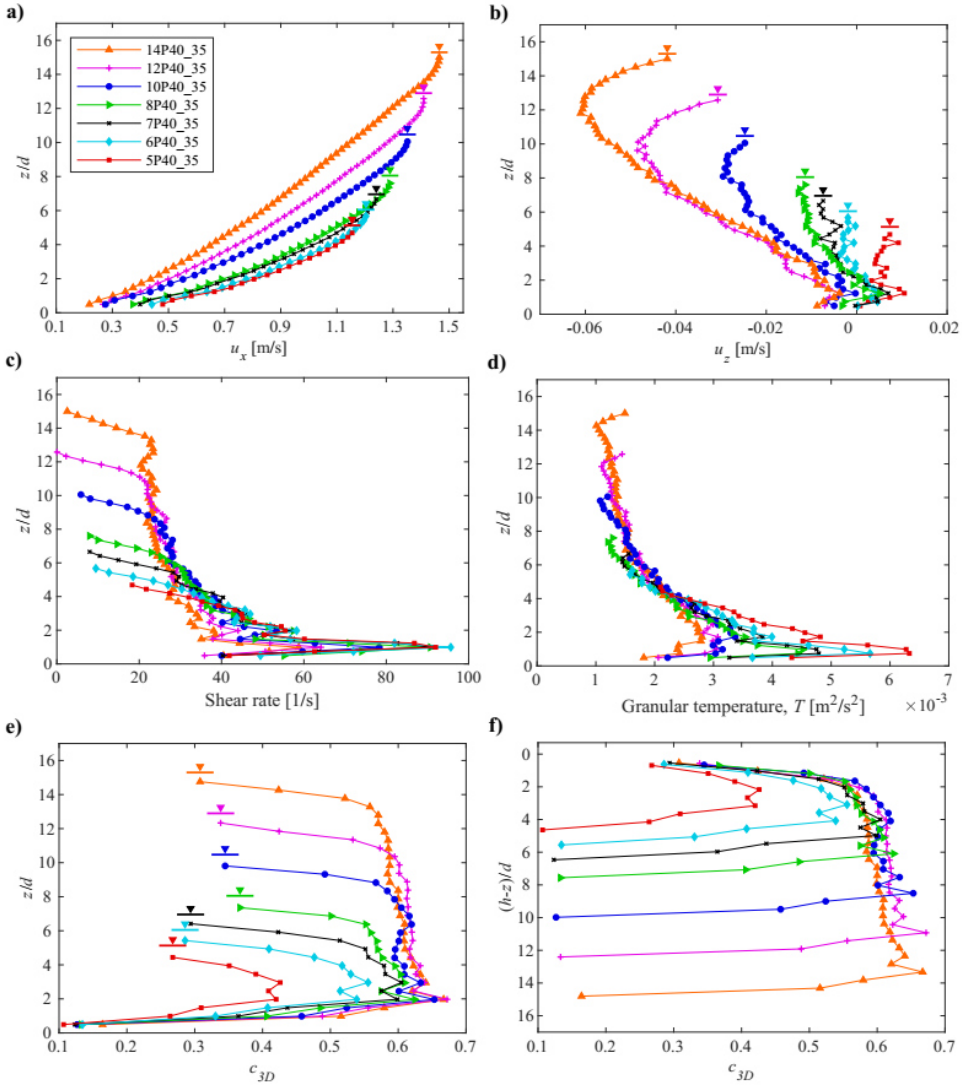

Fig. 4.9 - Sidewall profiles for the P40-bed with inclination angle of the chute α = 35°: a) longitudinal velocity profiles; b) vertical velocity profiles; c) shear rate profiles; d) granular temperature profiles; e) volume fraction profiles; f) volume fraction profiles aligned at the free surface.

above the basal surface, volume fraction is very small but it rapidly increases

with z (Fig. 4.9e).

In the central zone, a denser flow regime takes place. As already observed in case of the S-bed, volume fraction keeps approximately constant with z, exhibiting the saturation value of ≈0.6. Differently from the smooth case, the rough basal roughness is a source of great agitation and shear (Fig. 4.9c, d). T and $\dot{\gamma}$ are higher with respect to the S-bed. Moreover, the perturbation propagates in the core layer from the rough bed, z=0, up to $z \approx 5d \div 6d$. In this zone, when the flow depth increases, namely the confining effect of normal pressures increases, T and $\dot{\gamma}$ decrease. For $z > 5d \div 6d$, both shear rate and granular temperature curves seems to collapse into their respective unique profiles. Therefore, $z \approx 5d \div 6d$ can be considered a distance of influence, z_{in}, of the rough bed for the P40_35 experimental campaign. In the experiments with h lower than z_{in}, the core layer do not develop, since the agitation induced by the rough basal surface is high and the grains exhibit a more dilute behavior. The velocity profiles exhibit a concave shape along the whole flow depth (Fig. 4.9a). In the experiments 8P40_35 to 14P40_35 for which the flow depth is higher than the distance of influence of the rough bed, the longitudinal velocity exhibits a more linear trend in the core layer, due to both the sidewall resistances and the normal pressures. However, the linearization of the sidewall longitudinal velocity profiles is not so evident. Only in the 14P40_35 experiment, which is the experiments with the highest flow depth, a linear trend of the longitudinal velocity is observed soon beneath the upper collisional layer, namely quite far from the bed ($\dot{\gamma} = 20 \div 25$ 1/s).

The upper collisional layer of approximately constant thickness forms in all the experiments in which a core layer developed, as in case of the smooth bed. In the upper layer, c_{3D} exhibits the same decreasing trend with z in all the experiments, as shown by the collapse of the volume fraction profiles if aligned at their respective free surfaces (Fig. 4.9f). The grains move toward the basal surface exhibiting a downward velocity peak at about $2d \div 4d$ from the free surface, namely at the interface between the upper layer and the core layer, as in case of slip KBC. In the experiments with low flow depth, the vertical velocity is almost zero along z (Fig. 4.9b). In the 5P40_35 experiment, which is the experiments with the lowest flow depth, u_z is positive all along the flow depth indicating that the grains are moving away from the basal surface. This means that, when the normal pressure, namely the flow depth, is small enough, the agitation induced by the basal roughness could cause an expansion of the granular flow, namely a decrease of the average volume fraction (Sheng et al., 2011).

4.1.3 Sidewall measurements: experiments over granular bed (G_35)

By moving from a smooth bed (S) to a more rough bed (P40), the KBC at the bed changed from sliding to rolling and saltation of the grains. Since the roughness of the fixed granular bed (G) is higher than P40, one would expect more saltation of the grains at the basal surface. Instead, a no-slip kinematic boundary condition with very weak saltation was observed. The voids of the bumpy granular bed allows the interlocking of the grains at the basal surface

so the saltation of the grains is almost entirely inhibited (except in the 5G_35 and 6G_35 experiments). This probably occurs because the characteristic length of roughness l, together with flow depth and the sidewall resistances, is not enough to determine the KBC. One should compare l with the grain diameter d: if l and d are of the same order of magnitude, the size of the voids is large enough to induce the interlocking of the particles at the bed. It should be underlined that grain saltantion could have been inhibited, with respect to the P40 bed, also by the dumping effect of the silicone used for gluing grains at the fixed bed. Moreover, the different shape of the sand grains used in the fabrication of the P40 lining with respect to a more spherical shape of the grains used in the bumpy bed could have had some effect on the occurrence of the KBC.

The sidewall profiles related to the G_35 experimental campaign are presented in Fig. 4.10. Owing to the strong interlocking of the particles, velocity at the basal surface is almost null (Fig. 4.10a). Soon above the granular bed, volume fraction reaches the saturation value (≈0.6) and it keeps constant along the flow depth up to $3d \div 4d$ from the free surface (Fig. 4.10e). As already observed in case of the P40 bed, the strong agitation induced by the basal roughness propagates along z and up to $\approx 9d \div 10d$ from the bed. The distance of influence of the fixed granular bed in the G_35 experimental campaign, z_{in}, is higher than z_{in} for the P40_35 campaign (Fig. 4.10d). This could be probably due to the dilatancy effect exerted by the fixed bumpy bed that could be more relevant with respect to a sandpaper lining. Actually, other physical reasons that could explain the difference in z_{in} have not been found yet.

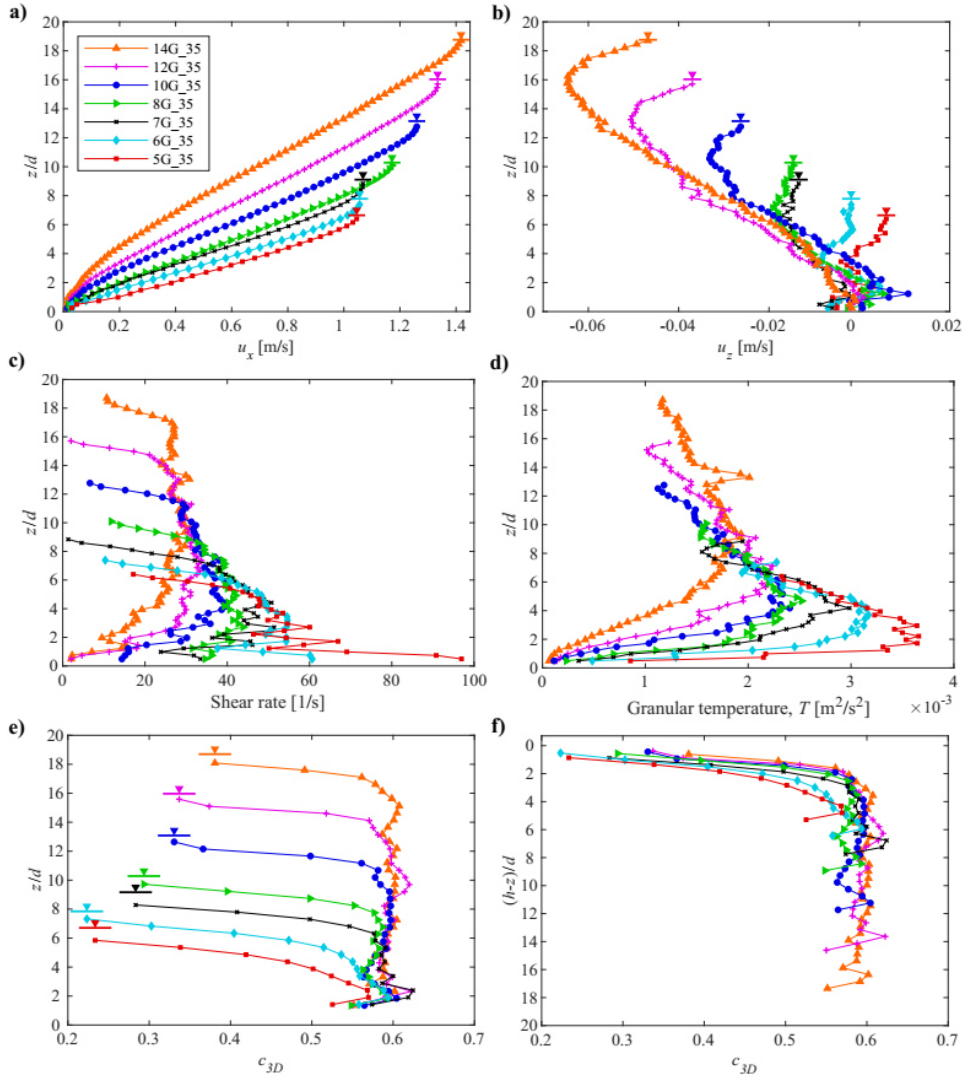

Fig. 4.10 - Sidewall profiles for the G-bed with inclination angle of the chute α = 35°: a) longitudinal velocity profiles; b) vertical velocity profiles; c) shear rate profiles; d) granular temperature profiles; e) volume fraction profiles; f) volume fraction profiles aligned at the free surface.

As already observed in the P40 bed, for $z<z_{in}$, if the flow depth increases,

namely the normal pressures becomes higher, the strong shear and the strong agitation induced by the G-bed are progressively inhibited (Fig. 4.10c, d). For the experiments with a flow depth smaller than the distance of influence of the rough bed, namely 5G_35 to 7G_35, the grain collisionality is high: volume fraction is less than 0.6 all along the flow depth and the longitudinal velocity profile is concave ($\partial_{zz} u_x \leq 0$), as shown by the decreasing trend of the shear rate with z. If $h>z_{in}$, namely for the 8G_35 to 14G_35 experiments, the dense core layer takes place (Fig. 4.10e). It develops soon above the basal surface up to $3d \div 4d$ from the free surface. Frictional dissipation mechanisms takes place in the core layer and are more relevant in its lower part due to higher normal pressures and the higher sidewall resistances. This induce a change in concavity of the velocity profiles, clearly visible in the lower zone of the experiments with the highest h (14G_35). The linearization of the velocity profile in the core layer is more evident for $z > z_{in}$, where the strong agitation effect of the basal roughness progressively disappears and the sidewall resistances, together with the normal pressures, are the main cause of modification of the velocity profile shapes.

In the upper collisional layer, volume fraction rapidly decreases with z and the grains tend to go toward the core layer, as already observed in the other experimental campaigns. When the flow depth is small, u_z is very close to zero or even positive. As already observed for the P40 experiments, the rough basal surface induces high value of T and thus a more collisional behavior of the granular material. This could cause an expansion of the granular body (5G_35) and thus values of the volume fraction lower than the loose random packing.

4.1.4 Free surface measurements

The free surface velocity profiles related to all the KBCs analyzed in the experiments performed in the 8cm-wide channel tilted with α = 35° are presented in Fig. 4.11. The longitudinal velocity, u_x, is normalized with the respect to maximum value at the free surface, $u_{x,max}$, in order to compare the shape of the profiles (Fig. 4.11a, c, e). The *y*-component of the free surface velocity, u_y, was kept in a dimensional form to give information about its magnitude (Fig. 4.11b, d, f).

As one can see, all the $u_x/u_{x,max}$ profiles show a symmetric parabolic shape with the maximum value of the velocity at $y=W/2$ and the minima at $y=0$ and $y=W$ due to the sidewall friction. Differently, the u_y profiles exhibit an anti-symmetric shape with an approximately null value at $y=W/2$ and almost null value of the velocity at the sidewalls.

In case of slip KBC at the basal surface, the $u_x/u_{x,max}$ profiles collapse into a unique profile (Fig. 4.11a). In case of sandpaper and granular bed, the $u_x/u_{x,max}$ profiles do not collapse but become blunter and blunter as the mass flow rate increases (Fig. 4.11c, e). When the mass flow rate is high enough, the grains tend to go toward the sidewalls and the u_y profiles show an anti-symmetric shape (Fig. 4.11b, d and f). $|u_y|$ exhibits two peaks ($|u_y| = 0.02$ m/s) at a distance of $y/W=0.2$ from both the sidewalls. It is interesting to look both at the u_y profiles at the free surface and the u_z profiles at the sidewall presented in the previous sections (Fig. 4.8b, 4.9b and 4.10b). In

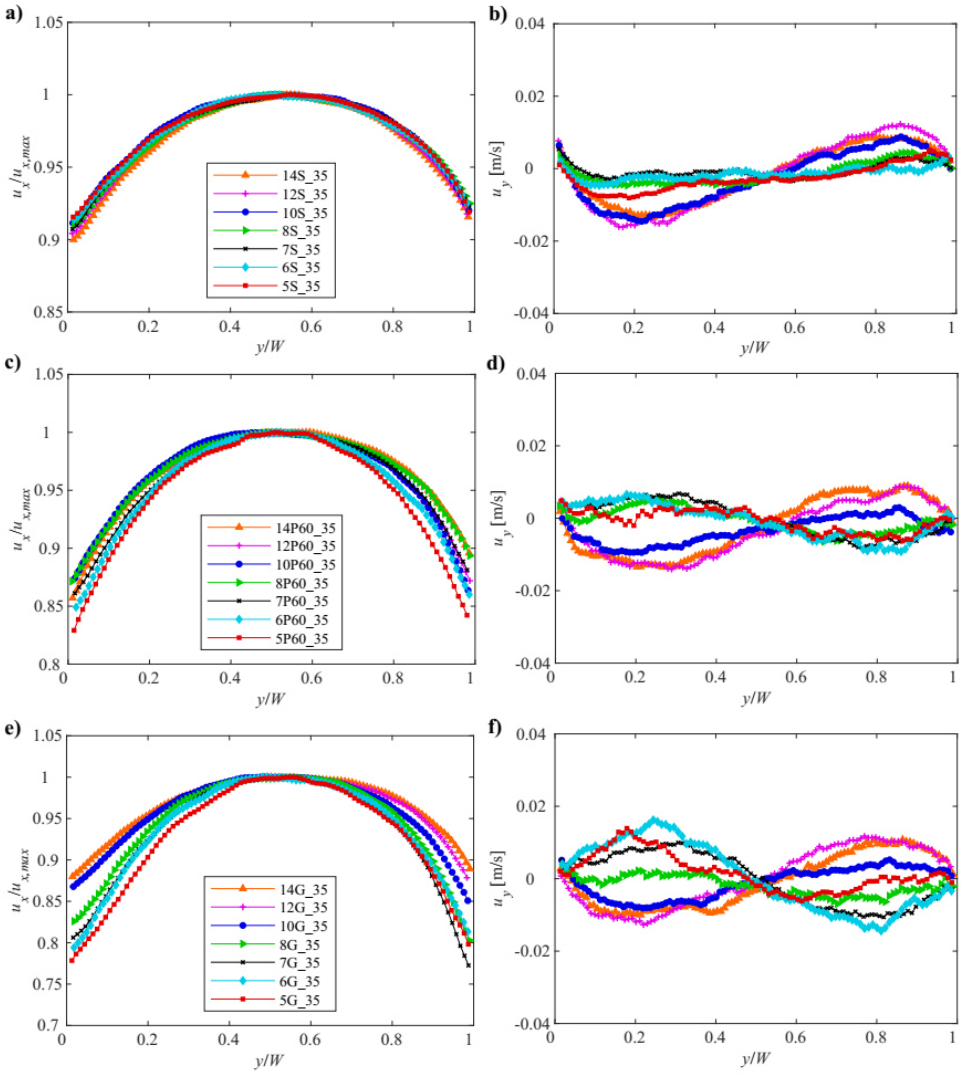

Fig. 4.11 - Free surface velocity profiles related to the experiments with α = 35°: Bakelite bed (a,b), sandpaper bed (c,d) and granular bed (e,f).

case of high flow depths, vertical velocities were found to be negative so the grains move toward the basal surface. At the free surface, the grains tend to

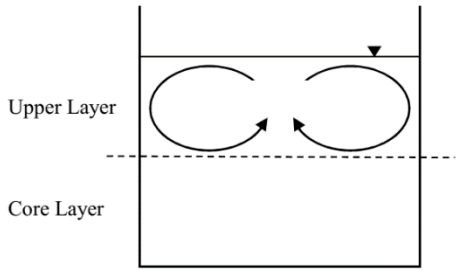

Fig. 4.12 - Secondary circulation scheme.

go toward the sidewalls. In order to balance the mass along *y* and *z* directions, a secondary circulation should take place in the upper layer (Fig. 4.12). The occurrence of such circulation is possible thanks to the low values of the volume fraction in the upper layer. The secondary circulation could be justified by the high velocities at the free surface, especially in the middle of the cross section, which could induce momentum fluxes toward the sidewalls. In the 5G_35 and 6G_35 experiments, the grains seems to go from the sidewalls to the middle of the channel exhibiting an opposite direction with respect to the experiment with high free surface velocities (Fig. 4.11f). This could let think to the occurrence of a secondary circulation in the other direction. However, vertical velocity is almost null or slightly positive. Furthermore, it is worth underling that this phenomenon can be clearly observed only in two cases, so it would be too much ambitious stating the existence of an opposite circulation. In any case, the non-null values of the transversal velocity reveals that momentum is exchanged also along the *y*-direction so the motion of a dry granular material down an incline must be considered weakly three-dimensional.

4.2 Experiments over fixed basal surface: inclination angle of the chute $\alpha = 30°$

The experiments presented in this section were performed in the same 8cm-wide channel used in the experimental campaigns with $\alpha = 35°$ (Sect. 4.1). However, the inclination angle of the chute is lower and equal to 30°. In this investigation, we used part of the fixed basal surfaces employed in the experiments performed with $\alpha = 35°$: the Bakelite bed (S), the P40 bed (P40) and the fixed granular bed (G).

The lower inclination angle of the chute involved lower driving forces, higher vertical normal pressures and higher resistance forces so the KBC observed at the bed were partially different. The experimental campaign on the smooth Bakelite surface, S_30, allows studying a slip kinematic boundary condition at the bed, as in the S_35 experiments. Differently from the P40_35 experimental campaign, for which rolling and saltation of the grains was observed at the basal surface, in the experiments performed over the P40 basal surface with $\alpha = 30°$, P40_30, a no-slip KBC with weak grain rolling was observed. In the experimental campaign performed over the fixed granular bed, G_30, a no-slip KBC without grain rolling was studied.

Part of these investigations were antecedent to the development of the volume fraction measurement technique (SOM method) for chute applications. Therefore, volume fraction measurements were not available for all the experimental campaigns but only for the experiments performed over the Bakelite surface (S_30), to which the SOM method was applied for

the first time.

Results of the S_30 experimental campaign were submitted to Advanced Powder Technology Journal (Carleo et al. 2018, in the references). Results of the velocity measurements of all the experimental campaigns performed with inclination angle of the chute $\alpha = 30°$ were instead already published in Rock Mechanics and Rock Engineering Journal (Sarno et al. 2018a, in the references). The list of all the experiments is presented in Tab. 4.3.

Tab. 4.3- List of all the experiments performed in the 8cm-wise channel tilted with inclination angle of $\alpha = 30°$.

Experimental campaign ID	**Exp. ID**	**Gate opening [m]**	**Basal surface**	Q_m **[g/s]**	h **[m]**	β **[°]**
S_30	5S_30	0.05	Bakelite (S), l <<10μm	926	0.013	-0.30
	6S_30	0.06		1181	0.018	-0.73
	7S_30	0.07		1402	0.020	-0.80
	8S_30	0.08		1622	0.024	-1.39
	10S_30	0.10		1994	0.032	-1.61
	12S_30	0.12		2466	0.040	-2.02
	14S_30	0.14		2845	0.047	-1.97
P40_30	5P40_30	0.05	Sandpaper (P40), l = 425 μm	643	0.022	0.44
	6P40_30	0.06		755	0.037	-0.08
	7P40_30	0.07		837	0.044	-0.47
	8P40_30	0.08		928	0.051	-0.49
	10P40_30	0.10		1041	0.061	-0.78
	12P40_30	0.12		1208	0.070	-1.44
	14P40_30	0.14		1488	0.079	-1.66
G_30	5G_30	0.05	Grain (G), l = 1.65 μm	309	0.040	-0.24
	6G_30	0.06		387	0.046	-0.02
	7G_30	0.07		465	0.051	-0.72
	8G_30	0.08		577	0.059	-0.66
	10G_30	0.10		784	0.069	-0.89
	12G_30	0.12		1016	0.080	-1.04
	14G_30	0.14		1257	0.089	-0.94

4.2.1 Sidewall measurements: experiments over smooth bed (S_30)

A slip condition with negligible grain rolling at the bed was observed by employing the Bakelite basal surface. The sidewall profiles are presented in Fig. 4.13. As one can see, by comparing the profile shapes with those of the S_35 runs, a very similar rheological stratification can be observed. In the lower zone, high values of the shear rate and low values of the volume fraction confirm the occurrence of a shear band (Fig. 4.13c, e). Because of the sidewall friction, the slip velocity exhibits a decreasing trend with the flow depth, as already observed in the S_35 experiments. Moreover, with a fixed h, slip velocities are lower, due to lower driving forces. T and $\dot{\gamma}$ are, instead, higher with respect to the S_35 experiments.

In the middle region, a dense frictional-collisional regime occurs. The core region forms when the normal pressure increases, namely when the flow depth increases, and it develops from $z \approx 1d$ to about $3d \div 4d$ from the free surface (10S_30 to 14S_30 experiments). In the core layer, volume fraction keeps approximately constant with z and it exhibits a value of ≈0.6. The onset of the frictional forces in the granular body, due to both the increase of the normal pressures and the sidewall resistances, induces a linearization of the velocity profiles with $\dot{\gamma} \approx 20$ 1/s. This value is slightly higher than the

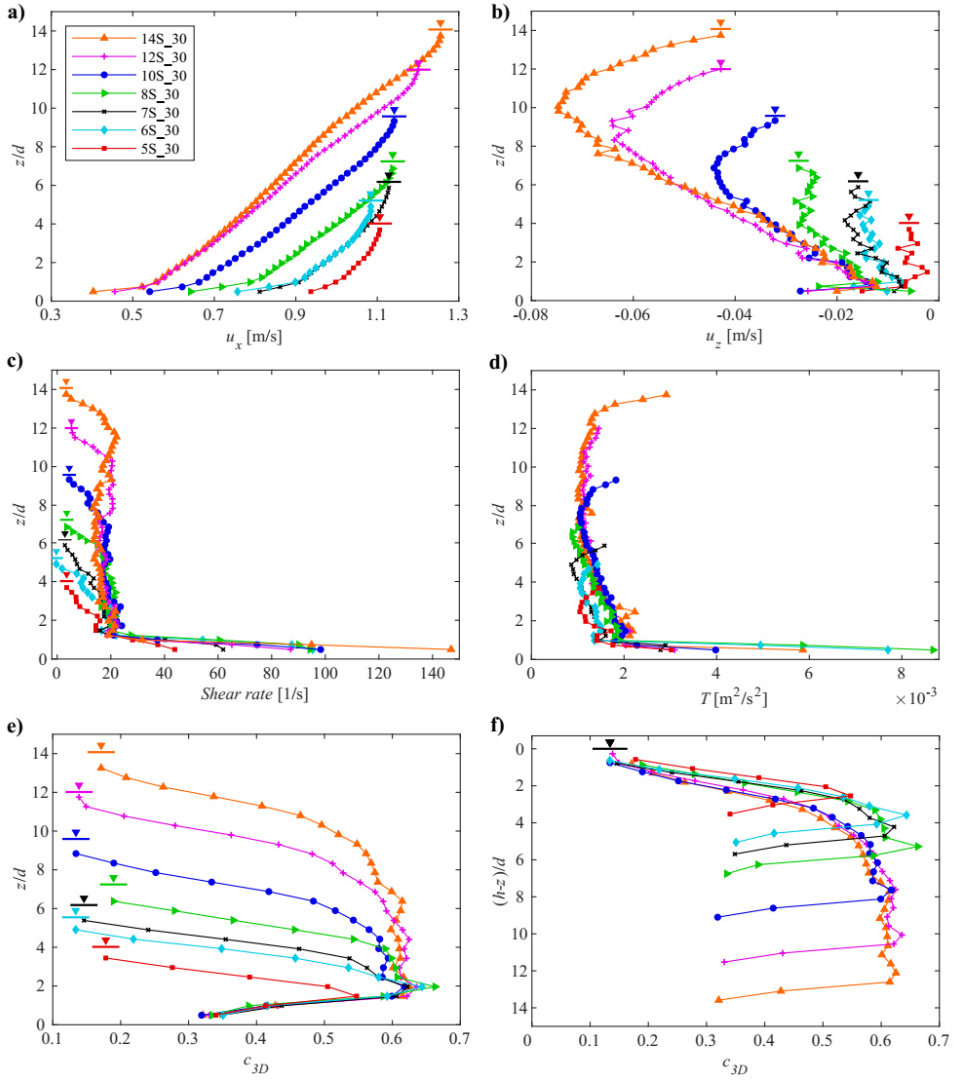

Fig. 4.13 - Sidewall profiles for the S-bed with inclination angle of the chute α = 30°: a) longitudinal velocity profiles; b) vertical velocity profiles; c) shear rate profiles; d) granular temperature profiles; e) volume fraction profiles; f) volume fraction profiles aligned at the free surface.

value found for the S_35 experiments ($\dot{\gamma} = 10 \div 15$ 1/s). Granular

temperature is constant with z and it assumes values of $\approx 1 \div 2 m^2/s^2$, slightly higher than T in the S_35 experiments (values less than ≈ 1 m^2/s^2). This is probably because lower slip velocities induce a less ordered granular flow and thus a less blunt sidewall velocity profile. If the flow depth is small so that the core region do not form (5S_30 to 8S_30), the velocity profiles exhibit a concave shape all along the flow depth, as shown by the decreasing values of the shear rate with z (Fig. 4.13c).

The upper collisional layer, with an approximately constant thickness of $\approx 3d \div 4d$, forms soon above the core region. It is characterized by the decreasing trend of the volume fraction with z and a concave shape of the velocity profiles. The volume fraction decreases more rapidly for the 5S_30 to 8S_30 experiments, for which the core layer do not form (Fig. 4.13f). Granular temperature slightly increases in the upper layer due to more collisions among the grains. The z-component of the sidewall velocity shows only negative values with maximum in correspondence of the interface between the dense middle region and the dilute upper region (Fig. 4.13b), as already observed in the previous experimental campaigns (Sect. 4.2). The characteristics of the upper layer of the S_30 experiments are very similar to the S_35 experiments and of the other experimental campaigns leading to the occurrence of a secondary circulation.

4.2.2 Sidewall measurements: experiments on the P40 bed (P40_30)

By employing the P40 basal surface but by lowering the inclination angle of the chute from 35° to 30°, a different KBC arises at the bed. Grain saltation is completely inhibited and only weak grain rolling was observed. This is because normal pressures at the basal surface are higher because of a lower inclination angle.

The u_x-profiles, the u_z-profiles, the shear rate profiles and the granular temperature profiles are shown in Fig. 4.14. The experiments can be grouped in three families: the first family only contains the 5P40_30, which is the experiment with the smallest flow depth, h; 6P40_30, 7P40_30 and 8P40_30 are in the second family; the third family contains the experiments with the higher flow depth, namely 10P40_30, 12P40_30 and 14P40_30.

Since no volume fraction measurements are available for the P40_30 experimental campaign, only some hypotheses can be done on the flow regimes on the basis of the analyses carried out on the S_30 experimental campaign (Sect. 4.2.1) and all the experiments performed with $\alpha = 35°$ (Sect. 4.1), for which volume fraction measurements were taken.

The 5P40_35 experiment is the only experiment that shows a linear longitudinal velocity trend with z (Fig. 4.14a). In fact, the shear rate is approximately constant along the flow depth and slightly higher than 20 1/s (Fig. 4.14c). The agitation induced by the basal roughness is higher with respect to the other groups of experiments due to the small flow depth ($h \approx 6d$), namely low normal pressure values (Fig. 4.14d). The u_z profile

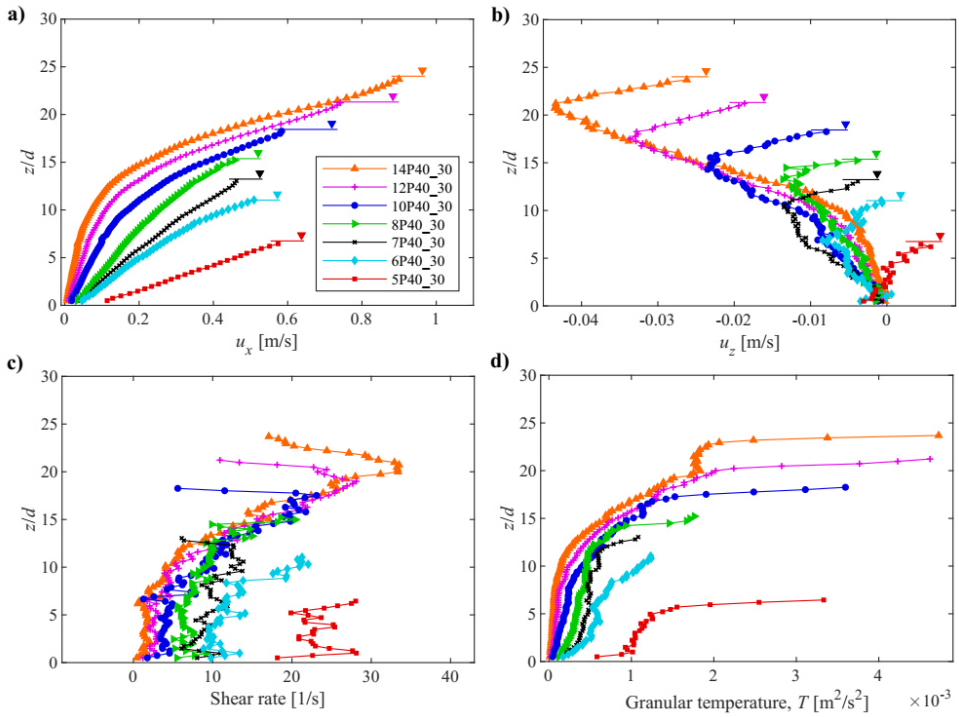

Fig. 4.14 - Sidewall profiles for the P40-bed with inclination angle of the chute α = 30°: a) longitudinal velocity profiles; b) vertical velocity profiles; c) shear rate profiles; d) granular temperature profiles.

shows positive values for most of the flow depth indicating that grains are moving away from the bed (Fig. 4.14b). These characteristics are found to be typical of a dilute regime so one could expect volume fraction values less than the loose random packing of the granular material, namely ≈0.6.

In the second family of the experiments, longitudinal velocity exhibits almost null values at the bed. Due to higher flow depth, grain rolling progressively disappears. The onset of frictional dissipation forces due to both higher sidewall resistances and higher normal pressures induce a weak

convexity of the u_x velocity profiles ($\partial_{zz} u_x \geq 0$), as already observed for the G_35 experiments with the high flow depth (Sect. 4.1.3). Moreover, the *T*-values are almost null at the bed and slightly increase with *z*. For these experiments, a denser frictional collisional regime takes place so one could suppose that the volume fraction values, averaged along the flow depth, could be closer to the saturation value, namely 0.6, with respect to the 5P40_30 experiment.

In the third category of experiments, the frictional forces are quite high: the longitudinal velocity profiles exhibit a clear convexity with smaller and smaller values of u_x at a fixed *z*. The same trend can be observed in the *z*-component of the sidewall velocity, u_z. As one can see in Fig. 4.14b, in the 14P40_30, which is the experiment with the highest flow depth, u_z shows an almost null value at the bed and increases with *z* very slower than the other experiments. This is because a different flow regime establishes: frictional dissipation mechanisms strongly prevail on the collisional stresses due to high normal pressures, high sidewall resistances and, probably, high values of the volume fraction close to 0.6.

4.2.3 Sidewall measurements: experiments over granular bed (G_30)

In the experiments over the G-bed, rigorous no-slip and no-rolling occur at the basal surface. The u_x profiles, the u_z profiles, the shear rate profiles and the granular temperature profiles are shown in Fig. 4.15. The longitudinal velocity profiles are very similar to the ones observed in other experimental

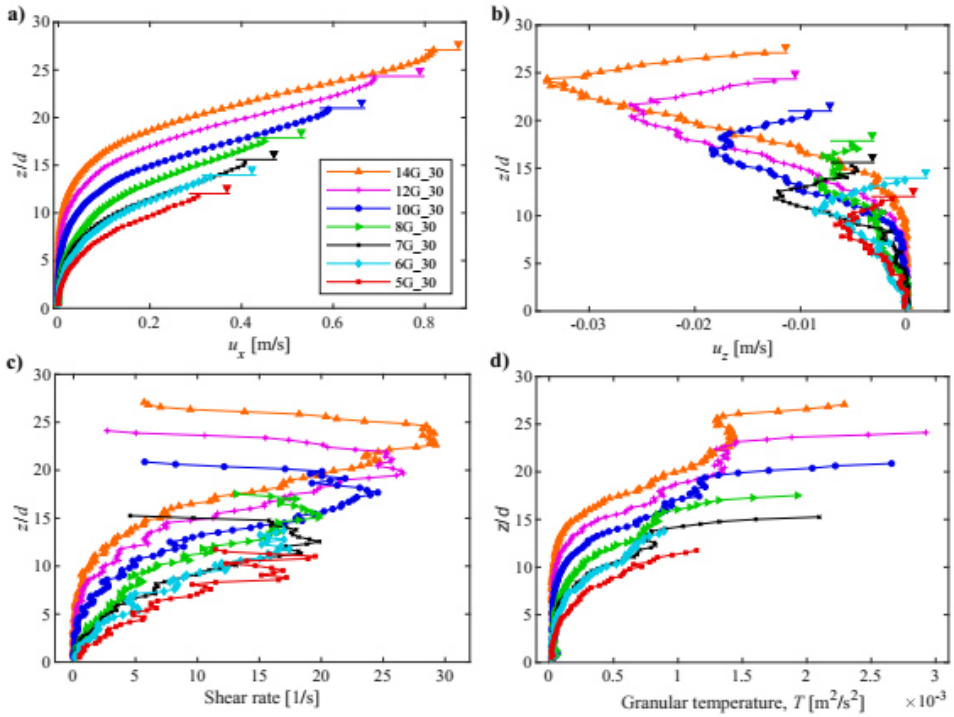

Fig. 4.15 - Sidewall profiles for the G-bed with inclination angle of the chute α = 30°: a) longitudinal velocity profiles; b) vertical velocity profiles; c) shear rate profiles; d) granular temperature profiles.

works in heap flow and rotating drum geometries (Komatsu et al. 2001; Bonamy et al. 2002; Jop et al. 2005). One may distinguish two layers (Fig. 4.15a): an upper approximately linear layer, called *surface flow* layer, and a lower convex layer, called *creep flow* layer. For the experiments with high values of the flow depth, a weak concavity of the velocity profiles beneath the free surface can be observed, as confirmed by the decreasing trend of the shear rate with z (Fig. 4.15c). This is due to high values of the longitudinal velocities at the free surface that induce a more collisional behavior of the

granular flows so the velocity trend is more similar to a Bagnold scaling (Bagnold 1954). In case of small flow depth, this concavity is not so evident because the velocities at the free surface are very small so the collisions are rarer.

The joint information of T and u_x supports the occurrence of a rheological stratification (Armanini et al. 2008; Doyle et al. 2010; Sarno et al. 2014). The granular temperature (Fig. 4.15d) exhibits almost null values in correspondence of the creep flow. Frictional dissipation mechanisms prevail inducing a strong convexity of the velocity profiles. It is worth recalling that the convexity of the lower part of the velocity profiles due to the friction was visible also in the P40_30 (Sect. 4.2.2) but only when flow depth was high enough, due to the smaller basal roughness (see the appendix of Sarno et al. 2018a). In the upper surface flow, more collisional dissipation mechanisms take place: higher values of T can be observed and longitudinal velocity exhibits a linear trend.

Similar to other experiments, the u_z velocities are negative all along the flow depth. Moreover, the profiles show a minimum at around $3d \div 5d$ from the free surface in all the runs.

4.2.4 Free surface measurements

The free surface measurement are reported in Fig. 4.16. As already observed in the case of $\alpha = 35°$, the longitudinal velocity profiles at the free surface exhibit a symmetric and approximately parabolic shape, owing to the non-negligible effects of the sidewall resistance. The profiles related to the

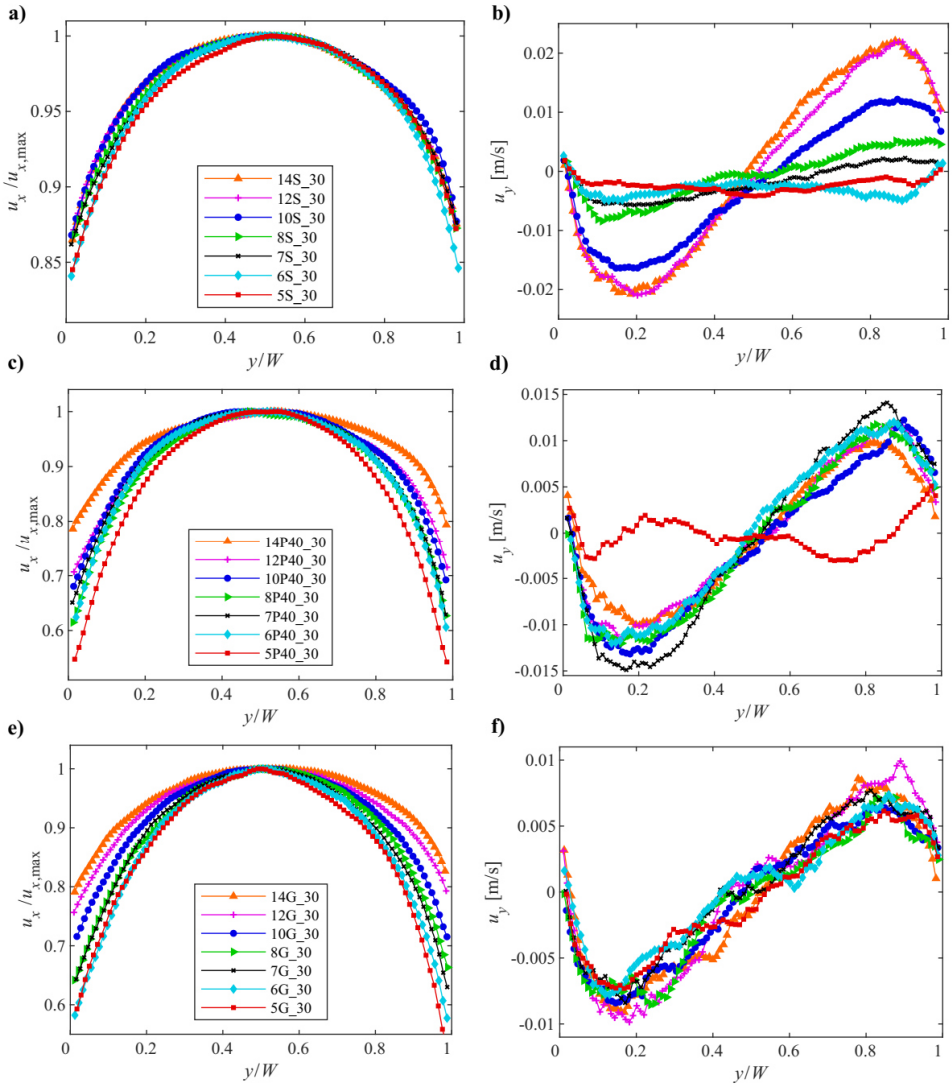

Fig. 4.16 - Free surface velocity profiles related to the experiments with α = 30°: Bakelite bed (a,b), sandpaper bed (c,d) and granular bed (e,f).

experimental campaign under slip condition at the bed, S_30, collapse into a unique profile, as already observed in the S_35 experiments. In case of sandpaper and granular bed, the profiles tend to be blunter and blunter as the

mass flow rate increases. If the mass flow rate is high enough, the transversal velocity profiles exhibit an anti-symmetric shape with null velocity at $y=W/2$. By looking both at the vertical sidewall velocity profiles (Fig. 4.13b, 3.14b and 3.15b) and at the transverse velocity profiles at the free surface (Fig. 4.16b, d and f), a secondary circulation (Fig. 4.12) takes place also in the experiments with $\alpha = 30°$. The only exceptions are the experiments on the S-bed, 5S_30, 6S_30, 7S_30 and 8S_30, and the 5P40_30 for which agitation is low.

5. Results of the laboratory investigation on granular flows over erodible bed

The erodible bed is a configuration that often occurs in nature in which the sediments flow over a loose bed made up of the same sediments. As pointed out by many authors (Komatsu et al. 2001; Taberlet et al. 2003; Jop et al. 2005), under this configuration, fully developed uniform flow conditions can be observed: a *flowing layer* of constant thickness, h_{flow}, develops along the channel atop a stabilized heap of granular material (Fig. 5.1). The dynamics of such flows is strongly influenced by the sidewall effect (Jop et al. 2005). Moreover, as already illustrated in Sect. 2.5.3, the characteristics of these flows depend on the channel width, as well (Taberlet et al. 2003; Jop et al. 2005). The goal of this part of the laboratory activity was to investigate on the effect of both the sidewall friction and the channel width on the dynamics of chute dry granular flows by analysing both velocity and volume fraction measurements taken at boundaries. The experiments were performed in two channels of width 8cm, namely ≈24*d,* (experimental campaign ID, E_8), and 3cm, namely ≈9*d*, (E_3), respectively. The erodible bed configuration was obtained by placing a small weir at the outlet of the channels so a flowing layer of constant thickness can develop above a granular pile.

In order to check the existence of steady uniform flow conditions the inclination of the free surface and of the surface that downwardly delimits

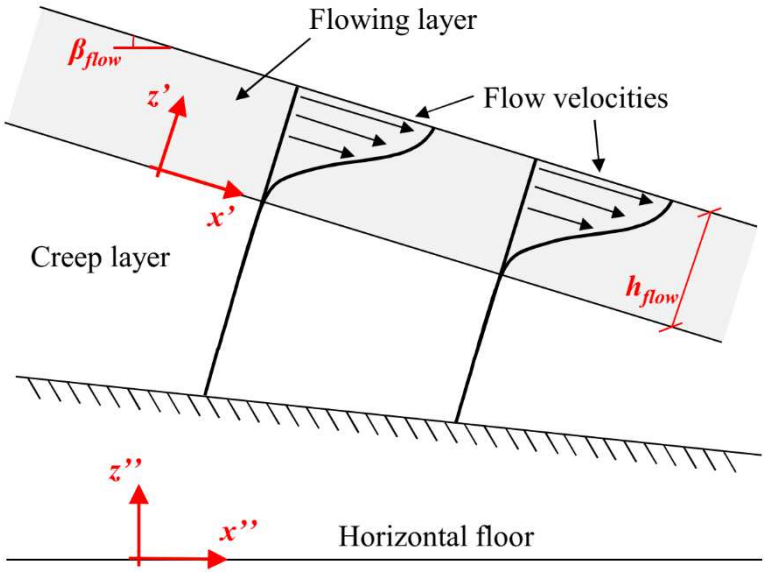

Fig. 5.1 - Sketch of a flowing layer atop a granular pile

the motion field must be equal (Fig. 5.1). The granular pile, over which the granular material flows, is not made up by strictly immobile granular material. In fact, as pointed out by Komatsu et al. (2001), the grains in the granular pile flows very slowly. The sidewall longitudinal velocity is not null but it exhibits an exponentially decreasing trend while going deep in the pile so that this layer is more properly called *creep layer* (Komatsu et al. 2001). For this reason, the concept of interface between the flowing and the immobile granular material is an abstraction. In Literature, a criterion to approximately identify the position of the interface and based on physical quantities is lacking. Jop et al. (2005) carried out experiments in a heap configuration. They employed a blade blackened with a candle immerged in the granular flow. By observing the thickness of the eroded black soot due to friction forces of the grains acting on the blade, they were able to have an

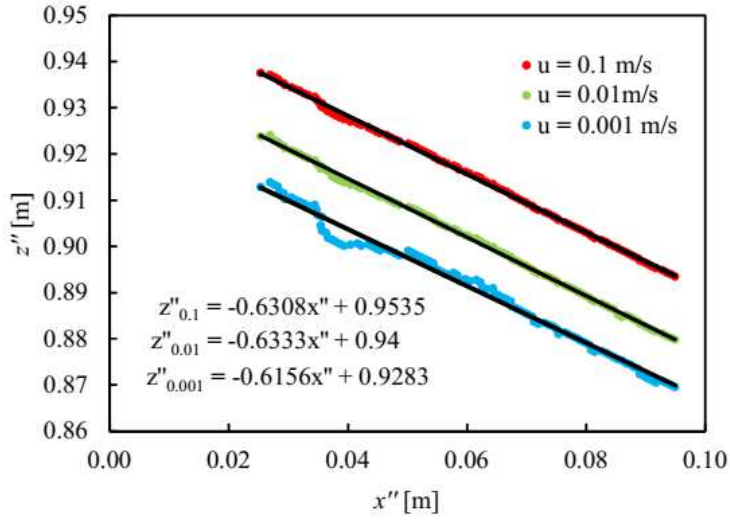

Fig. 5.2 - Location of the point corresponding to the same velocity, measured in different cross section for a repetition of the 18E_8 experiment. Red points correspond to 0.1 m/s, green point to 0.01 m/s and blue point to 0.001 m/s.

idea of the location of such interface. In these investigations, we tried to use a different method. By analysing the sidewall velocity profiles at different cross sections along the channel, one can detect the heights of the points in which the same velocity is measured and verify if they are aligned on a straight line. Moreover, all the lines related to different velocities, should exhibit the same slope in case of uniform flow. By using the reference system (0, x'', z'') of Fig. 5.1, the alignment was reported for a repetition of the 18E_8 run, as an example (Fig. 5.2). Three velocities were tested: 0.1 m/s, 0.01 m/s and 0.001 m/s. As one can see, by using a linear approximation, very similar slope angles of the straight lines, referred to the three analysed velocities, were found. In particular, the angles were found to

be 32.24°, 32.35° and 31.61° related to the velocities of 0.1m/s, 0.01 m/s and 0.001 m/s, respectively. The small discrepancies among these values are mainly due to the same time interval used for obtaining the time-averaged velocity profiles. If one analyse small velocities, one have to use a higher time interval to obtain less oscillations in the determination of the heights of the points. This explains why the values of the inclination angles of the straight lines corresponding to the points related to the velocities of 0.1 and 0.01 m/s are quite similar each other but vary with respect to the points corresponding to the velocity of 0.001 m/s.

The configuration used in the experimental campaigns performed during my PhD is very similar to the one used by Jop et al. (2005) which employed a channel of the same length of those employed in this research. Moreover, by considering that the cross section under study is far enough from both the outlet (50cm) and the inlet (100cm) of the channel, one can reasonable say that steady uniform conditions took place in our experimental set-up.

The list of all the experiments carried out in both channels is presented in Tab. 5.1. The inclination of the interface with respect to the horizontal, β_{flow}, was estimated by using the velocity measurement immediately beneath the free surface, namely employing the formula $\beta_{flow} = \arctan(u_{z''}/u_{x''})$. It is worth underlining that β_{flow} goes with the mass flow rate, namely with h_{flow}, as found by Taberlet et al. (2003) and Jop et al. (2005).

Tab. 5.1 - List of all the experiments performed over erodible bed in two channels of width W = 8cm and W = 3cm.

Experimental campaign ID	Exp. ID	Gate opening [m]	Channel width [m]	Q_m [g/s]	h_{flow} [m]	β_{flow} [°]
E_8	6E_8	0.06	0.08	304	0.040	-31.72
	8E_8	0.08		584	0.047	-31.83
	10E_8	0.10		815	0.052	-31.93
	12E_8	0.12		1102	0.057	-31.96
	14E_8	0.14		1361	0.062	-32.07
	16E_8	0.16		1645	0.065	-32.59
	18E_8	0.18		1912	0.068	-32.86
E_3	16E_3	0.16	0.03	367	0.050	-35.35
	18E_3	0.18		414	0.049	-35.68
	20E_3	0.20		465	0.053	-36.11
	22E_3	0.22		517	0.053	-36.53
	24E_3	0.24		578	0.056	-36.78
	26E_3	0.26		631	0.058	-37.41
	28E_3	0.28		672	0.061	-37.57
	30E_3	0.30		721	0.063	-37.67
	32E_3	0.32		766	0.063	-38.26
	34E_3	0.34		794	0.063	-38.79

5.1 Sidewall measurements: experiments in the channel with a width W = 8cm (E_8)

As shown in Tab. 5.1, the higher is the flow depth h_{flow}, namely the mass flow rate, the higher is the inclination angle of the free interface, β_{flow}. In order to properly compare the sidewall profiles related to different experiments, we decide to present them by considering a reference system

(0, x', z'), where x' and z' are the axes parallel and perpendicular to the free surface, respectively (Fig. 5.1). Since β_{flow} is different for each experiment, the orientation of the reference system changes in each experiment. Moreover, the origin of the reference system changes and it was chosen in correspondence of the interface between the flowing layer and the creep layer identified at the depth where $u_{x'} = 0.001$ m/s. Therefore, all the profiles are aligned at their respective interfaces. The sidewall profiles related to the E_8 experiments are presented in Fig. 5.3. The shape of the velocity profiles is similar to the ones found in other experimental works (Komatsu et al. 2001; Bonamy et al. 2002; Jop et al. 2005) so it could be decomposed in a lower exponential tail and upper linear part. It worth mentioning that the longitudinal velocity trend is also qualitatively similar to the velocity profiles observed in case of solid-liquid mixtures flowing over loose bed (Armanini et al. 2005; Armanini et al. 2008; Lanzoni et al. 2017).

An impressive collapse of the $u_{x'}$ profiles can be observed, with the only exception of the upper collisional layer (Fig. 5.3a). It is worth underlining that the collapse occurs independently on the velocity chosen for the alignment of the profiles. A core region develops soon above the erodible bed and up to $\approx 4d \div 5d$ from the free surface. Volume fraction is approximately constant with z' and it exhibits the typical saturation value of ≈0.6 (Fig. 5.3e) in all the experiments. The separation between the linear and the exponential velocity trend can be roughly identified at $z' \approx 8d$. For $z' < 8d$, the granular temperature is almost null (Fig. 5.3d) while $u_{x'}$ profiles show a convex shape. This means that frictional forces strongly prevail in this zone of the core region. For $z' > 8d$, granular temperature increases with z' so the

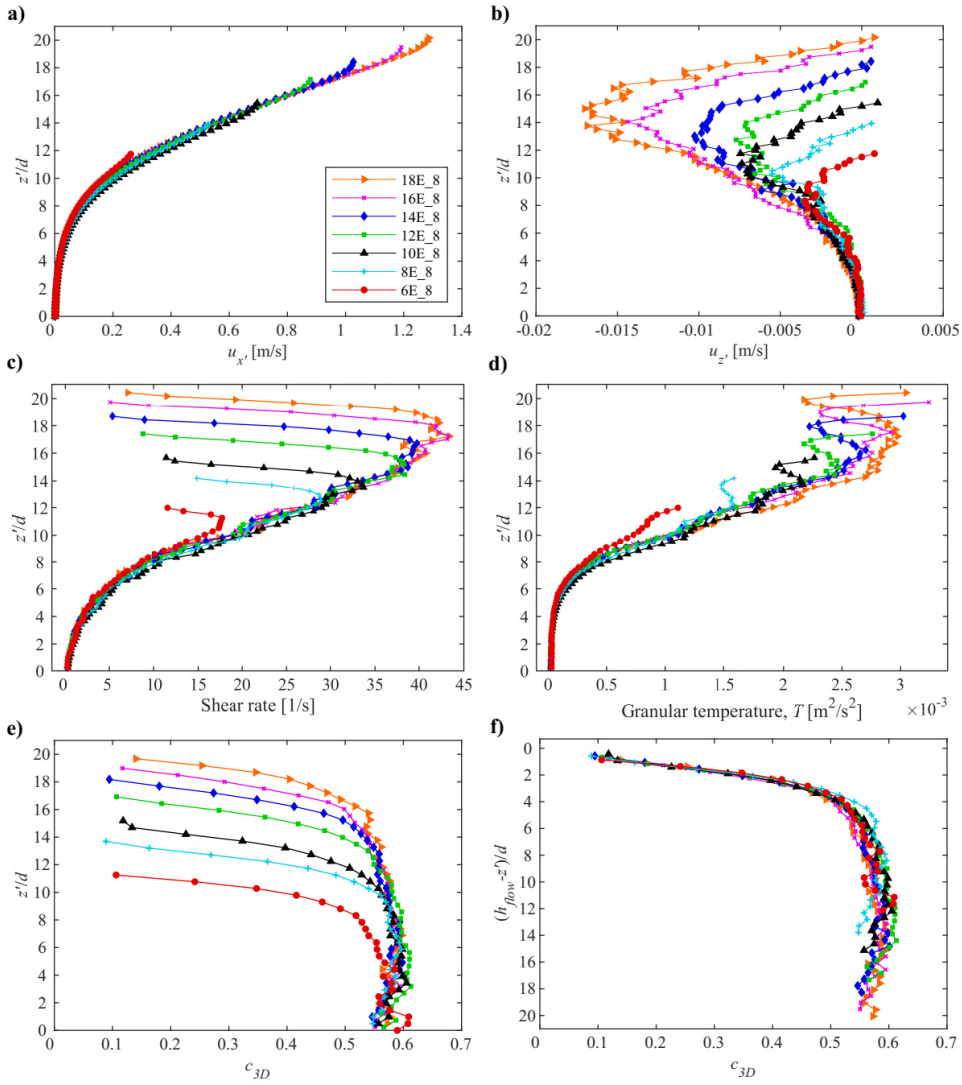

Fig. 5.3 - Sidewall profiles related to the erodible bed performed in 8cm-wise channel: a) $u_{x'}$ profiles; b) $u_{z'}$ profiles; c) shear rate profiles; d) granular temperature profiles; e) volume fraction profiles; f) volume fraction profiles aligned at the free surface.

motion became more collisional and $u_{x'}$ exhibit an increasing linear trend.

Results of the laboratory investigation on granular flows over erodible bed

Differently from the fixed bed, the increasing of the normal stresses due to higher flow depths does not induce any change in the velocity and granular temperature values. The existence of a master curve for the velocity and granular temperature profiles indicates that the effect of the normal pressures within a chute granular flow over an erodible bed are counterbalanced by sidewall friction forces and by all the other dissipative forces. The granular flow find its own equilibrium by only changing the inclination of the flowing layer.

In the upper layer, $u_{x'}$ shows a concave shape typical of the collisional regime, as shown by the decreasing trend of the shear rate with z' (Fig. 5.3c). The collisional behavior of the granular material within this layer can be also observed by the rapid decrease of the volume fraction with z'. The z'-component of the velocity is negative with a minimum located slightly lower with respect to the experiments on the fixed bed, namely at $4d \div 5d$ from the free surface (Fig. 5.3b). It is impressive the collapse of the volume fraction profiles of all the runs if one aligns them at their respective free surfaces (Fig. 5.3f).

5.2 Sidewall measurements: experiments in the channel with a width W = 3cm (E_3)

In the E_3 experimental campaign, the gate openings were chosen to obtain the same thickness of the flowing layer of the E_8 experiments so one can do appropriate comparisons (see Sect. 6). A preliminary investigation was performed to detect the adequate range of gate openings and it was found to

be [16cm, 34cm]. As in the E_8 experiments, in order to align all the profiles at their respective interfaces creep layer – flowing layer, we decided to employ a reference system (0, x', z') based on the schematization of Fig. 5.1. The alignment of the profiles at the interface, identified at the depth where $u_{x'}$ = 0.001 m/s, did not give the expected collapse of the sidewall profiles. This is probably due to PIV errors in the detection of such small velocity. The analysis of the shape of the "raw profiles", which are qualitatively the same of the E_8 experimental campaign, showed that the shear rate of the linear part is approximately the same in all the runs. Therefore, we decided to align the profiles at the beginning of the linear part, namely at the depth where $u_{x'}$ is equal to 0.7 m/s. Successively, the profiles were cut in the lower part in order to consider only the $u_{x'}$ values more than 0.001 m/s for which PIV measurements can be considered accurate.

The sidewalls profiles are shown in Fig. 5.4. As one can see, the collapse of the velocity profiles occurs also for this experimental campaign. We think that it is not a case and it is not due to an *ad-hoc* alignment criterion. The non-alignment of the velocity profiles at the interface is mainly due to the difficulties in the detection of the interface.

A master curve in the $u_{x'}$ profiles can be observed in the E_3 experimental campaign, as well. Similar considerations to the previous case can be done. A core region develops with high volume fraction (≈0.6) soon above the erodible bed. Frictional forces takes place in the lower part of the core region inducing a convex shape in the velocity profiles. The increasing of the normal pressures do not induce any significant variation in the shape of the velocity and granular temperature profiles, which remains the same even if

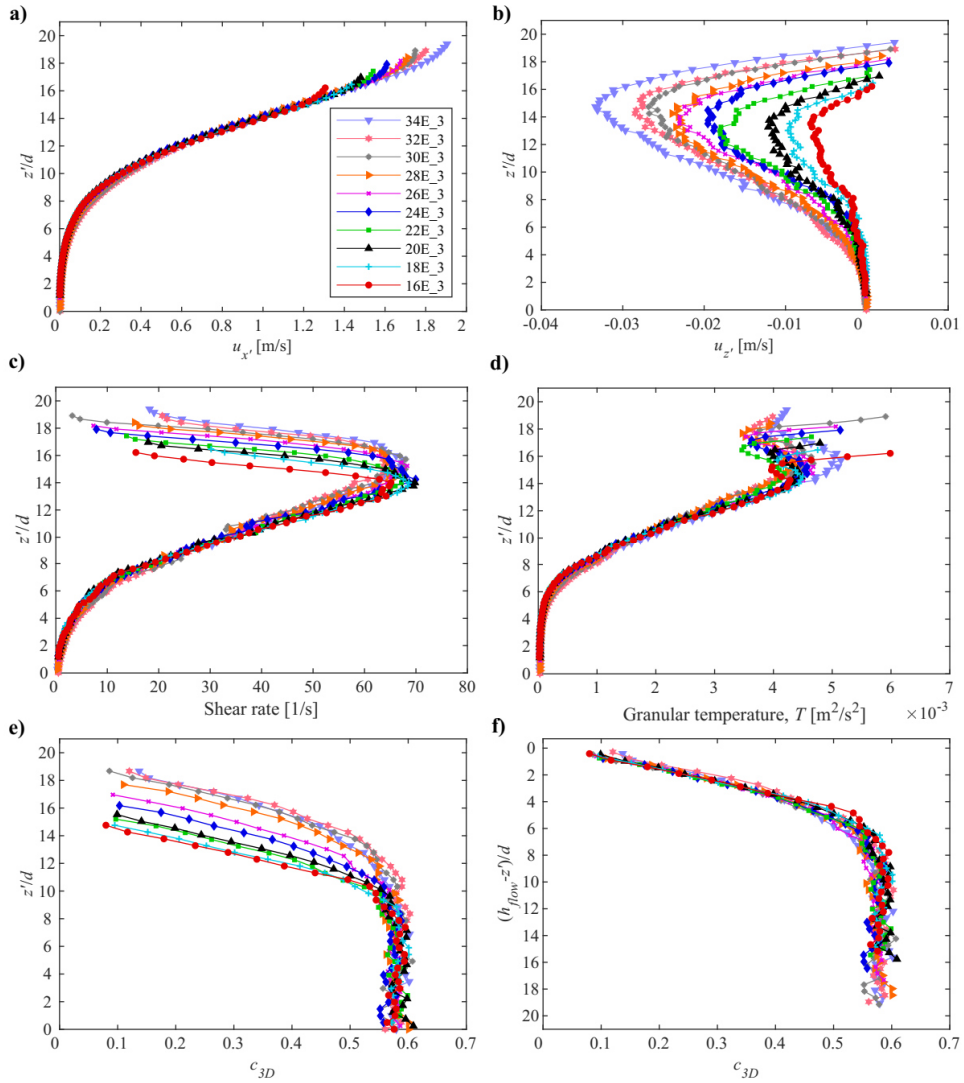

Fig. 5.4 - Sidewall profiles related to the erodible bed performed in 3cm-wise channel: a) $u_{x'}$ profiles; b) $u_{z'}$ profiles; c) shear rate profiles; d) granular temperature profiles; e) volume fraction profiles; f) volume fraction profiles aligned at the free surface.

the flow depth increases.

In the upper collisional zone, grain agitations is high due to the high velocity

at the free surface and low values of the volume fraction. The decreasing trend of the volume fraction with z' is the same in all the experiments. By align the volume fraction profiles at the free surface, one can observe that the thickness of the collisional layer is approximately constant in all the experiments and of $\approx 4d \div 5d$. The grains tend to go toward the granular pile showing higher downward velocities as the mass flow rate increases.

5.3 Free surface measurements

The free surface velocity profiles are presented in Fig. 5.5. The longitudinal velocity profiles exhibit the typical approximately parabolic shape due to the sidewall effect both in the case of W = 8cm and W = 3cm (Fig. 5.5a, c). Moreover, the profiles exhibit a more pronounced concavity when the mass flow rate is small and become blunter and blunter as the free surface velocities increase.

By looking both at the u_z profiles (Fig. 5.3b) and the u_y profiles (Fig. 5.5b) related to the E_8 experimental campaign, a secondary circulation occurs in all the experiments. In the E_3 experiments, u_y are very small and comparable with the PIV accuracy so they could be considered null and the secondary circulation does not take place. The non-occurrence of the secondary circulation is probably due to the higher velocities and the higher grain agitation at the free surface, which are almost twice the respective values measured in the E_8 runs. This induces a more chaotic and turbulent collisional regime so that the occurrence of the weak secondary circulation

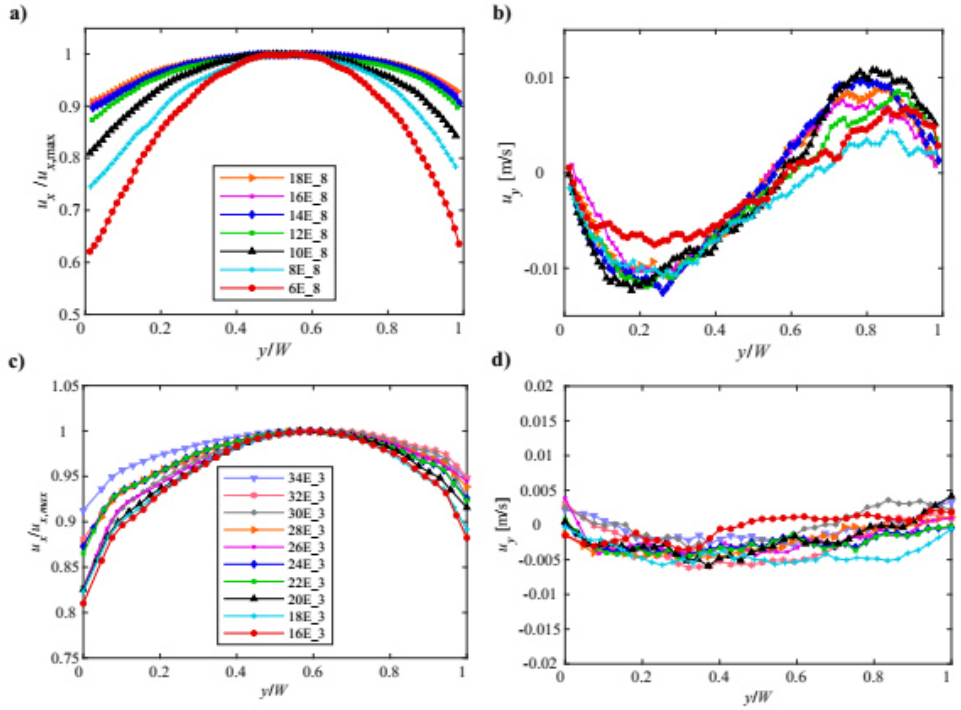

Fig. 5.5 - Free surface velocity profiles related to the experiments on erodible bed: W = 8cm (a,b) and W = 3cm (c,d).

is inhibited.

6. Discussion about the results of the laboratory investigation

In this section, a comparison among all the experiments performed during the laboratory activity will be shown. Before going into details, it is important to recall the definition of the coefficient *f*, defined by Sheng et al. (2011) and presented in Sect. 2.5.3, which gives important information on the effect of the sidewall friction on the velocity field in the transverse direction *y* (Eq. (20)). Since no information of the *y*-component of the velocity can be gather except at the free surface, in our calculation, the coefficient *f* can be evaluated only at the free surface:

$$f(h) = \frac{\frac{1}{W}\int_0^W u(y,h)dy}{u(0,h)} \tag{27}$$

This coefficient will be used to compare the free surface velocity profiles (Sheng et al. 2011; Sarno et al. 2018a).

6.1 Fixed basal surface

The analysis of the volume fraction profiles showed that some similarities occurred among all the experiments. A lower region, near the basal surface, with an approximately constant thickness of ≈1*d*, was identified. Volume fraction is low due do the presence of the fixed bed (G_35 and P40_35

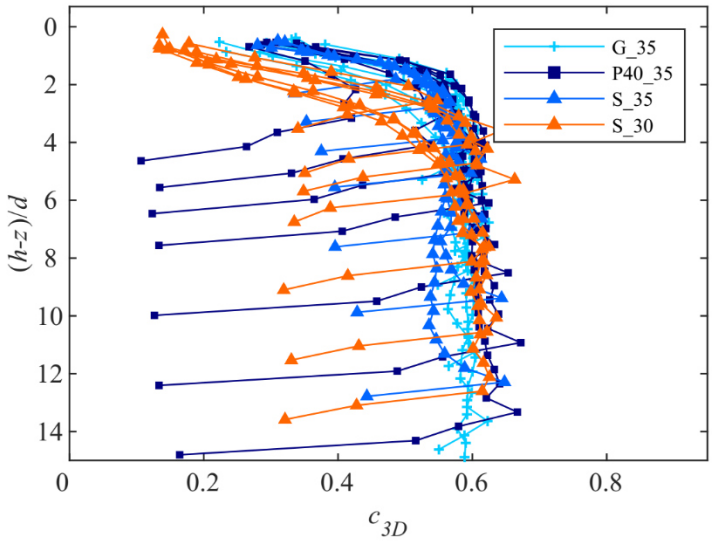

Fig. 6.1 - Volume fraction profiles related to the experiments performed over fixed bed aligned at the free surface.

experimental campaign) or due to the occurrence of the shear band (S_35 and S_30 experimental campaign). A core layer exhibiting a constant value of the volume fraction with z and approximately equal to the loose random packing of the granular material (≈0.6) develops soon above the lower region. A superimposed upper layer, within which volume fraction rapidly decreases with z, was identified in all the experiments.

In Fig. 6.1 all the volume fraction profiles aligned at the free surface are reported. As you can see, the thickness of the upper layer in the experiments performed with α = 35° is of ≈2d÷3d, while for the S_30 experiments is slightly higher and about ≈4d. This difference could be probably due to the difficulties in the detection of the interface between upper and core layer, which is simply based on the detection of the beginning of the decreasing

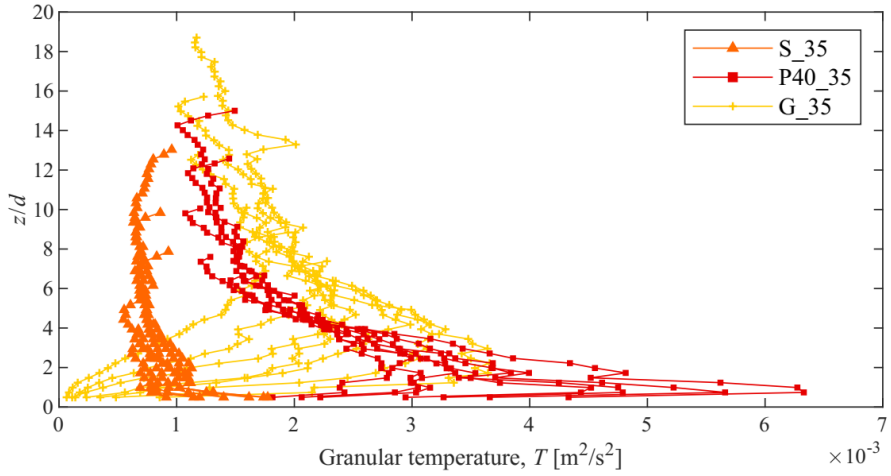

Fig. 6.2 – Granular temperature profiles related to the experiments performed with $\alpha = 35°$.

trend of c_{3D} with z.

In Fig. 6.2, all the granular temperature profiles related to the experiments performed with $\alpha = 35°$ are shown. The values of T are strongly influenced by the kinematic boundary condition observed at the bed. As you can see, in the proximity of the fixed basal surface, the highest value of T were measured in the P40_35 experiments, where rolling and strong saltation of the grain was observed. In the G_35 experimental campaign, in the nearest of the basal surface, T is globally lower than P40_35 experiments due to the strong interlocking of the grains in the voids of the fixed granular bed (Sect. 4.1.3). A lower agitation can be observed in the S_35 experiments, where the slip KBC induced smaller fluctuation velocities.

In Fig. 6.3, granular temperature is plotted for all the experimental campaigns performed with $\alpha = 30°$. As on can see, T values are globally

lower with respect to the case of α = 35°. Only in the case of the S_30 experiments, T exhibits slightly higher value ($\approx 1 \cdot 10^{-3}$ m^2/s^2) with respect to S_35 experiments ($<1 \cdot 10^{-3}$ m^2/s^2). This probably due to the fact that higher slip velocities produce a less agitated granular flow. By increasing the basal roughness, the KBC at the bed turns from slip (S_30) to weak grain rolling (P40_30) to rigorously no-slip and no grain rolling (G_30). The agitation reduces and tends to 0 due to the high normal pressures and high value of the basal roughness.

In order to compare the effect of both different KBCs at the bed and the inclination angle of the chute, the sidewall velocity profiles related to some experiments with the same flow depth but performed over different basal roughness, are plotted in Fig. 6.4 as an example. As one can see, a slip condition induces a blunter profile shape with a shear band located soon above the fixed smooth bed. By moving from the 14S_30 to the 14S_35,

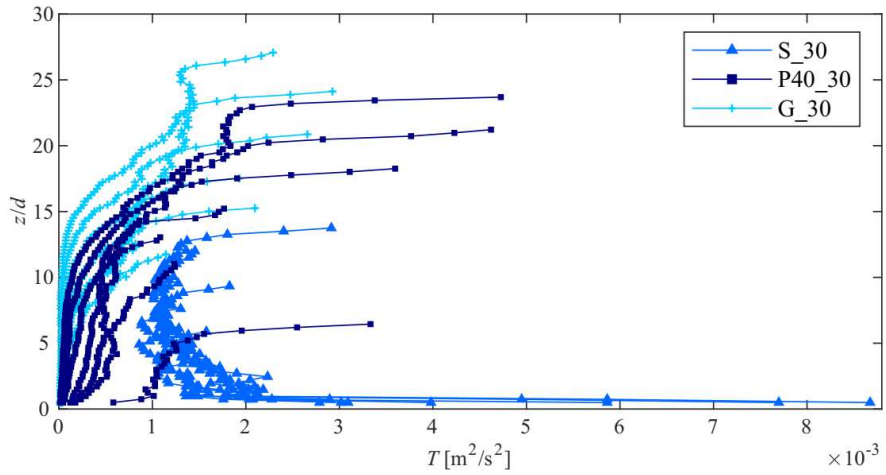

Fig. 6.3 - Granular temperature profiles related to the experiments performed with α = 30°.

namely by increasing the inclination angle of the chute, the profile is blunter due to the higher slip velocities so the granular flow behave more like a plug. In case of the P40 bed, the shape of the velocity profile strongly depends on the KBC at the basal surface. In fact, saltation and grain rolling (12P40_35) induce strong deformations so the velocity profile shape is concave all along the flow depth ($\partial_{zz} u_x \leq 0$), as typically observed is the collisional regime. In case of only weak grain rolling (7P40_30), the profile shows a different concavity. This is because the grain rolling supports a stronger interlocking among the particles with respect to the "bouncing case" so frictional forces

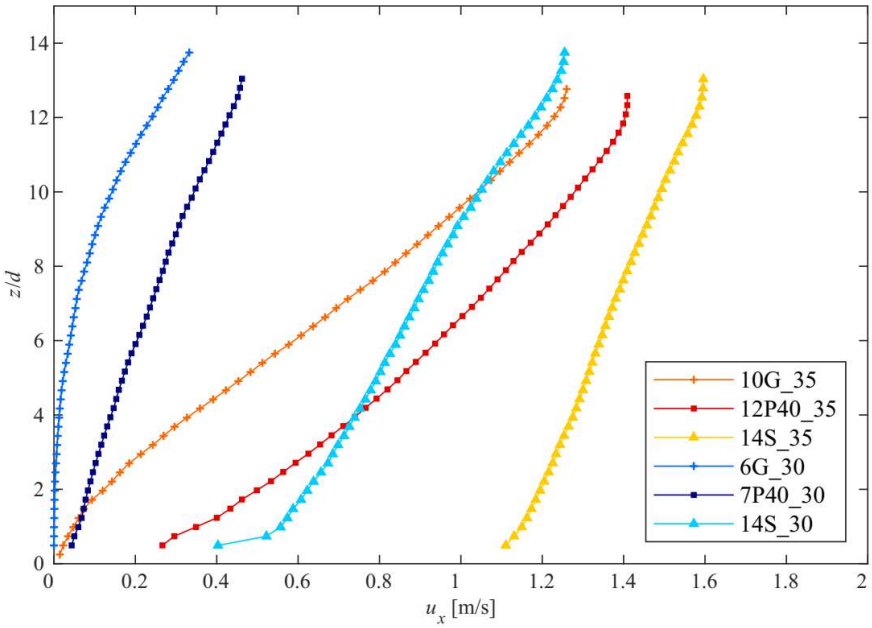

Fig. 6.4 - Comparison among all the sidewall longitudinal velocity profiles with a fixed flow depth for all the investigated basal roughness.

prevail and a convex shape ($\partial_{zz} u_x \geq 0$) of the velocity profile is observed. This prevailing effect of the frictional forces on the collisional stresses can be partially observed also by moving from the 12P40_35 to the 10G_35 in which a weak grain rolling is observed but saltation of the grains is inhibited by the interlocking of the particles in the void of the fixed granular bed. In this case, only a small convexity appears at the base. The convex shape of the velocity profile clearly develops for the 6G_30 run all along the flow depth, for which no-slip and no-grain rolling was observed at the base. Fig. 6.4 highlights the important role played by the granular temperature (Fig. 6.2 and Fig. 6.3). In fact, it seems that, the lower is the grain agitation, namely *T,* the blunter is the sidewall velocity profile. Moreover, for very small value of *T*, the sidewall longitudinal velocity profiles can exhibit a convex shape.

The analysis of the shape of the free surface profiles is carried out by employing the shape coefficient introduced by Sheng et al. (2011) and showed in Eq. (27). In Fig. 6.5, the coefficient *f* is plotted against the mass flow rate Q_m. As one can see, the shape of the free surface velocity profiles remains the same in all the experiments performed on the S-bed, showing a weak dependence on the mass flow rate in case of both the analysed inclination angles of the chute. In case of $\alpha = 35°$ (Fig. 6.5a), with a fixed mass flow rate, the higher is the basal roughness the higher is the *f* coefficient. This trend cannot be observed in case of $\alpha = 30°$ (Fig. 6.5b). In case of both $\alpha = 30°$ and $\alpha = 35°$, for high values of Q_m, the curves related to the rough surfaces seem to collapse on the *f*-Q_m curve of the respective smooth beds. This means that the effect of the basal roughness on the free

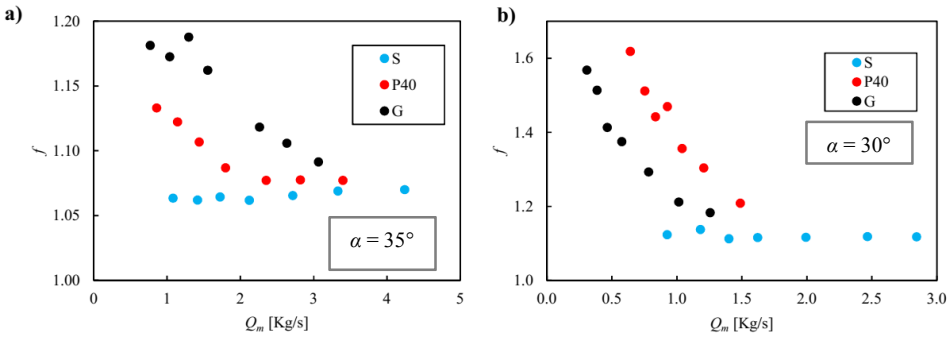

Fig. 6.5 - Shape factor f plotted against the mass flow rate Q_m: a) $\alpha = 35°$; b) $\alpha = 30°$.

surface velocity profiles disappears when the mass flow rate is high enough. This could be due to both the strong agitation of the grains in the upper collisional layer and the presence of a well-established core layer that could soften the influence of the perturbation induced by the rough bed KBC.

6.2 Erodible bed

The sidewall velocity profiles related to the erodible bed are compared in Fig. 6.6. As one can see, the experiments performed in the narrower channel are faster. This is mainly due to the sidewall resistances. As pointed out by Taberlet et al. (2003), the inclination of the flowing layer β_{flow} depends on the ratio h_{flow}/W (see Sect. 2.5.3, Eq. (17)). In the case of a smaller W and with a fixed flow depth h_{flow}, β_{flow} must be higher so the driving forces are higher and the granular flows are faster. Moreover, we found that the master sidewall velocity profile related to the 3cm-wise channel, $u_{x,3}$, can be simply obtained by scaling the master sidewall velocity profile related to the 8cm-

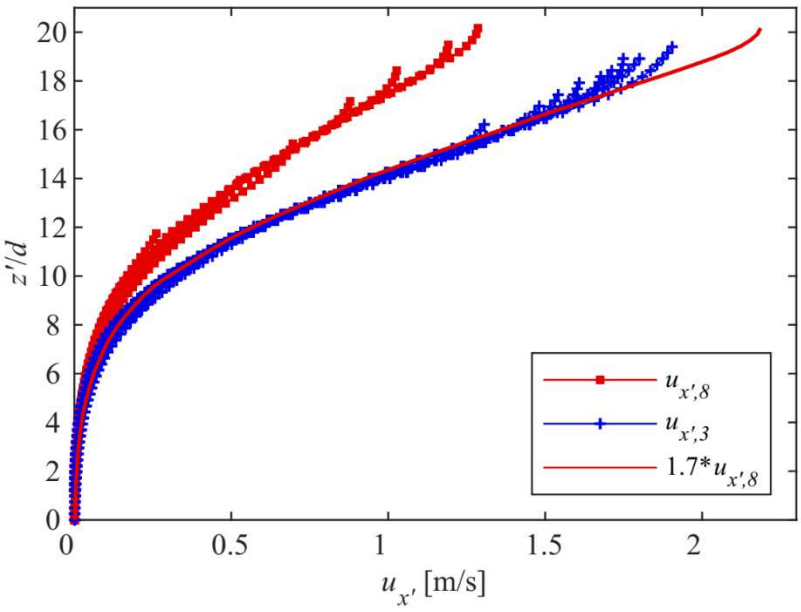

Fig. 6.6 - Comparison between the experiments on erodible bed. Red markers correspond to the runs performed in the 8cm-wise channel, blue markers to the 3cm-wise channel. Continuous line corresponds to the master curve of the 8cm-wise channel scaled with a constant value of 1.7.

wise channel, $u_{x,8}$, with a constant value with the depth and equal to ≈1.7. This is a very interesting result, since the effects of different sidewall forces are quantified by a single coefficient.

The volume fraction profiles aligned at the free surface and related to W = 8cm and W = 3cm are plotted together in Fig. 6.7. As one can see, in the core region, c_{3D} lies in the range 0.55÷0.6 in both the experimental campaign. The thickness of the upper layer is slightly different: in the E_3 experiments, the thickness is slightly larger than in the E_8 experimental campaign. This is probably due to the different grain agitation in the upper layer. Granular

temperature in E_3 is almost twice T in E_8 experiments, due to the higher longitudinal velocities. Therefore, the grains collide in a more chaotic way and they occupy more space.

The shape of the velocity profiles at the free surface are compared in Fig. 6.8. The coefficient f is plotted against the mass flow rate per unit of width Q_m/W. As one can see, the lower is Q_m/W the higher is f, confirming what was previously observed in the case of fixed bed. Moreover, when the mass flow rate per unit of width is high enough, the curves tend to be flatter. The curves related to the two channels approximately collapse into a unique curve if Q_m/W >15 Kg/(m*s).

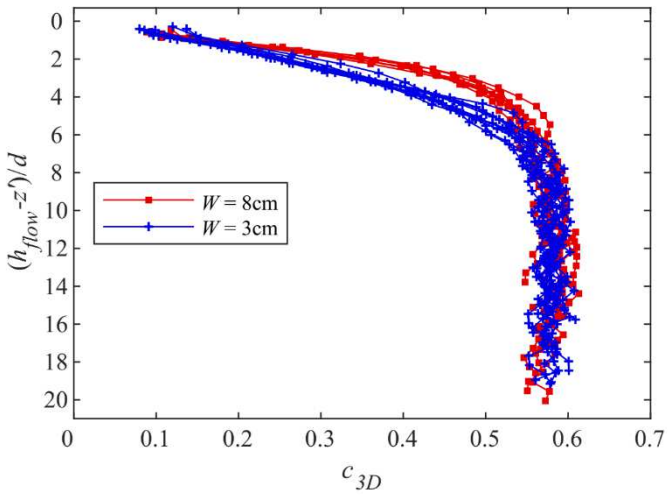

Fig. 6.7 - Volume fraction profiles aligned at the free surface. Red markers correspond to the runs performed in the 8cm-wise channel, blue markers to the experiments carried out in the 3cm-wise channel.

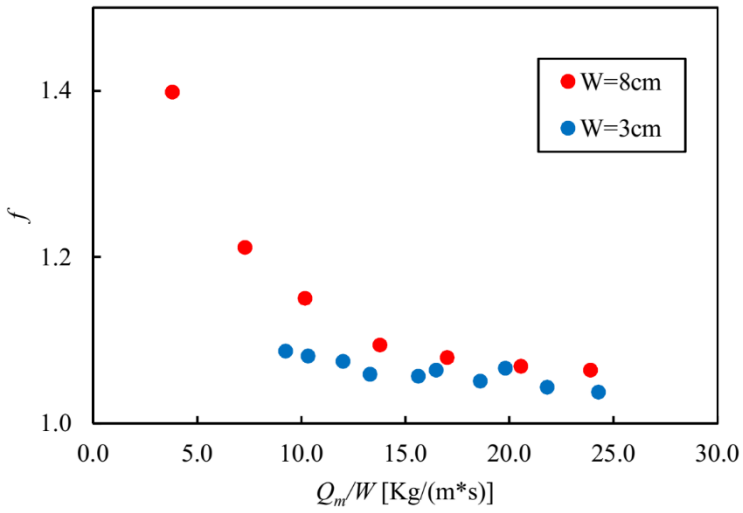

Fig. 6.8 - Shape factor *f* plotted against the mass flow rate per unit of widh Q_m/W. Red markers correspond to the runs performed in the 8cm-wise channel, blue markers to the 3cm-wise channel.

7. Application of the $\mu(I)$ rheology to interpret the laboratory results

In this section, an application of the $\mu(I)$ rheology is presented. The goal is to provide preliminary information about the constitutive law of granular materials.

Before going into details, it is important recalling the $\mu(I)$ rheology presented in Sect. 2.3.4 (GDR MiDi 2004; Jop et al. 2005). It is based on a dimensionless number, called Inertial Number I, describing the relative importance of inertia and confining stresses $I = \dot{\gamma} d / \sqrt{P/\rho_s}$, where $\dot{\gamma}$ is the shear rate, d is the grain diameter, P are normal pressures and ρ_s is the grain density. In the $\mu(I)$ rheology, shear stresses, τ, are proportional to the normal pressures P through a friction coefficient $\mu(I)$ that depends on the Inertial Number: $\mu(I) = \mu_s + (\mu_2 - \mu_s)/(I_0/I + 1)$, where μ_s, μ_2 and I_0 are parameters depending on the granular material (Jop et al. 2005). In particular, $\mu_s \approx \tan\varphi$, where φ is the internal angle of friction of the granular material. Since $\varphi = 27°$, μ_s is a known quantity and is equal to 0.51. The other two rheological parameters, μ_2 and I_0, will be calibrated.

Because of time constraints, the numerical analysis was focused only on the comparison with two experimental campaigns: experiments performed in the 8cm-wise channel over the erodible bed, E_8, and experiments carried out in the same channel over the Bakelite basal surface with inclination angle of the chute $\alpha = 30°$, S_30. In the former experimental campaign, uniform

flow condition occurs. A layer of granular material of constant thickness and inclined with a certain angle with respect to the horizontal flows over the erodible bed. The grains exhibit long-lasting contacts and smaller and smaller shear deformations while going deep in the granular pile. In the latter experimental campaign, steady granular flows were studied. In particular, a slip kinematic boundary condition with negligible grain rolling takes place at the bed.

7.1 Implementation of the $\mu(I)$ rheology

The $\mu(I)$ rheology was implemented in a model of chute granular flows which includes the friction forces exerted by the sidewalls. The integration of the theoretical velocities was performed by following an approach similar to Jop et al. (2005), which developed a model for chute uniform flows. However, different from Jop et al. (2005), which assumed that c_{3D} was constant along the flow depth and equal to 0.6 (i.e. the loose random packing), here we decided to employ the volume fraction measurements. In Sect. 7.1.1, the model adopted for uniform dry granular flows is presented. The model extended to steady chute dry granular flows is presented in Sect. 7.1.2.

7.1.1 Uniform flow condition

The numerical integration of the longitudinal velocity profiles, $u_{x,calc}$, was carried out by writing the momentum balance on a control volume, Ω,

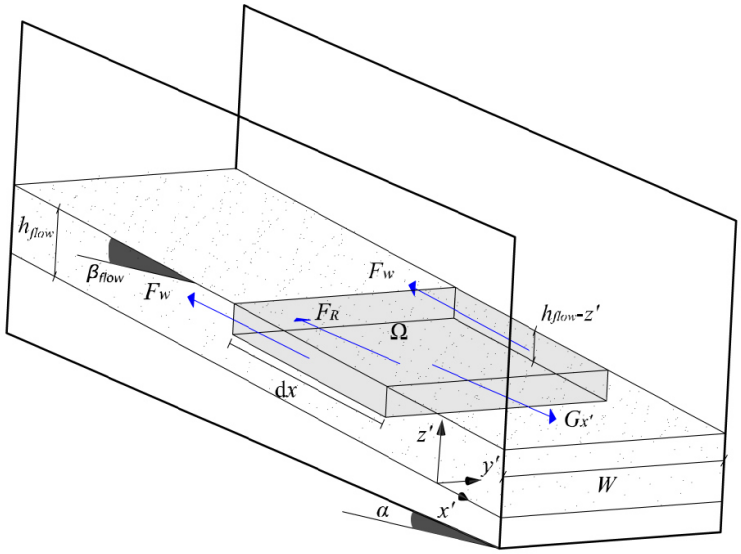

Fig. 7.1 - Sketch of the model used for the momentum balance for uniform flows.

delimited by the free surface, the sidewalls and a surface parallel to the free surface, as shown in Fig. 7.1. The reference system (0, *x*', *y*', *z*') was used, where *x*' and *z*' are the axes parallel and perpendicular to the free surface, respectively. Since the inclination of the free surface with respect to the horizontal, β_{flow}, varies with the flow rates, specifically increases due to the effect of the sidewall friction (Eq. (17)), the reference system change its orientation in each experiment.

The result of the numerical integration is a velocity profile representative of the entire cross section. The comparison among the velocities predicted by the model and the experimental velocities taken at the sidewall cannot be straightforwardly performed. In fact, as observed from the free surface velocity measurements, the velocity profiles taken at the sidewall vary along

the transverse direction. Consequently, we need to do some hypotheses on the velocity field across the channel. By using the approach of Sheng et al. (2011), the *y'*-averaged velocity, $u_{x',y'\text{-}aver}$, can be considered a scaled quantity of the sidewall velocity, $u_{x'}$. The scaling factor, *f*, generally depends on *x*' and *z*' (Eq. (20)). Since the flow is uniform, $u_{x',y'\text{-}aver}$ can be estimated with the relation

$$u_{x',y'-\text{aver}}(z') = \frac{1}{W}\int_W u_{x'}(y',z')\,dy \approx f(z')\,u_{x'}(z'). \qquad (28)$$

In our measurements, the scaling factor *f* can be calculated only at the free surface. By assuming that *f* keeps constant along *z*', $u_{x',y'\text{-}aver}$ can be expressed by:

$$u_{x',y'-\text{aver}}(z') \approx f(h_{flow})\,u_{x'}(z') \qquad (29)$$

The numerical integrated velocity profiles, $u_{x',calc}$, will be thus compared with the *y'*-averaged velocity profiles, $u_{x',y'\text{-}aver}$, obtained with Eq. (29).

Since no scaling factor like (20) is available for the volume fraction field, it is assumed that $\partial_{y'} c_{3D}(x',y',z') \approx 0$. By considering that the transverse velocity at the free surface is very small compared to the longitudinal velocity, one can reasonable assume that the shear mostly occurs in the *x'z'* plane. Therefore, the flow can be viewed as an approximately planar shear flow and the two-dimensional form of the $\mu(I)$ rheology can be used (Sect. 2.3.4, Eqs. (12), (13)). The term *P*, which indicates the normal pressures in (12) and (13), reduces to the vertical normal pressures along the *z'*-direction, $\sigma_{z'}$. By assuming an hydrostatic distribution of the pressures, $\sigma_{z'}$ can be expressed by:

$$\sigma_{z'}(z') = \rho_s g_z c_m(z')(h_{flow} - z') \qquad (30)$$

where ρ_s is the grain density, $c_m(z') = 1/(h_{flow} - z') \int_{z'}^{h_{flow}} c_{3D}(\xi) d\xi$ is the integral mean of c_{3D} in (h_{flow}-z'), h_{flow} is thickness of the flowing layer (Tab. 4.4), $g_{z'} = g \cos \beta_{flow}$.

By neglecting the friction force due to the air, the momentum balance related to the control volume Ω along the x'-direction can be written as:

$$G_{x'} - F_R - 2F_W = 0 \qquad (31)$$

where:

- $G_{x'} = (h_{flow} - z') W \rho_s c_m(z') g_{x'} dx'$ is the weight of the control volume along the x'-direction and $g_{x'} = g \sin \beta_{flow}$;
- $F_R = W \tau(z) dx'$ is the resistance exerted by the granular flow at the lower surface of Ω, where $\tau(z')$ is the shear stress predicted by the $\mu(I)$ rheology: $\tau(z') = \mu(I(z'))(\rho_s g_{z'} c_m(z')(h_{flow} - z'))$;
- The term $2F_w$ represents the two forces exerted at the sidewalls.

Similar to Jop et al. (2005), F_w is estimated by assuming a Coulumbian resistance, $F_w = dx' \mu_w \rho_s g_{z'} \int_{z'}^{h_{flow}} c_m(\xi) (h - \xi) d\xi$, where μ_w is an empirical factor which takes into account the uncertainties related to the Coulomb model and the anisotropy of the normal stresses (e.g. Gray et al. 1999; Hungr 1995; Sarno et al. 2013). μ_w is assumed constant along z'.

Preliminary calibrations were performed using a unique value of μ_w for all the experiments. Despite the employment of the calibrated rheological parameters I_0 and μ_2, the location of the interface between flowing layer and creep layer predicted by the model, namely the depth below which $u_{x',calc}$ =

0 and above which $u_{x',calc} > 0$, was found to be very deep in the granular pile. Moreover, theoretical velocity profiles and experimental velocity profiles differed widely. To solve this issue, we decided to focus on the equilibrium of the entire flowing layer. By using Eq. (31) imposing $z'=0$, one can perform the momentum balance of the flowing layer. The Eq. (31) reduces to the experimental relation found by Taberlet et al. (2003) of Eq. (17):

$$\tan \beta_{flow} = \tan \varphi + \mu_w \frac{h_{flow}}{W} \qquad (32)$$

where φ is the internal angle of friction of the granular material and μ_w is the effective friction coefficient at the sidewall. It is worth underlining that no rheological assumptions are in (32) since the shear rate does not appear in the aforementioned equation. As you can see, Eq. (32) provides a linear relation between h_{flow}/W and β_{flow}.

In order to check if the experimental measurements, related to the E_8 experiments over erodible bed, satisfy Eq. (32), the values of h_{flow}, representing the thickness of the flowing layer to which corresponds an interface located at the depth where $u_{x'} = 0.001$ m/s, are plotted against the inclination of the free surface, β_{flow}, for all the E_8 experiments. As you can see, the points do not exactly align on a straight line. Moreover, it seems that the experimental points follow a double linear trend. Many reasons could induce the non-alignment of the points. The discrepancies could be because the rate-independent Coulumbian relation used for modeling the sidewall friction could be unrealistic. Moreover, the coefficient μ_w is considered constant along the flow depth. This could be a strong assumption. In fact, when normal pressures increases, namely when the distance from the free

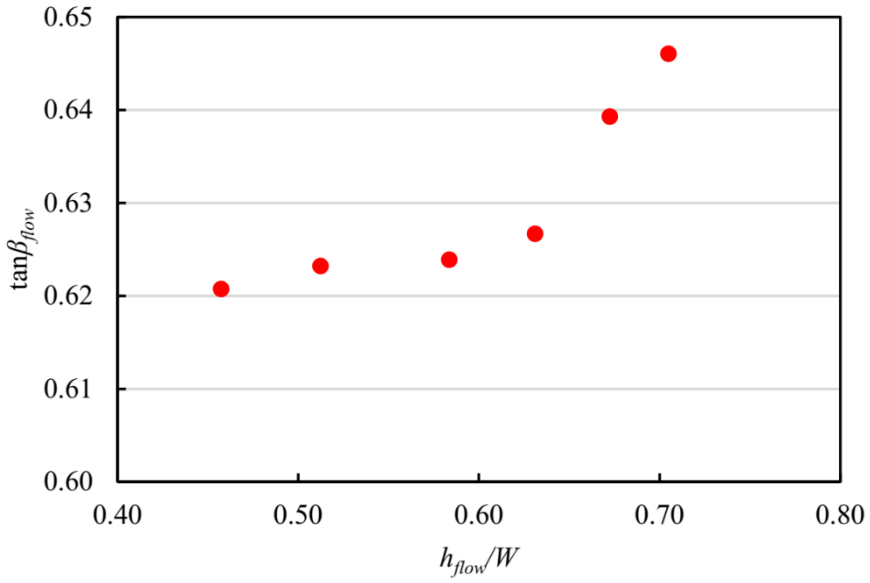

Fig. 7.2 – Relation between h_{flow}/W and β_{flow} for the experiments over erodible bed performed in 8cm-wise channel (E_8).

surface increases, friction at the sidewalls could be influenced by different mechanisms such as the force chains (Mills et al. 1999; da Cruz et al. 2005). Strong uncertainties are also related to the identification of the interface between flowing layer and creep layer and to the assumption that, at the interface, a purely Coulombian equation is capable to describe all the dissipation mechanisms occurring in the granular flow. Moreover, the experimental measurements of h_{flow} and β_{flow} could be affected by some errors. Given these uncertainties, in this model, the choice of a unique coefficient for all the experiments and constant along the flow depth, is a very strong assumption. Therefore, we decided to use different *z'*-averaged values of the μ_w coefficient for each experiment.

The choice of μ_w was mainly based on the resulting position of the interface, namely at the depth where the equilibrium of the flowing layer is reached. In fact, as already explained in the previous sections, a clear separation between the faster and the slower layers of granular material does not exist since velocity exponentially decay while going toward the erodible bed (Komatsu et al. 2001). We investigated a range of positions to which corresponded high values of the volume fraction (≈0.6) and small values of the longitudinal velocities (up to 0.05 m/s), namely where frictional forces mainly take place in the granular medium. The equilibrium of the flowing layer was imposed in such a way that the resulting theoretical profiles were capable to approximate the linear trend of the experimental velocity, namely the part of the velocity profile related to the flowing layer. It was chosen the depth to which corresponded a longitudinal velocity $u_{x'}$ of 0.01 m/s. The values of μ_w used in the numerical integrations are shown in Tab. 7.1.

Tab. 7.1 – Values of the μ_w coefficients used for the integration of the velocity profiles in case of uniform granular flows.

Exp. ID	μ_w
6E_8	0.303
8E_8	0.243
10E_8	0.222
12E_8	0.196
14E_8	0.185
16E_8	0.193
18E_8	0.194

7.1.2 Steady flow condition

The model presented for chute uniform flows in Sect. 7.1.1 was extended to steady granular flows over fixed bed. The origin of the reference system was set at the fixed bed in order to include the entire flow field (Fig. 7.3). The control volume Ω is delimited by the free surface, the sidewalls and a surface parallel to the fixed bed.

Since the inclination angle of the free surface, β, with respect to the inclination angle of the channel, α, is small ($|\beta| = 0° - 2°$, Tab. 4.3) can assume that $\partial_x c_{3D}(x, y, z) \approx 0$ and $\partial_x u(x, y, z) \approx 0$. An additional force, d$\sigma_x$, was considered with respect to the uniform case due to the flow depth gradient along the x-direction. It can be calculated as

$$d\sigma_x = -K_x \, dx \, W \left[\rho_s c_m (z) g_z (h - z) \tan \beta \right] \qquad (33)$$

In (33), the coefficient K_x represent the earth pressure coefficient along x-direction and it is expected to vary in the range between the active state and the isotropic state since the flow elongates along the x-direction, namely $\partial_x h < 0$ (e.g. Gray et al. 1999; Hungr 1995; Carleo et al. 2018).

Three different values of K_x were tried: $K_x = K_{act}^R$, with $K_{act}^R = (1 - \sin\varphi)/(1 + \sin\varphi) = 0.37$ equal to the Rankine active earth pressure coefficient, K_x = 1, and $K_x = K_{act}^{SH}$ with K_{act}^{SH} equal to the earth pressure coefficient from the Savage and Hutter (1989) theory (Sect. 2.5.3). This theory is based on the assumption that the failure of a granular medium

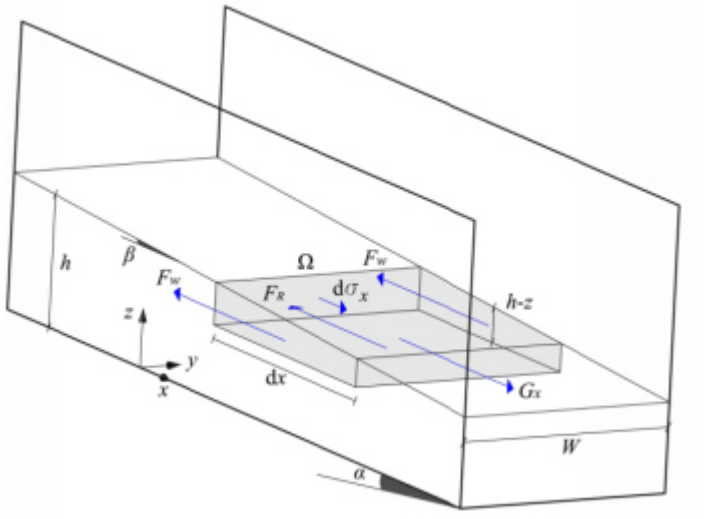

Fig. 7.3 - Momentum balance on the control volume Ω for the experiments over fixed bed.

occurs simultaneously at the bed and along the Coulomb failure plane so $K_{act}^{SH} = 2/\cos^2\varphi\left[1-\sqrt{1-\cos^2\varphi/\cos^2\varphi_{gb}}\right]-1 = 0.53$, where φ_{gp} is the angle of friction between grains and Bakelite and it is equal to 14.5° (Sect. 3.1). The coefficient μ_w, describing the friction at the sidewalls, is here assumed equal to $K_{act}^{R}\tan\varphi_{gp} = 0.133$.

The momentum balance on the control volume Ω is

$$G_x - F_R - 2F_W + d\sigma_x = 0 \qquad (34)$$

Since the basal shear band cannot be described by the $\mu(I)$ rheology, we chose the following boundary condition: $u_{x,calc}\big|_{z=d} = u_{x,y-aver}\big|_{z=d}$.

7.2 Optimization of the rheological parameters

The optimization of the parameters of the $\mu(I)$ rheology, I_0 and μ_2, was performed by comparing the numerical velocities, $u_{x,calc}$, with the experimental velocities averaged across the channel, $u_{x,y\text{-}aver}$, obtained by scaling the sidewall velocities with the coefficient f (Eq. (29), Sheng et al. 2011). The back analysis was carried out separately for the experiments over erodible bed, E_8, and the three different scenarios of the experiments over the fixed smooth bed, S_30. The optimized parameters were obtained by minimizing the global error function E:

$$E\left(I_0,\mu_2\right)=\sqrt{\frac{\sum_{i=1}^{n}\left(RMSE_i\left(I_0,\mu_2\right)\right)^2}{n}} \qquad (35)$$

where n is the number of experiments related to the analyzed experimental campaign. The function E represents the quadratic mean of the root mean square error $RMSE_i$ between the calculated, $u^i_{x,calc}$, and the experimental velocities, $u^i_{x,y-aver}$, related to the experiment i, $RMSE_i(I_0,\mu_2)=\sqrt{\sum_{j=1}^{M}((u^i_{x,calc}(j)-u^i_{x,y-aver}(j)^2)/M}$, where M is the number of velocity measurements for the experiment i. An analysis of the error function E around its minimum, E_{min}, was performed for each experimental campaign. We focused on a small neighborhood of the minimum E_{min} corresponding to the interval $I_{opt}=\left[E_{\min},E_{\min}+\varepsilon_{acc}\right]$, where ε_{acc} is the PIV accuracy of the sidewall velocity measurements and it is equal to 0.004 m/s.

Therefore, at each value of $E \in I_{opt}$ correspond a couple of parameters (I_0, μ_2) which can be considered a solution of the minimization problem of the function E.

7.2.1 Optimization on the experiments performed over the erodible bed (E_8)

The optimization of the rheological parameters on the experiments performed over the erodible bed was conducted with reference to the model for uniform dry granular flows of Sect. 7.1.1. The minimum value of the function E, E_{min}, was found to be 0.067 m/s. The analysis of the error around its minimum provided that, for $E \in I_{opt}$, I_0 and μ_2 exhibit a strong linear relation (R^2>0.98): $\varphi_{sat} = aI_0 + b$ where $\varphi_{sat} = \arctan(\mu_2)$, a is equal to 7.63 and b equal to 30.50. Moreover, the range of validity of the linear function is I_0 = [0.4, 0.8] and φ_{sat} = [33.5°, 36.6°]. The theoretical and the experimental velocity profiles related to the erodible bed are presented in Fig. 7.4. Since the numerical velocity profiles are sensibly independent of any specific choice of (I_0, μ_2) corresponding to $E \in I_{opt}$, they are plotted by setting a value of I_0 lying in the range of validity of the linear relation, namely I_0 = 0.5. Moreover, we decided to present all the profiles aligned at the interface identified by the model, namely aligned at the depth to which correspond a longitudinal velocity $u_{x'}$ of 0.01 m/s. As one can see, the collapse of the experimental velocity profiles (Fig. 7.4a), already discussed in Sect. 5.1, cannot be observed in the back analyzed profiles (Fig. 7.4b).

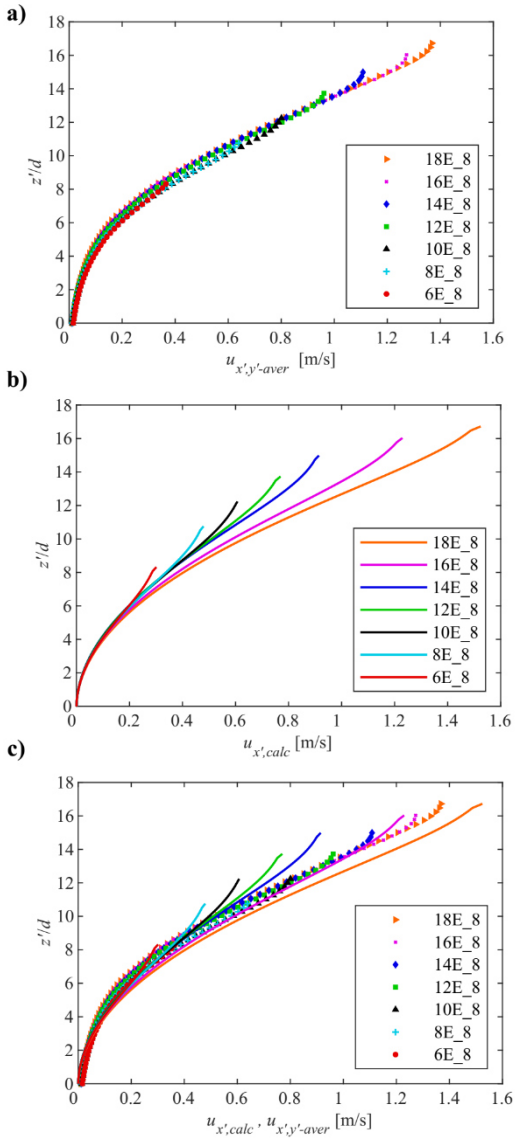

Fig. 7.4 – Theoretical and experimental velocity profiles related to the erodible bed (E_8): a) experimental *y'*-averaged velocity profiles; b) theoretical velocity profiles obtained with I_0 = 0.5 and ϕ_{sat} = 34.3°; c) comparison between the experimental *y'*-averaged velocity profiles (markers) and the numerically integrated profiles (continuous lines).

The $\mu(I)$ rheology implemented in this model for chute granular flows is not

capable to capture this interesting trend of the velocity profiles. However, it seems that the shape of the experimental velocity profiles can be reproduced quite well. A systematic underestimation of the velocities beneath the free surface can be observed in all the runs, except for the 18E_8 experiment for which velocities are slightly overestimated (Fig. 7.4c).

7.2.2 Calibration on the experiments performed over the fixed bed (S_30)

The numerical investigation carried out with reference to the experiments over the Bakelite surface with the inclination angle of the chute α = 30°, S_30, is presented in this section. The back analysis was performed with reference to the model adopted for steady dry granular flows described in Sect. 7.1.2.

We analyzed three different states corresponding to different horizontal normal pressures along the *x*-direction. We investigated the isotropic state, K_x = 1, the active state with K_x evaluated with the Rankine theory, $K_x = K_{act}^R = 0.37$ and an intermediate state corresponding to the active state of the Savage and Hutter (1989) theory, $K_x = K_{act}^{SH} = 0.53$. The absolute minimum of the *E* function, E_{min}, was found to be lower than the one of the E_8 experimental campaign, namely 0.0349 m/s, 0.0186 m/s and 0.0167 m/s for the scenarios with K_x = 1, $K_x = K_{act}^{SH}$ and $K_x = K_{act}^R$, respectively. An optimality interval I_{opt} was found for the back analysed rheological parameter for the S_30 experimental campaign, as well. As in the case of the

Tab. 7.2 - Best-fitting parameters of the linear relation $\phi_{sat} = aI_0 + b$ between ϕ_{sat} and I_0 for the experiment over smooth bed (S_30).

K_x	a	b	Range of φ_{sat}	Range of I_0
1	10.17	30.7	[32.7°, 41.0°]	[0.2, 1.0]
K_{act}^{SH}	8.02	30.1	[32.3°, 39.8°]	[0.3, 1.2]
K_{act}^{R}	7.06	30.1	[32.9°, 40.7°]	[0.4, 1.5]

E_8 experiments, the optimum values of the calibrated I_0 and φ_{sat}, namely the couples corresponding to $E \in I_{opt}$, show a linear relation (R^2>0.99) in all the three scenarios. The best-fitting parameter of such a linear function and its range of validity are listed in Tab. 7.2. As you can see, the range of validity of the linear function and values of the parameter a and b related to the K_{act}^{SH} and K_{act}^{R} scenarios are very similar to the ones of the E_8 experiments. In Fig. 7.5, we decided to report the theoretical velocity profiles related to I_0 = 0.5. The hypothesis of K_x=1 for calculating the term due to the flow depth gradient (Fig. 7.4a), yields larger discrepancies than the other two scenarios with $K_x = K_{act}^{SH}$ and $K_x = K_{act}^{R}$. Specifically, in experiments from 5S_30 to 10S_30, the model systematically underestimates the flow velocities near the free surface, while, in the other experiments, the flow velocities are slightly overestimated. A generally better agreement can be observed with the other two scenarios (Fig. 7.5b, c). This indicates that the optimal K_x value could be less than 1. For the 12S_30 and 14S_30 experiments, in the lower zone of the velocity profiles, it can be noted that the $u_{x,calc}$ slightly underestimates $u_{x,y\text{-}aver}$ and exhibits a weak concavity ($\partial_{zz} u_x < 0$), which is in disagreement with the approximately

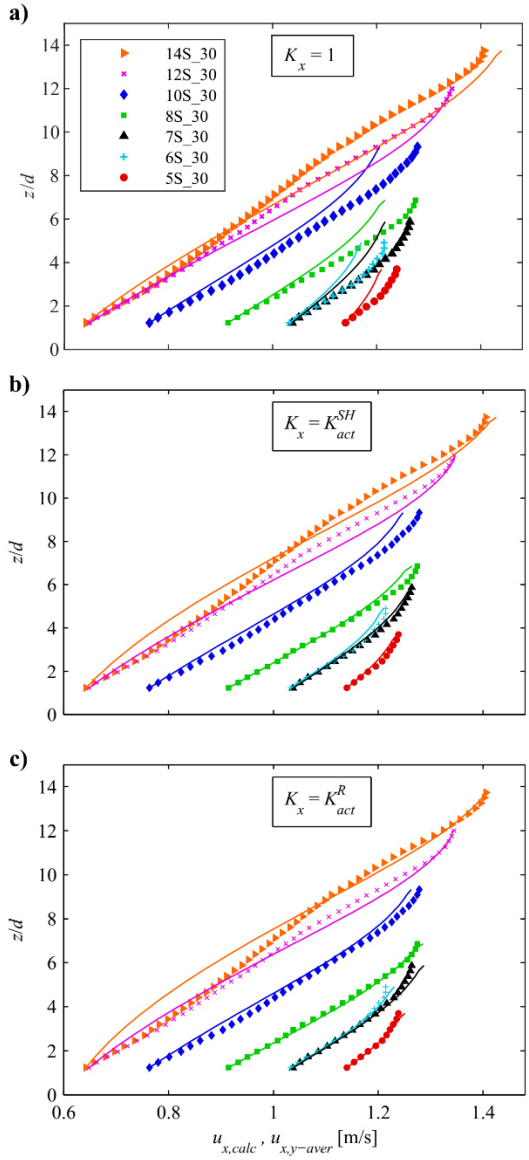

Fig. 7.5 - Experiments on fixed smooth bed (S_30): comparison between the experimental *y*-averaged velocity profiles (markers) and the numerically integrated profiles (continuous lines) obtained with I_0 = 0.5 and a) ϕ_{sat} = 35.8° for K_x = 1, b) ϕ_{sat} = 35.3° for $K_x = K_{act}^{SH} = 0.53$ and c) ϕ_{sat} = 34.1° for $K_x = K_{act}^{R} = 0.37$

linear shape of $u_{x,y\text{-}aver}$. This discrepancy could be due to the assumption of

K_x constant along z and due to the oversimplified hypothesis of the Coulomb-frictional rate-independent law for describing the sidewall resistances.

7.2.3 Discussion on the numerical investigation

The numerical investigation was carried out with reference to two experimental campaigns: experiments over erodible bed performed in the 8cm-wise channel, E_8, and experiments over fixed smooth bed performed in the 8cm-wise channel with inclination angle of the chute $\alpha = 30°$, S_30. The former campaigns corresponds to uniform flow condition while the latter to steady flow condition. In the S_30 experiments, three states were investigated corresponding to different hypotheses on the value of horizontal normal pressures along the x-direction: isotropic state, $K_x = 1$, the active state, according with the Rankine theory, and the active state according with the Savage and Hutter (1989) theory, for which the horizontal normal pressures exhibit values between the Rankine active state and the isotropic state.

The optimization of the rheological parameters I_0 and μ_2 was conducted separately for the two experimental campaigns and for the different scenarios of the fixed bed. The minimum of the error function E (Eq. (35)) was found to be small in all the analyzed cases. The analysis of the neighborhood of the error function E provided that I_0 and μ_2 exhibit a strong linear relation. The range of validity of such linear relation related to the S_30 runs includes the range referred to the E_8 experiments. Moreover, the

coefficients of the linear relation found in case of E_8 runs are very similar to the ones of the active state scenarios of the S_30 runs, to which correspond the lowest value of the error function E. Since the rheological parameters of the $\mu(I)$ rheology are supposed to be only function of the granular material, this could indicate that I_0 and μ_2 related to the employed granular material could lie in the range of validity of the linear relation of the E_8 runs.

The $\mu(I)$ rheology implemented in the model used for chute dry granular flows was capable to approximately reproduce the shape of the velocity profiles both in uniform and steady flow conditions. However, some features of their dynamics, such as the collapse of the velocity profiles in case of uniform flow condition and the linearization of the velocity profiles in case of steady granular flows, were not fully captured by the model. This could be due to both the employed rheology and the model used for chute flows. Non-local effects, such as the force chains (Mills et al. 1999; da Cruz et al. 2005), could take place in case of high flow depth due to high normal pressures and are not taken into account by the $\mu(I)$ rheology. Moreover, such effects could induce different dissipation mechanisms at the sidewall that a rate-independent Coulombian model with a constant earth pressure coefficient is incapable of taking into account.

8. Field investigation

The field activity was conducted during the short research period abroad at the Universitat Politècnica de Catalunya (Barcelona) in collaboration with Prof. Marcel Hürlimann. It focused on the analysis of data from the monitoring station located in the Rebaixader catchment (South Central Pyrenees). Main goal was to detect and classify all the flow processes occurred in the catchment through measurements of ground vibrations and flow depths. Rainfall and infiltration data analysis allowed making preliminary considerations on rainfall intensity thresholds and on the infiltration mechanisms in the triggering area. The observation period was chosen from May 2017 to August 2017, which represents the portion of the year already known for the high debris flow activity in this catchment (Hürlimann et al. 2014).

8.1 Geological, morphological and climate settings of the study site

The Rebaixader catchment is located in the South Central Pyrenees (Fig. 8.1). The bedrock consists of Paleozoic metamorphic and igneous rocks and it is covered by a layer of colluvium and glacial deposits ranging from two

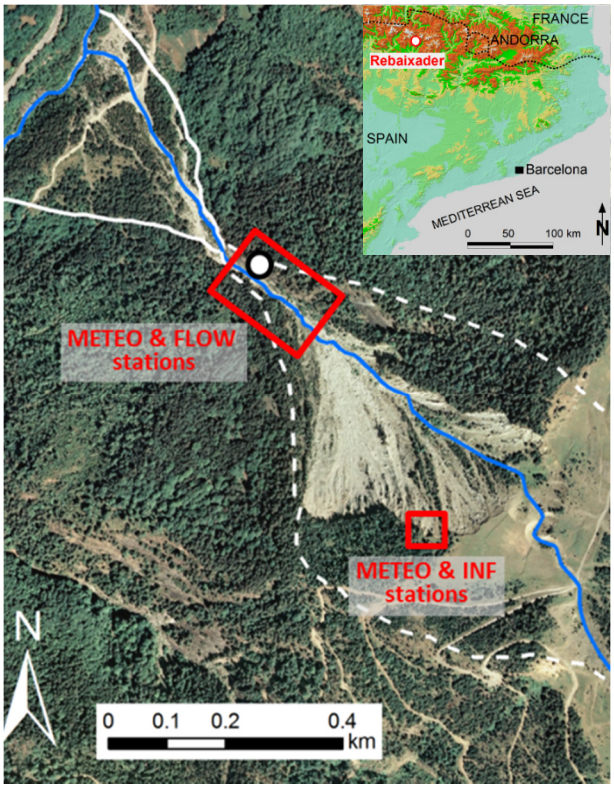

Fig. 8.1 - Situation and overview of the study site. Location of the monitoring system. Inset: location of the Rebaixader catchment.

meters to several tens meters of thickness. The catchment develops from 1345 masl up to 2310 masl, covering an area of 0.53 Km^2. The initiation zone is located in a lateral moraine composed of rocks and boulders in a gravel-sandy matrix (Hürlimann et al. 2012). A large open scarp is clearly visible in the triggering zone and is characterized by having high slope angles ranging from about 30° up to 70° with an unlimited sediment availability. The propagation zone is quite incised in the slope with an average slope angle of about 21°, while, in the deposition zone, inclination is lower with an average slope angle of about 18°. Climate conditions are

influenced by three factors: the orographic effect, the proximity of the Mediterranean Sea and the existence of the west winds from the North Atlantic. In summer, high intensity rainfalls with short durations can be observed, whereas, in autumn, winter and spring, lower intensity and longer duration precipitations occur together with snow precipitations. Most of the flow processes take place in summer during convective rainstorms. Furthermore, a small number of flow processes have been observed in spring, partially due to snowmelt, and in autumn (Hürlimann et al. 2012).

8.2 Description of the monitoring system

The monitoring system consists of three infiltration stations ("INF"), two situated in the scarp and one at the top of the triggering zone, two meteorological stations ("METEO"), one located at the top of the scarp and one in the propagation zone, and a detection station ("FLOW"), in the propagation zone (Fig. 8.1). In this study, we focused on the two INF stations located in the scarp and on the METEO and FLOW stations situated in the channelized zone. The INF stations were installed to monitor soil conditions by measuring pore water pressure (*PWP*), volumetric water content (*VWC*) and suction. The METEO station was used to classify the rainfall episodes. Principal scope of the FLOW station was to identify and classify all the processes that took place in the study period in the Rebaixader catchment through measurements of ground vibrations and flow depths.

The INF stations considered in this work, INF-Scarp1 and INF-Scarp2 (Fig.

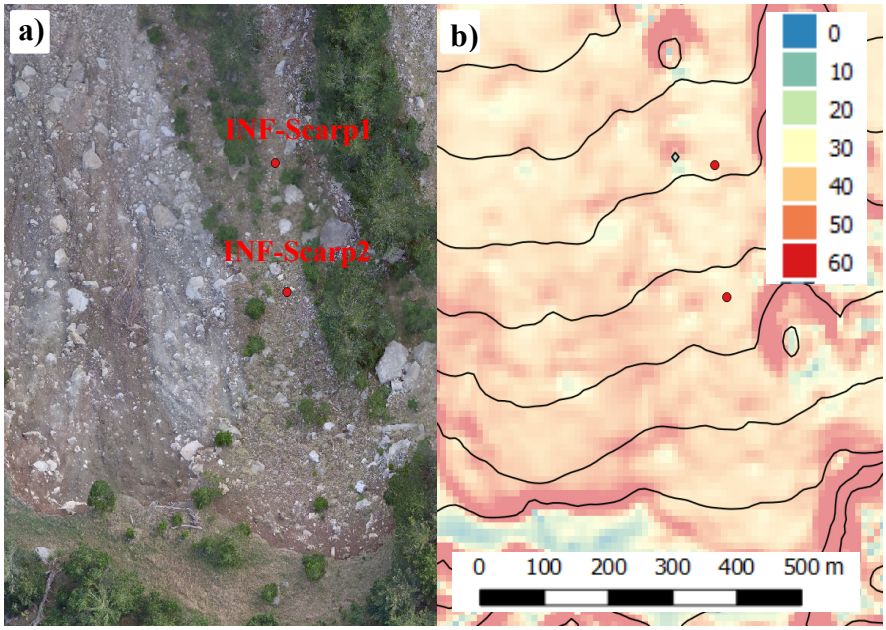

Fig. 8.2 - Infiltration stations in the initiation area. a) Ortophoto and the locations of the two infiltration stations. b) Slope angle map derived from the 0.5 m digital elevation model.

8.2), were installed in a portion of the scarp with a low erosion activity (one can note the presence of grass, bushes and trees). Here, the slope angle ranges from 30° to 40°. INF-Scarp1 is located about 15 m down INF-Scarp2 position (Fig. 8.3). The stations are equipped with piezometers, soil moisture and water potential sensors. Vibrating-wire piezometers from Geosense (model VWP 3200) were employed for measuring pore water pressure through the deformation of a diaphragm. Full scale of the piezometers is of 173 kPa with an accuracy of ±0.173 kPa and a resolution of 0.04325 kPa. The soil moisture sensors from Decagon Devices (model 10HS) were employed. They measure the dielectric permittivity of the soil that can be directly related to the volumetric water content thanks to the dielectric

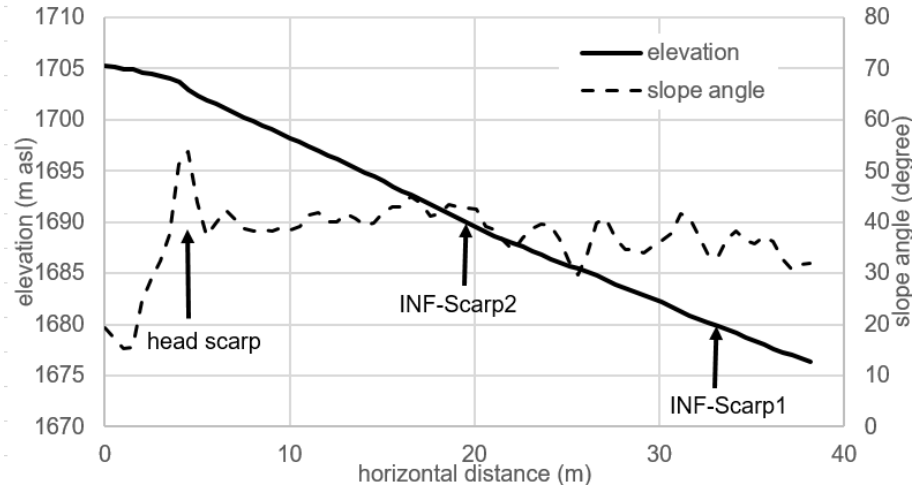

Fig. 8.3 – Topographic profile through the infiltration stations.

constant of water, which is much higher than that of air or soil minerals. These sensors work in a range of 0 - 0.57 m^3/m^3 with an accuracy of ±0.03 m^3/m^3 and a resolution of 0.00008 m^3/m^3. Dielectric water potential sensors (Decagon Devices, model MPS-2) were installed for measuring soil water potential through the dielectric permittivity of a porous ceramic disk placed in the soil. The sensors have an operating range from -5 to -500 kPa with a resolution of 0.1 kPa and an accuracy of ±25%.

In INF-Scarp1, one vertical was investigated. Soil moisture sensors were placed at 15cm, 30cm and 50cm from the soil surface while water potential sensor at 15cm and 50cm. In INF-Scarp2, two verticals were investigated. Soil moisture sensors and piezometers sensor were installed in the lower zone of both verticals (at 50cm and 60cm from the soil surface for left and right vertical, respectively) while, in the upper zone (at a depth of 20cm and

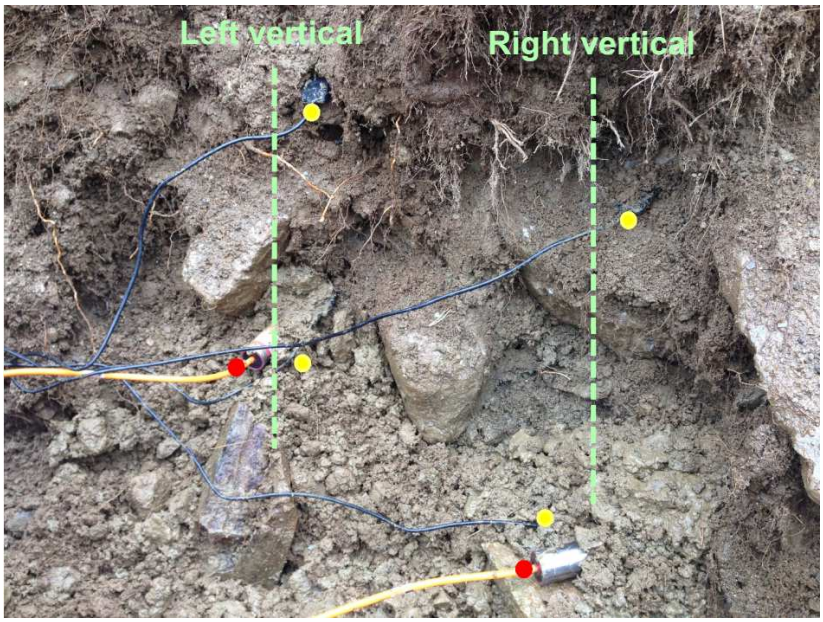

Fig. 8.4 - Photograph of the installed sensors at INF-Scarp2. Yellow circles correspond to soil moisture sensors, red circles to piezometers.

25cm for left and right vertical, respectively), only soil moisture sensors were used, as shown in Fig. 8.4.

The list of all the sensors installed in the INF stations in shown in Tab. 8.1.

A wireless monitoring system has been developed for the recordings of the infiltration data in the scarp. Four nodes, to which sensors are wired connected, transmit all the data to a gateway so that the entire network can be controlled remotely. This system shows lower consumption and long distance of communication with respect to a wired one.

The meteorological station is located in the middle of the transit zone. It consists of a rain gauge, relative humidity and air temperature sensors. The ECRN-100 high-resolution rain gauge of METER measures precipitations

Tab. 8.1 - List of the sensors installed in the scarp area for the infiltration measurements

Name	Type of sensor (model)	Location	Depth [cm]
VWC_1-15	Volumetric water content (DECAGON 10HS)	INF-Scarp1	15
VWC_1-30			30
VWC_1-50			50
WP_1-15	Water potential (DECAGON MPS-2)		15
WP_1-50			50
VWC_2-20	Volumetric water content (DECAGON 10HS)	INF-Scarp2 (left vertical profile)	20
VWC_2-50			50
VWC_2-25		INF-Scarp2 (right vertical profile)	25
VWC_2-60			60
PWP_2-50	Piezometer (Geosense VWP-3200)	INF-Scarp2 (left vertical profile)	50
PWP_2-60		INF-Scarp2 (right vertical profile)	60

with a resolution of 0.2 mm and a sampling rate of 5 minutes. The METEO station is connected to the Campbell Scientific CR200 data logger.

During this observation period, the FLOW station was composed by a camera, to record videos of the passing flow, both a radar and an ultrasonic device, to measure flow depths, and a series of geophones, located along the channel to measure ground vibrations (Arattano 2000). These devices are usually employed in debris flow monitoring stations (Marchi et al. 2002; Badoux et al. 2009; Hürlimann et al. 2011; Comiti et al. 2014; Bel et al. 2017).

In Fig. 8.5, the locations of all the devices installed in the propagation zone are shown. On the left side of the channel, a camera was placed to provide videos and images during day and night. The radar and the ultrasonic device,

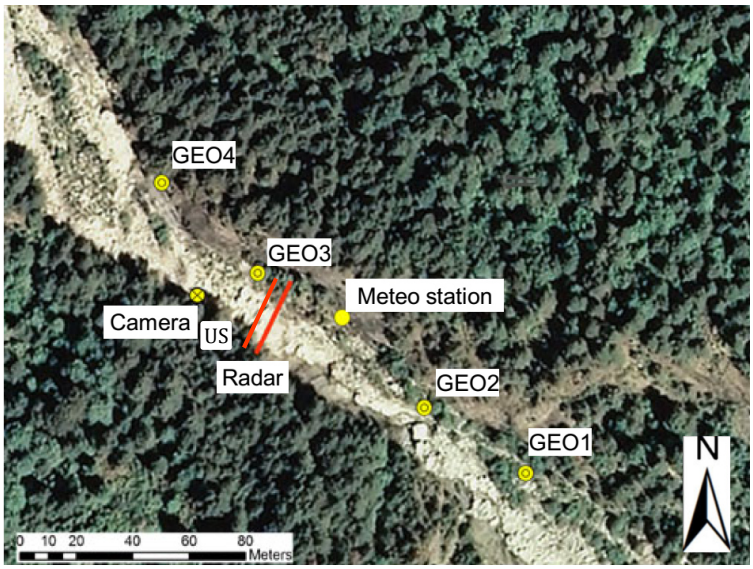

Fig. 8.5 - FLOW and METEO stations in the propagation zone. Location of all the devices.

situated in the proximity of the camera, were mounted on fixed cables at about 6 m over the basal surface of the channel to measure the flow depth.

In this work, data from four geophones were used. Because of robustness and low power consumption, moving-coil geophones (Geospace sensors, model GS-20DX) were employed. They consists of a magnetic mass that oscillates inside a coil due to ground vibrations generating, thus, an electric signal proportional to the ground velocity. This signal is, then, transformed by the data logger into number of impulses per second (*IS*) through a two-step procedure. First, the seismic noise of the study site is eliminated by filtering the original signal using a threshold voltage. From previous studies, the threshold voltage for the Rebaixader catchment corresponds to a ground velocity of 0.17 mm/s (Abanco et al. 2012). In the second step, the same threshold is employed to discretize the signal into impulses that are counted

for each second. The geophones were installed in a metal sheet box attached to the bedrock. A plastic protection covers the boxes to avoid the impact of raindrops.

All the devices installed in the FLOW station were wired connected to a data logger from Campbell Scientific (model CR1000). A 12 V battery, charged by a 30 W solar panel, powered the data logger. Ground vibration data can be recorded continuously (Arattano and Moia 1999) or by switching from a no-event mode into an event-mode in order to avoid high power and high memory consumption (Abancó et al. 2012). In this monitoring station, the data logger was programmed to follow the latter approach. During the "no-event mode", geophone measurements are taken each hour. As soon as one of the geophones records more than 20 IMP/s for three consecutive seconds, "event mode" is activated (Abancó et al. 2012). Radar and geophone measurements are, then, taken every second while the camera is switched on to record a video of the flowing mass. "Event mode" is deactivated when vibrations, recorded at each geophone, are less than 20 IMP/s for 2 consecutive minutes. All the data are sent daily to the server sited in Barcelona through a GSM modem.

8.3 Data and methods

8.3.1 Ground vibrations and flow depth measurements

In this section, the analysis of the data recorded by FLOW station is

presented. Main goal is to detect and classify all the processes occurred in the Rebaixader catchment during the observation period. Informations on both flow depths and ground vibrations were used to this scope.

As shown in Tab. 8.2, three process categories were identified: 1) debris flow processes, *DBF*, 2) fluvial sediment transport processes, *FST* (Heiser et al. 2015), and 3) erosion and accumulation processes in the scarp area, *EAC*. Ground vibrations were used in two different ways: maximum value of impulses per second, IS_{max}, and mean value of impulses per minute, *IM*, both evaluated during the event mode recording. The *IM*-value is defined by

$$IM = \frac{IS_{tot}}{D} \tag{36}$$

where $IS_{tot} = \sum_{i=1}^{n} IS_i$, IS_i is the number of impulses recorded in the second *i*, *n* is the number of measurements recorded during the event mode and *D* is the duration of the process, assumed equal to the duration of the event mode recordings. As one can see, not all the geophones were employed for this classification. The geophone located at the end of the triggering zone, namely in the upper part of the channelized zone, GEO1, was used to avoid false detections of the FLOW station. A threshold on the *IM*-value of 90

Tab. 8.2 - Classification of all the detected processes.

Process	Ground vibration		Flow depth	
	***IM* at GEO1 [IMP/min]**	***IS*$_{max}$ at GEO4 [IMP/sec]**	**y_{max} [m]**	**Shape of hydrograph**
DBF	$IM > 90$	$IS_{max} > 100$	$y_{max} > 0.55$	Peak-tail
FST	$IM > 90$	-	$0.2 \leq y_{max} \leq 0.55$	Increase-decrease
EAC	$IM > 90$	-	$y_{max} < 0.2$	Zero increase

IMP/min was employed. GEO4, which was the geophone installed in the lower part of the channelized zone, was employed in terms of IS_{max} to detect a debris flow. As shown in Abancó et al. (2014), when IS_{max} exceeds the threshold of 100 IMP/sec in GEO4, a fully developed debris flow occurs in the Rebaixader catchment.

The sole information of the ground vibration is not enough to achieve a complete distinction of all the types of process. Flow depth measurement were found to be necessary to distinguish *FST* from *EAC* processes.

In this monitoring system, the ultrasonic device and the radar were used for measuring the flow depth. The analysis of the time series showed that the ultrasonic device, which was the oldest device (Hürlimann et al. 2011), recorded no significant variation in flow depth measurements even when a flow process occurred. Conversely, the radar sensor, which was recently installed, was capable to provide valuable information on the flow depth trend in time. The reason of this discrepancy could be due a slightly changes of the main flow path within the cross section of the channel due to the presence of some blocks transported by the debris flows in the past. Therefore, in this study, only radar recordings were used to measure the flow depth.

A threshold on the maximum flow depth, y_{max}, measured during the whole event mode recording, was used. Moreover, as shown in Fig. 8.6, we found a typical shape of the hydrograph for each type of process: a) a "peak-tail" shape, which indicates *DBF*, b) a "smooth increase-decrease" shape representing *FST*, and c) an "almost zero increase" shape standing for small channel runoff. In case of debris flow (Fig. 8.6a), flow depth abruptly

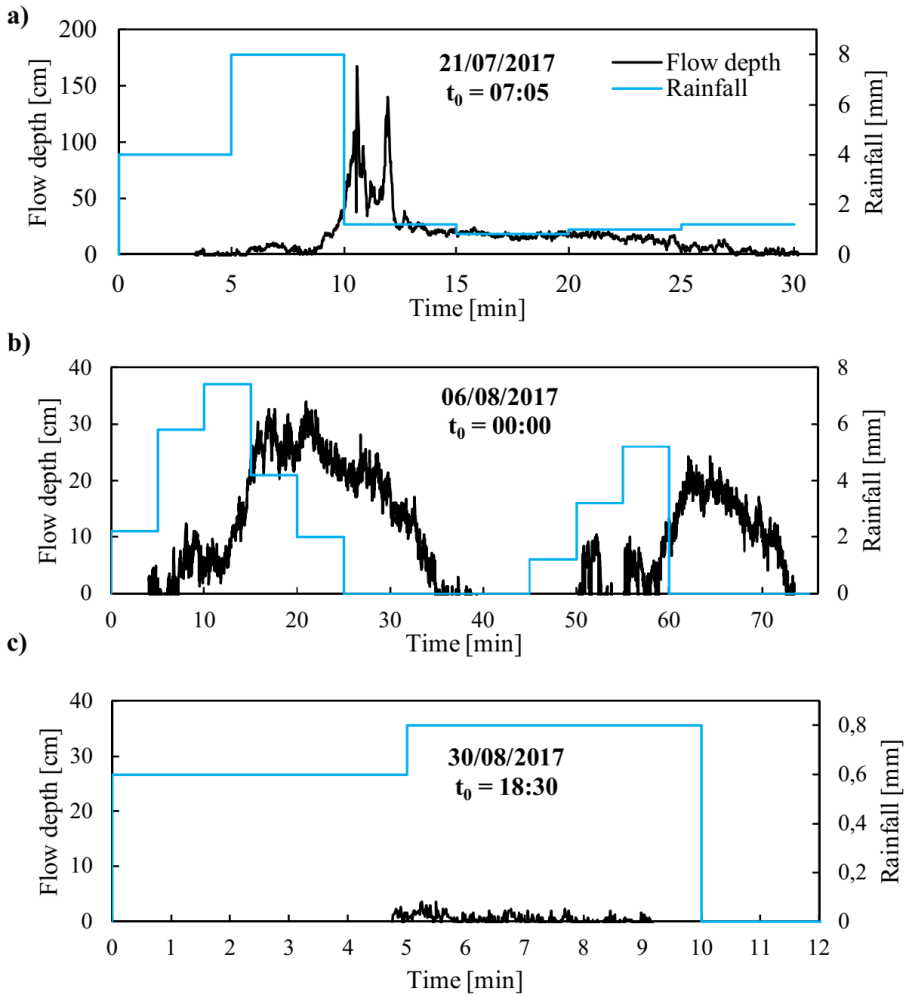

Fig. 8.6 - Examples of typical flow depth trends plotted with the corresponding triggering rainfalls: a) *DBF* process; b) *FST* process; c) *EAC* process. t_0 represents the moment when rainfall started.

increases reaching the maximum value immediately after the rainfall peak. This sudden increase can be clearly related to a debris flow front progress. Successively, other small peaks can be observed in the hydrograph due to the passing of big boulders incorporated into the debris flow body. Then,

flow depth decreases showing a long tail trend. The flow depth trend shown in Fig. 8.6a was already observed in other monitoring stations (Berti et al. 2000; Marchi et al. 2002; Comiti et al. 2014; Bel et al. 2017) and it was typically related to a debris flow progress. A simple threshold on y_{max} equal to 0.55 m was enough to distinguish debris flow processes from other type of processes. We have to say that this threshold is slightly higher than the one previously found by Abancó et al. (2014) for the same catchment which was equal to 0.5 m. In Fig. 8.6b, the typical *FST*-curve is presented. Flow depth slightly increases reaching much lower values than *DBF* and showing two waves of sediments and water that flowed down the slope. It is clearly visible that, also for this flow process, there is a strong relation between the maximum flow depth of each wave and the rainfall peak recorded in 5 minutes by the rain gauge. For this category, maximum flow depth evaluated during the event mode recording was found to be in the range [0.2 m, 0.55 m]. In case of *EAC* processes, despite the activation of the event mode recording, no significant flow depth variations were measured (Fig. 8.6c). This means that the strong erosion processes, which affected the initiation zone, induced the detachment of boulders and big blocks that started flowing down in the scarp but stopped at the beginning of the channel due to bottleneck effect without, thus, any flow depth recordings.

This classification is similar to the one recently proposed by Bel et al. (2017) who investigated the occurrence of debris flow in the Réal Torrent catchment, in the Southern French Prealps. It is based both on flow depth and ground vibration measurements, as well. Moreover, Bel et al. (2017) found a similar value of the maximum flow depth to distinguish debris flow

processes from other processes, namely 0.5m. Differently from Bel et al. (2017), as suggested by Abancó et al. (2014), we added an additional information for debris flow detection, namely the threshold value on IS_{max} (Tab. 8.2). Moreover, the employment of the *IM*-value allowed avoiding false detection of a process.

8.3.2 Rainfall data

The classical approach in threating rainfall data in debris flow hazard analysis is to employ mean intensity-duration plots (Sect. 2.4). In this work, the goal was not to define threshold curves but characterise all the rainfalls that occurred in the study period in the Rebaixader catchment focusing on the precipitations that triggered torrential processes.

A criterion to determine a rainfall episode from the rain gauge time series was imposed in the following manner: if the minimum amount of rainfall recorded in 5 minutes (scan rate of the rain gauge) was higher than 0.6 mm, the precipitation was defined as a rainfall episode. Successively, the beginning and the end of the precipitation were found. By starting from the instant when intensity threshold was exceeded, the beginning of the precipitation, t_0, was found by going backward in time and searching for the first instant corresponding to 15 consecutive minutes of no antecedent rainfall. Instead, the end of a precipitation, t_f, was detected by going forward and searching for the first instant corresponding to 15 consecutive minutes of no succeeding rainfalls. Once a rainfall episode was detected and defined, many quantities could be employed to classify it (mean intensity, duration,

etc.). Previous studies (Abancó et al. 2016) have already identified the parameters that better discriminated precipitations in this catchment. Among these quantities, we decided to focus on the maximum floating intensity, I_{max}. It is defined as the maximum value of the floating intensity, $I(t)$, evaluated on floating time intervals of different durations d, centred at a certain instant t included in the range $[t_0, t_f]$. By choosing d smaller than the total duration of the rainfall episode, I_{max} can can give more importance to the rainfall peak. Since rainfall durations can vary in a very wide range, we decided to investigate small duration of the floating time interval, from 5 minutes (scan rate of the rain gauge) up to 1 hour. It was not always possible to centre properly d at the instant t due to discrete nature of the measurements. In these cases, d was considered backward in t, as shown in Fig. 8.7.

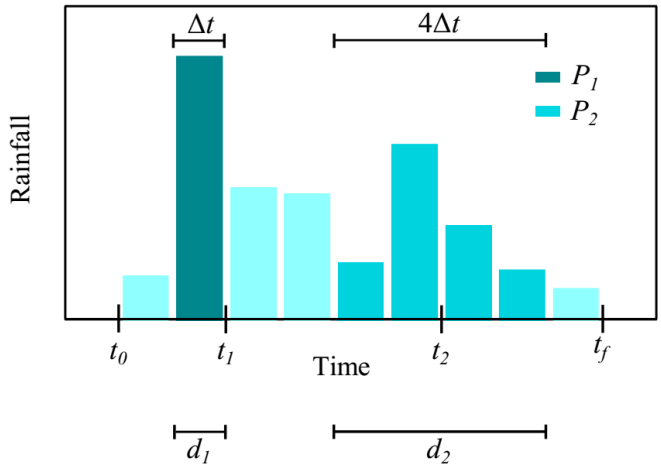

Fig. 8.7 - Example of calculation of floating intensities evaluated within the rainfall event occurred in the interval $[t_0, t_f]$. Evaluation of two different floating intensities at t_1 and t_2 on two different floating time intervals $d_1 = \Delta t$ and $d_2 = 4\Delta t$ (Δt is the sampling rate of the rain gauge). P_1 and P_2 represent the amount of precipitation related to d_1 and d_2, respectively.

8.3.3 Infiltration data

Main goal of this part of the research was to have a general overview on the main infiltration processes that take place during a rainfall episode in the Rebaixader catchment.

As suggested by the manual, the suction sensor calibration is not affected by soil type so the measurements can be straightforwardly used. The conversion of the raw pore water pressure measurements depends only on the engineering units into which the raw data has to be converted. The conversion of the raw *VWC* measurements is more complicated and depends on the soil in which the sensor is buried. Decagon has developed a standard calibration equation to convert the voltage measurements in volumetric water content. Laboratory tests were performed to calibrate the 10HS sensor to the soil of the triggering area. A different calibration equation was obtained. A comparison among the *Decagon equation* and the *Calibration equation* obtained in the laboratory is shown in Fig. 8.8 together with results of the laboratory tests. By looking at the range of the measurements of the 10HS sensors in the 2017 in the study site, one can note that, in case of sensor readings between ≈400 mV and ≈500 mV, both the aforementioned calibration equations provide negative values of the soil moisture, which is physically impossible. In order to partially avoid negative values, we adopted a different calibration equation, called *Test equation* in Fig. 8.8, which approximates the part of the Decagon curve where the concavity changes to a straight line.

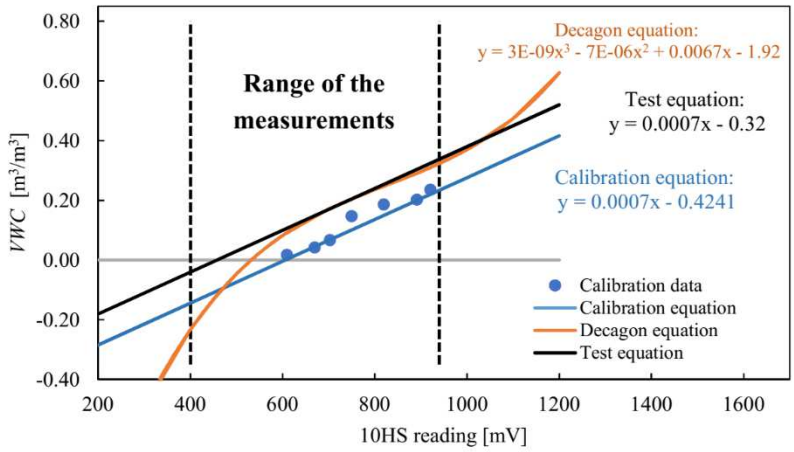

Fig. 8.8 - Comparison among different calibration equations and the results of the laboratory calibration.

The analysis of the infiltration data is very complicated in natural soils. The following procedure was adopted. First step was to look at the piezometer time series in order to verify if soil in the triggering zone reached saturated condition in the observation period. Successively, soil moisture sensor time series were analyzed. In particular, we focused on the detection of the volumetric water content increments in the soil due to a certain rainfall. Response time of the sensors placed in the same vertical were compared to better comprehend the main infiltration mechanisms.

VWC_1-50 sensor showed technical problems and it was not taken into account in the following analysis.

9. Results of the field investigation

In this section, results of the field investigations are presented. Main goal was to detect and classify the flow processes occurred in the Rebaixader catchment (South Central Pyrenees) from May 2017 to August 2017. Ground vibration and flow depth measurements allow distinguishing the different processes. Rainfall data were used to characterize precipitations that triggered a process. The analysis of the infiltration data allows making preliminary considerations on the rainfall infiltration mechanisms in the triggering area.

Before presenting the results, it is useful to recall some important features of the monitoring system and on the quantities employed in the monitoring data analysis (Chapt. 8). The FLOW station is the monitoring station located in the channelized zone and it is composed by geophones, to measure ground vibrations, a radar, to measure flow depth, and a camera to record videos of the passing flows. Two recording modes can be activated. During the "no-event mode", geophone measurements are taken each hour. As soon as one of the geophones records more than 20 IMP/s for three consecutive seconds, "event mode" is activated and flow depth and ground vibration measurements are taken every second. "Event mode" is deactivated when vibrations, recorded at each geophone, are less than 20 IMP/s for 2 consecutive minutes. Data from the FLOW station were used for detection and classification. Ground vibrations were considered in terms of mean value of the impulses per minute, *IM* (Sect. 8.3.1, Eq. (36)), and maximum

value of the impulses per second at GEO4, $IS_{max.}$ The flow depth measurements recorded by the radar were considered in terms of maximum value, y_{max}.

Rainfall measurements were taken every 5 minutes by the METEO station located in the channelized zone. A rainfall event was detected if the minimum amount of precipitation recorded by the rain gauge in 5 minutes was higher 0.6mm. Successively, all the rainfall events were characterized by using the maximum floating intensity, I_{max}, defined as the maximum value of the intensity evaluated on floating time intervals of different durations d centred at a certain instant t between the beginning and the end of the precipitation.

The two INF stations located in the triggering zone provided pore water pressure, volumetric water content and suction measurements every 5 minutes.

The list of all the processes detected during the study period is presented in Tab. 9.1. 19 processes occurred: 2 debris flow processes (*DBF*), 3 fluvial sediment transport processes (*FST*) and 14 erosion and accumulation processes at the end of the scarp (*EAC*).

In Fig. 9.1, the entire rainfall time series is plotted together with the detected processes. As one can see, the flow processes, namely *DBF* and *FST*, occurred in correspondence of the highest rainfall peaks. Most of them occurred in July and August while only one *FST* process was triggered in May (22/05/2017 - 15:23). Some *EAC* processes were detected at the end of

Tab. 9.1 – List of all the processes detected at the Rebaixader catchment from May to August 2017.

Type of process	Date	Duration of the process, D [min]	Ground vibrations					y_{max} [m]	Rainfall intensity, I_{max} [mm/h]				
			IM [IMP/min]				IS_{max} at GEO4 [IMP/sec]						
			GEO1	GEO2	GEO3	GEO4			d = 5min	d = 10min	d = 20min	d = 30min	d = 60min
FST	22/05/2017 - 15:23	87.9	216	60	19	12	14	0.54	72	61,2	42	37,2	31,2
EAC	02/06/2017 - 12:46	5	152	68	11	4	5	0.05	36	24	19,8	13,6	6,8
EAC	08/06/2017 - 23:09	2.1	749	162	17	20	11	0.02	26,4	14,4	8,4	6	4,2
EAC	26/06/2017 - 00:07	14.6	99	11	15	10	8	0.15	43,2	32,4	21,6	15,6	10,4
EAC	27/06/2017 - 18:06	0.7	569	760	3	17	3	0.04	26,4	15,6	8,4	5,6	2,8
DBF	10/07/2017 - 02:55	54	388	143	69	115	143	0.77	100,8	75,6	55,2	54	31
EAC	21/07/2017 - 03:06	0.5	1142	107	0	6	2	0.03	33,6	19,2	12,6	8,4	4,2
DBF	21/07/2017 - 07:08	23.9	414	335	45	214	114	1.67	96	72	42	32,4	24,6
FST	06/08/2017 - 00:14	66.6	481	86	83	97	25	0.34	88,8	79,2	58,8	47,6	25
FST	06/08/2017 - 02:32	77.4	237	21	23	26	44	0.24	57,6	36	18,6	12,4	7,4
EAC	07/08/2017 - 00:39	2.9	632	1	0	0	1	0.06	14,4	9,6	5,4	3,6	1,8
EAC	23/08/2017 - 16:46	19.9	530	68	11	14	10	0.1	19,2	14,4	7,8	5,2	2,6
EAC	24/08/2017 - 00:42	42.9	315	1	1	1	1	0.1	14,4	12	10,2	9,6	8,2
EAC	24/08/2017 - 01:52	16.6	361	0	2	1	1	0.08	14,4	12	10,2	9,6	8,2
EAC	28/08/2017 - 17:10	20.3	732	27	16	17	18	0.1	45,6	32,4	21,6	15,6	9,4
EAC	28/08/2017 - 17:44	15.3	92	3	8	6	8	0.13	45,6	32,4	21,6	15,6	9,4
EAC	30/08/2017 - 18:34	2.1	1198	22	0	0	0	0.04	9,6	8,4	4,2	2,8	1,8
EAC	31/08/2017 - 01:33	10	592	10	3	1	2	0.19	36	26,4	16,2	11,2	6,8
EAC	31/08/2017 - 02:17	2.3	878	0	3	0	0	0.1	19,2	13,2	8,4	6,8	8,4

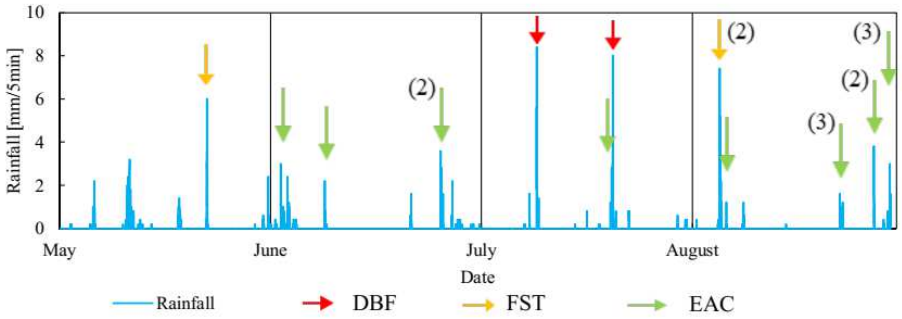

Fig. 9.2 – The entire rainfall time series plotted with the detected processes. Number between brackets indicates the number of detected processes.

June while most of them occurred at the end of August. Data from the FLOW station will be discussed in Sect. 9.1 while data from the METEO and the two INF stations will be presented in Sect. 9.2 and Sect. 9.3, respectively.

9.1 FLOW station measurements

The activation of the "event mode" recording did not always correspond to the occurrence of a process. The analysis of the geophone time series showed that, in some cases, when the "event mode" recording was activated, the geophones recorded very small or even no ground vibrations. In order to avoid the problem of the activation of the recording system due to "unknown" causes, we decided to use the *IM*-value of the ground vibrations recorded by the uppermost sensor, namely GEO1. Since the initial phase of a process takes place in the triggering zone, GEO1 measurements can be used to detect the activations of the "event mode" recording due to the

occurrence of a process. To this scope, we used the quantity *IM*, which stands for mean value of the impulses per minute (Eq. (36)). A threshold on the *IM*-value of 90 IMP/min was used.

In Fig. 9.2, ground vibration, in terms of number of impulses per second, *IS*, and flow depth time series are plotted for the three types of process identified in this catchment. Data recorded during the debris flow occurred in 21/07/2017 at 07:08 are presented in Fig. 9.2a. As one can see, strong vibrations were recorded both in GEO1 and in GEO2 at the beginning of the event mode recording, which means that boulders and blocks are moving down in the scarp reaching the channelized zone. After few minutes, an abrupt increase of the flow height was recorded by the radar. This indicates that a flow was passing under the radar, going downslope the channel. The values of the ground vibrations recorded by GEO4, which is the geophone located in the lower part of the channel, can be used to identify the process. As pointed out by Abancó et al. (2014), if the maximum value of *IS* at GEO4 is higher than 100 IMP/s, the observed process corresponds to a debris flow.

In Fig. 9.2b the geophone and flow depth time series corresponding to the *FST* process occurred in 06/08/2017 at 00:14 are shown. Ground vibrations were detected mostly at GEO1 and before the occurrence of the two surges. The other geophones recorded very small values of *IS* especially at GEO4. This indicates that the kinetic energy of the process was lower with respect to a debris flow.

In Fig. 9.2c, the time series related to the *EAC* process occurred in 30/08/2017 at 18:34 are shown. Vibration are mostly recorded by GEO1 while the other sensors recorded almost null values of *IS*. In this case, rainfall

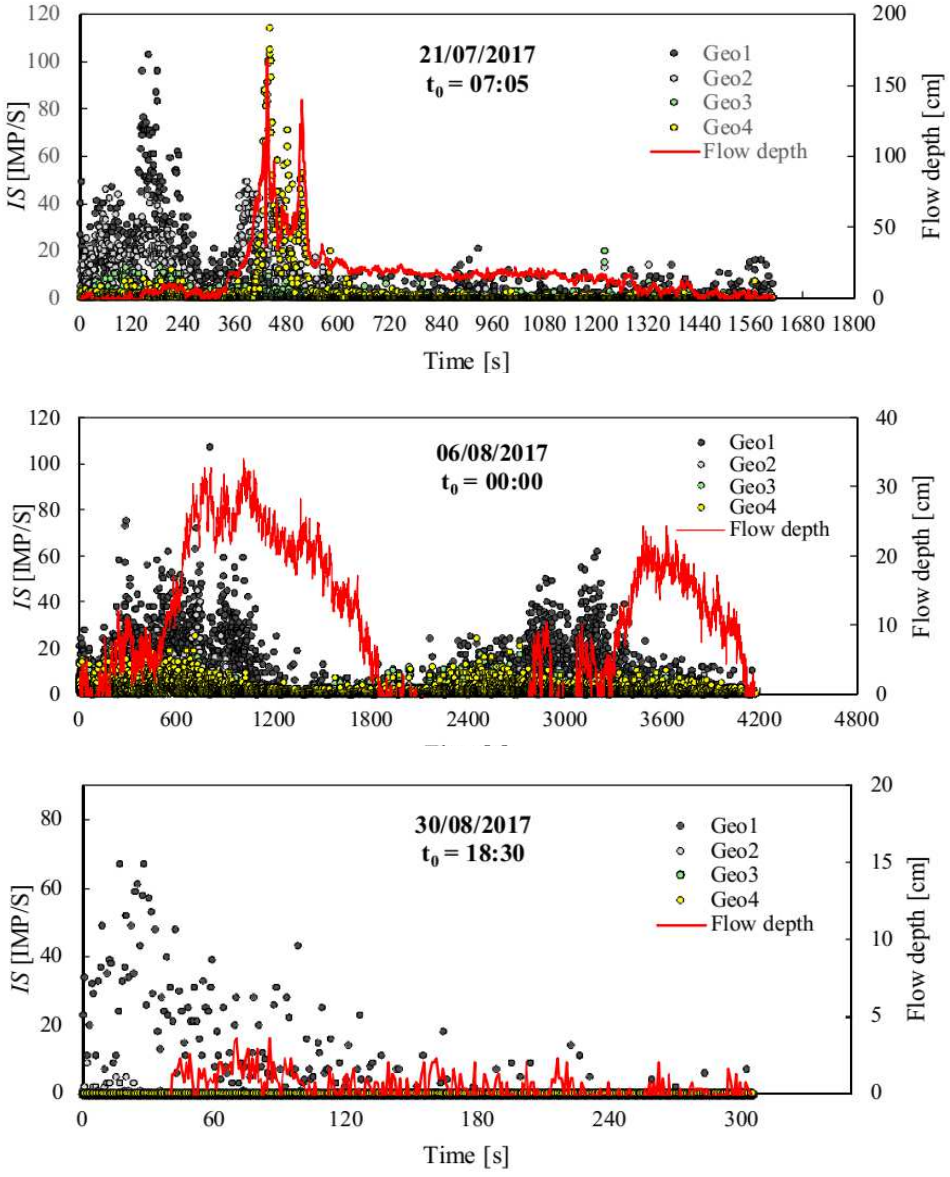

Fig. 9.3 - Examples of ground vibration time series plotted together with the flow depth: a) *DBF* process; b) *FST* process; c) *EAC* process. t_0 represents the moment when rainfall started.

probably induced only the detachment of some boulders and blocks in the

scarp, which stopped in the proximity of the beginning of the channel.
Another information can be obtained from the FLOW station measurements. Since the "event mode" recording is activated when strong vibration are detected, namely when a process indicatively begins, and it is deactivated when ground vibrations are weak, namely when the process indicatively ceases, the duration of the "event mode" recording can be used to have an estimation of the duration of a process, *D*. It was found that *D* is different for each type of process (Tab. 9.1): *FST* processes last more than 1 hour; the two *DBF* processes exhibited durations of some tens of minutes; *EAC* processes usually last some minutes. However, for some *EAC* processes, (e.g. the *EAC* process occurred in 24/08/2017 - 00:42) the duration reaches higher values, up to some tens of minutes. This occurs because strong erosion processes, occurring soon after the activation of the event mode recording and lasting few minutes, are followed by very small and discontinuous erosion processes. This induced the non-deactivation of the event mode recording and thus, sometimes, a great overestimation of the duration of the significant part of the *EAC* process.

9.2 METEO station measurements

During the observation period, 66 rainfall events were detected. By comparing the dates of occurrence of the precipitation with the ones of the detected processes, we found that each process can be related to a single rainfall event. Only in case of the *FST* processes (except the process

occurred in 22/05/2017 at 15:23), two precipitations were detected, each of which corresponding to a surge (see Fig. 8.6). In these cases, the first of the two precipitations was considered as the triggering rainfall for this type of process.

All the rainfall events were characterized by employing the maximum floating intensity, I_{max}, evaluated on different duration, d. Five different durations were investigated: 5min (scan rate of the rain gauge), 10min, 20min, 30min and 60min. The values of I_{max} of the triggering rainfalls, are shown in Tab. 9.1.

All the rainfalls were first compared with the data collected in the past years in the Rebaixader catchment. Abancó et al. (2016) analysed all the precipitations occurred in this catchment from 2009 to 2014. By using the terminology used in this work, they distinguished precipitations that triggered flow processes (TRIG), namely *FST* and *DBF* processes, from rainfalls that did not trigger any flow process (NO TRIG), namely all the precipitations that did not trigger anything or triggered *EAC*. I_{max}-d curves were defined, each of which corresponding to a different probability of TRIG rainfalls exceeding the curve. In Fig. 9.3 the 100% curve, which corresponds to 100% percentage of TRIG rainfalls exceeding the curves for the Rebaixader catchment (grey points), is plotted together with all the 66 rainfall event detected in 2017, distinguished in TRIG and NO TRIG rainfalls. As one can see, the 100% exceedance probability threshold points of 2017 for TRIG rainfalls (red points) are not located below the 100% curve of the Rebaixader catchment. Since the observation period of this field study is shorter than the observation period of Abancó et al. (2016), one can say

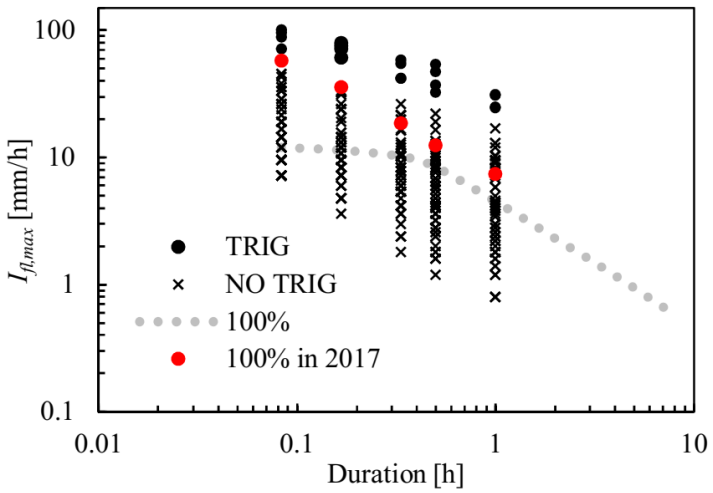

Fig. 9.4 - Rainfall characteristics: maximum floating intensity - duration plot of the 2017 rainfall events. TRIG stands for rainfalls that triggered torrential flows, namely *FST* and *DBF*, and NO TRIG stands for all the rainfalls that triggered nothing or *EAC* processes in 2017. The red markers indicate the 100% exceedance probability points for TRIG rainfalls in 2017. The 100% exceedance probability curve published by Abancó et al. 2016 (grey points) is included for comparison.

that the rainfall measurements of the 2017 are in agreement with the previous observations.

In Fig. 9.4, the maximum flow depth recorded by the FLOW station during the occurrence of a process, y_{max}, is plotted against the maximum floating intensity of the corresponding triggering rainfall. Each graph refers to a different time interval, d, used for the calculation of I_{max}. As one can see, in case of d = 5min and d = 10min (Fig. 9.4a, b), I_{max} seems to increase with y_{max}, which means that an higher rainfall intensity produces an higher flow height in the channel. By increasing d, this trend seems to disappear and the

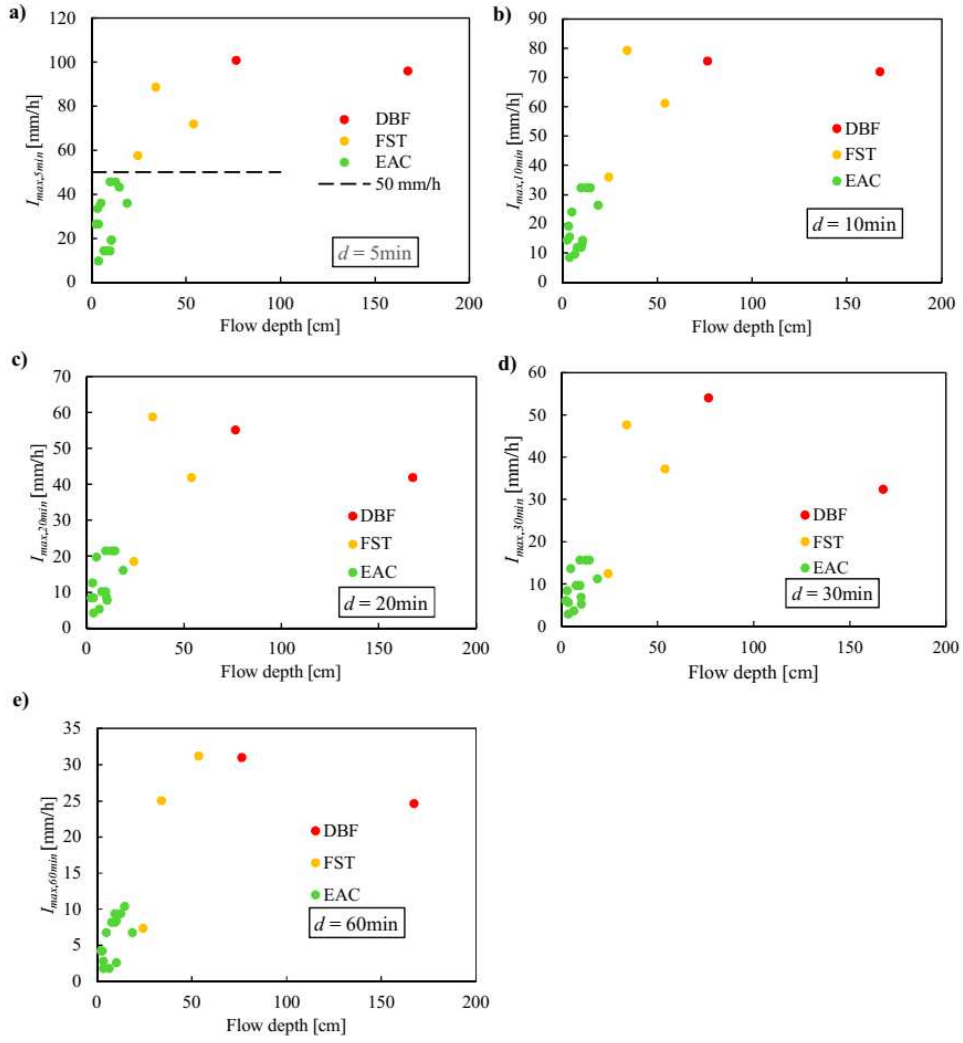

Fig. 9.5 – Maximum floating intensity plotted against the flow depth. Maximum floating intensity was evaluated on a time interval of 5min (a), 10min (b), 20min (c), 30min (d) and 60min.

differences among the triggering precipitations related to different processes seems to level themselves. By focusing on Fig. 9.4a, one can observe that, a

threshold of ≈50 mm/h can be used to distinguish precipitations that triggered flow processes (*FST* and *DBF*) from precipitations that triggered *EAC* processes.

It seems that $I_{max,5min}$ is the most suitable parameter to characterize precipitations in this catchment and it could be indicative of runoff generated debris flow occurring when rainfall intensity exceeds the infiltration capacity of the soil (Bel et al. 2017). However, these remarks must be considered as preliminary observation since the dataset is very small.

9.3 INF station measurements

The analysis of the water potential time series related to the INF-Scarp1 vertical, which sensors are located at -15cm and at -50cm from the soil surface, showed that suction was quite high during the whole observation period. Only after the rainfall events that triggered the *EAC* process in 26/06/2017, all the *DBF* and the *FST* processes an increase of the water potential was observed. The piezometer measurements related to the INF-Scarp2 verticals revealed that pore water pressure, in the nearest of the sensors, was negative during the whole observation period. The analysis of the soil moisture measurements related to both INF-Scarp1 and INF-Scarp2 verticals showed that *VWC* was always lower than the maximum value of *VWC* for this soil, namely 0.3, which corresponds to the mean porosity. All these measurements confirm that, along the analyzed verticals, the soil probably remained in unsaturated conditions during the whole study period.

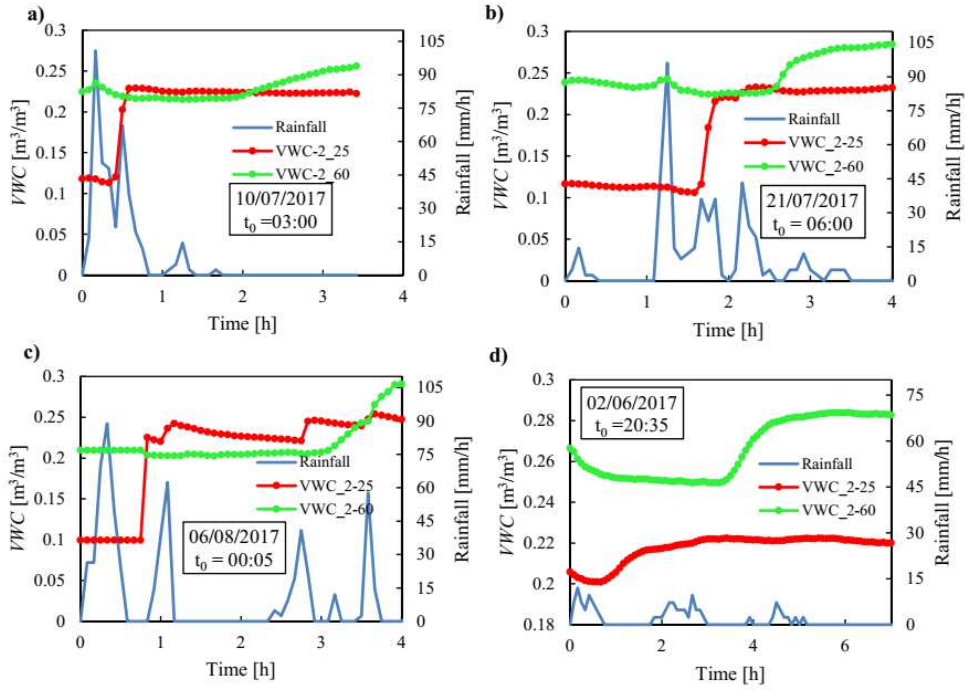

Fig. 9.6 – Examples of *VWC* increases detected in the time series (green and red markers) related to the sensors located in the right vertical of INF-Scarp2. Rainfalls (blue line) are reported, as well.

The analysis of the soil moisture measurements focused on the detection of the *VWC* increments in order to find a correlation between the occurrence of a process and the increase of the soil moisture. Moreover, the response times of the sensors located along the same vertical to the same rainfall event was analyzed, as well.

In Fig. 9.5, the *VWC* time series related to the measurements of the sensors located in the right vertical of INF-Scarp2 is presented. Four cases are shown as an example. In correspondence of the same rainfall events, both the soil moisture sensors, located at -25cm (VWC_2-25) and -60cm (VWC_2-60)

from the soil surface, respectively, detected a *VWC* increase. The increase was identified in correspondence of all the flow processes detected in 2017 (e.g. Fig. 9.5a, b and c) and in case of only one *EAC* process, namely the one occurred in 02/06/2017 (Fig. 9.5d). It was found that a *VWC* increase was observed also in case of rainfalls that did not trigger any process. The response time of the sensors located along the right vertical of INF-Scarp2 is different and depends on the rainfall. The lower sensor reacts always after the upper sensor and the beginning of the increase is typically delayed of 1÷2 h with respect to the beginning of the increase recorded by the upper sensor.

In Fig. 9.6, *VWC* time series related to the measurements of the sensors located in the left vertical of INF-Scarp2 is shown for four cases, as an example. Differently from the right vertical of INF-Scarp2, the *VWC* increase was not always detected in both the sensors. For some rainfall event, only the sensor located at -20cm, namely the uppermost sensor in this vertical, measured an increase of soil moisture (e.g. the *EAC* process occurred in 28/08/2017 at 17:10, Fig. 9.6d). Moreover, it was found that the increase occurred also when the rainfall did not trigger any process (e.g. in Fig. 9.6c). In case of all the flow processes (example in Fig. 9.6a and 9.6b), the increase of the soil moisture was always measured and by both the sensors. The lower sensor always react after the upper sensor, as already observed for the left vertical of INF-Scarp2, but with a lower response time and typically delayed of 5÷90 min.

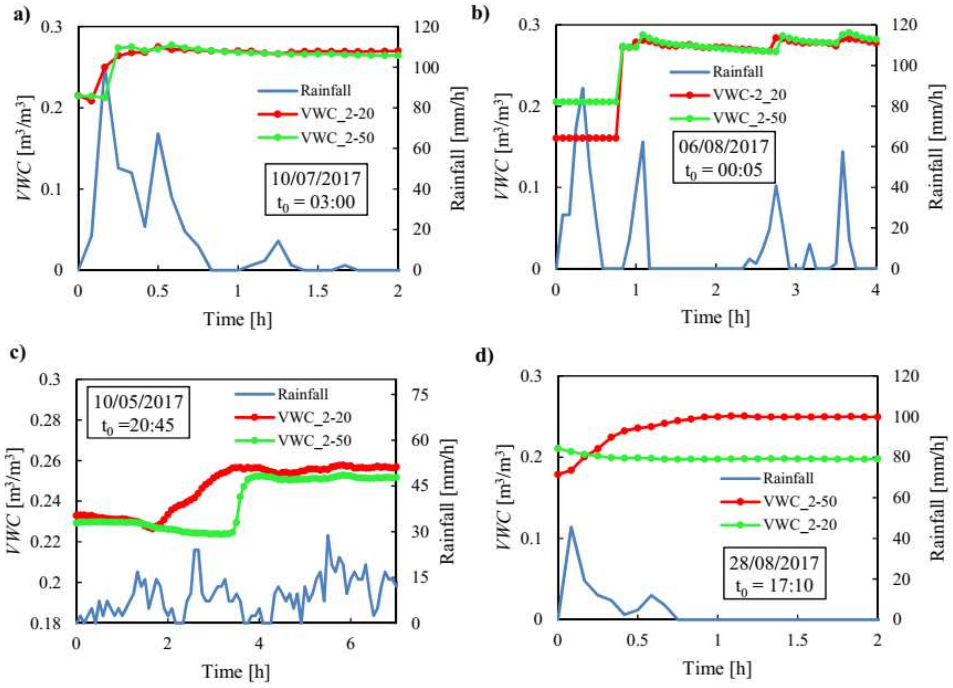

Fig. 9.7 - Examples of *VWC* increases detected in the time series (green and red markers) related to the sensors located in the left vertical of INF-Scarp2. Rainfalls (blue line) are reported, as well..

Four examples of the *VWC* time series from the soil moisture measurements of the sensors located along the INF-Scarp1 vertical is presented in Fig. 9.7. The sensor located at -15cm from the soil surface (VWC_1-15) recorded a *VWC* increase only in case of the rainfall event occurred in 22/05/2017 (Fig. 9.7a), which can be related to the *FST* process occurred in May, while the sensor located at -30cm (VWC_1-15) reacts much more. A soil moisture increase was detected in the VWC_1-30 time series in case of the two detected *DBF* processes (Fig. 9.7b and 9.7c), one *FST* process (22/05/2017 15:23) and in case of a rainfall event that did not trigger any process.

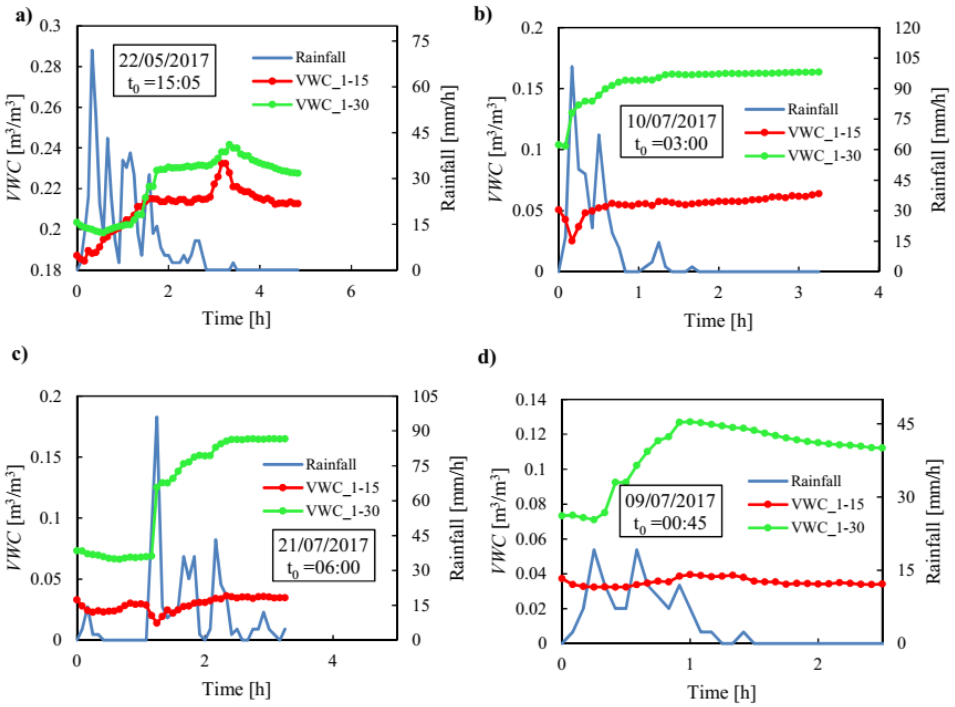

Fig. 9.8 - Examples of *VWC* increases detected in the time series (green and red markers) related to the sensors located in the INF-Scarp1 vertical. Rainfalls (blue line) are reported, as well.

As one can see, the soil response to the same rainfall event was different in each analyzed soil vertical. This highlights the fact that, in natural soil, the analysis of the infiltration mechanisms of the rainfall is very complicated. The strong heterogeneity of the soil can induce the formation of preferential paths through which rainfall infiltrates (Tarboton 2003). This could explain the differences in the delaying time of the response of the sensors located along the INF-Scarp2 verticals. In the INF-Scarp1, the uppermost sensor did not recorded any significant *VWC* increase (except for the rainfall event in

22/05/2017) while the lower sensor recorded an increase of the soil moisture for some rainfall events. Rainfall probably infiltrates through paths that do not always pass through the soil volume investigated by the VWC_1-15 sensor.

10. Conclusions

Granular flows are highly unpredictable and highly hazardous natural phenomena. The study of the triggering mechanisms and of the dynamics of such flows is of fundamental importance for the implementation of the most appropriate countermeasures. This research work was mainly devoted to the study of the effect of the boundaries on the dynamics of steady chute dry granular flows at laboratory scale. Part of this research study was also dedicated to the study of the triggering phase and of the propagation phase of granular flows at catchment scale. The laboratory investigations were performed at Laboratorio di IDraulica Ambientale e Marittima, LIDAM, University of Salerno, while the field campaign was conducted in the Rebaixader catchment (South Central Pyrenees) in collaboration with Prof. Marcel Hürlimann (Universitat Politècnica de Catalunya, Barcelona).

At laboratory scale, open channel experiments were performed. The employed channels allowed investigating different conditions by adjusting the inclination angle of the chute, the channel width, the mass flow rate and the basal roughness. The transparent Plexiglas sidewalls of the channels permitted to employ optical techniques and, thus, to study flows not disturbed by the measurement devices. The main variables which govern the dynamics of dry granular flows were investigated, namely velocity and volume fraction. In particular, velocity measurements were taken both at the sidewall and at the free surface while volume fraction was only measured at the sidewall. The PIV technique was employed for measuring the velocity

field. A multistep approach was used to obtain a quite high spatial resolution of the measurements and limits the *loss-of-pairs* effect. The SOM method, developed at LIDAM (University of Salerno), is here employed to get near-wall volume fraction measurements. It is based on the estimation of the near-wall volume fraction through the two-dimensional volume fraction taken at the sidewall under highly controlled illumination conditions. A local binarization algorithm allows measuring the two-dimensional volume fraction from gray scale images. The employed granular material was the same in all the experimental campaigns and consisted of acetal-polymeric beads with mean diameter d = 3.3mm and internal angle of friction $\varphi = 27°$. The mass flow rate was imposed by varying the upstream gate opening. The effect of the sidewall friction and of the normal pressures, both dependent on the flow depth, were systematically investigated by varying the mass flow rate.

A steady state time interval lasting several seconds was observed in all the experiments. A high repeatability was obtained among the four repetitions carried out for each analyzed boundary condition. All the measurements were first time-averaged within a steady state time interval and then ensemble-averaged among the four repetitions. The experiments can be divided in two groups: experiments over fixed bed and experiments over erodible bed. The first group of experiments comprehends a total of 224 runs. They were carried out in the same channel with a width W = 8cm ($\approx 24d$). Two inclination angles of the chute were studied, namely $\alpha = 30°$ and $\alpha = 35°$, both higher than the internal angle of friction of the granular material. Different fixed basal surfaces, characterized by different

characteristic length of roughness l, were employed: a Bakelite surface, with l<<10μm; three different sandpaper linings P100, P60 and P40, with l equal to 162 μm 269 μm and 425 μm, respectively; a fixed granular basal surface, with $l = d/2 = 1.65$ mm. The second group of experiments was devoted to the study of a configuration that often occurs in nature, in which the sediments flow over a loose bed made up of the same sediments. A small weir was placed at the outlet of the channel in order to obtain a lower wedge of granular material over which a flowing layer develops. In these conditions, uniform flows can be observed. In order to study the effect of the cross section width on the dynamics, two different channels were used, one having width $W = 8$cm (≈24d) and the other $W = 3$cm (≈9d). The same range of thickness of the flowing layer h_{flow} (between ≈10d and ≈20d) was investigated in both the channels. 72 experiments were performed.

Concerning the experiments over fixed bed, the employment of different fixed basal surfaces allowed investigating the influence of different kinematic boundary conditions (KBC) at the bed on the flow dynamics. The occurrence of a particular KBC depends on the normal pressures, on the sidewall resistances and on the basal roughness. The Bakelite basal surface allowed to study a slip KBC both in the experiments with $\alpha = 30°$ and with $\alpha = 35°$. The three sandpaper linings, induced strong rolling and saltation of the grains at the bed for the experiments with $\alpha = 35°$ while only weak grain rolling, progressively inhibited by the increase of the normal pressures, was observed at $\alpha = 30°$. In case of fixed granular bed with $\alpha = 35°$, only a weak grain rolling occurs when flow depth is small, while no-slip and no-grain rolling is present in all the experiments with $\alpha = 30°$.

In case of employment of different sandpaper linings with α = 35°, we observed the same KBC, namely rolling and saltation of grains, at the bed. No significant variations in the flow quantities were observed. Velocity profiles, both at the sidewall and at the free surface, and volume fraction profiles were qualitatively the same. This means that a variation of the characteristic length of roughness at the basal surface do not always induce variation in the flow dynamics.

The combined information of the volume fraction and velocity profiles revealed that the flow, in all the experiments, stratifies into three different regions: a *lower region*, 1*d*-thick, in which the velocity profile is strongly affected by the bed roughness and volume fraction is low; an intermediate *core region*, where volume fraction keeps approximately constant and equal to ≈0.6 and velocity profile is approximately linear (this layer can be assent when the flow depth is not high enough); and, finally, an *upper region*, with a thickness of ≈2*d*÷4*d*, where volume fraction decreases while going towards the free surface and the shapes of velocity profiles are concave ($\partial_{zz} u_x < 0$), resembling a Bagnold scaling.

In the *lower region*, the slip KBC induced the occurrence of a ≈1*d*-thick shear band soon above the fixed basal surface. In case of rough basal surfaces, because of different KBC, the shear band does not occur but volume fraction is small due to the presence of the bed, as well.

When the flow depth is small and the *core region* does not develop, volume fraction exhibits values less than the loose random packing of the granular material (≈0.6) and a concave shape of the longitudinal velocity profile, which covers all the flow depth, was observed. This suggests the occurrence

of a more collisional behavior of the granular material. When the flow depth is high enough, namely normal pressures and the sidewall resistances are high enough, a core region develops up to $\approx 2d \div 4d$ from the free surface exhibiting approximately constant value of the volume fraction and slightly less than 0.6. In this region, the dynamic is still affected by the bed roughness. In particular, in case of slip KBC, the effect of both the normal pressures and the sidewall friction, which is comparable to the friction exerted by the smooth but frictional bed, induced a linearization of the velocity profiles. The shear rate keeps approximately constant for tests with different flow depth. In case of rough bed and $\alpha = 35°$, the bed roughness is much higher than the sidewall roughness. The dynamics of the core layer is strongly affected by the KBC at the bed that induced high values of the granular temperature, T, and a more sheared flow, with respect to the smooth bed. When the flow depth increases, due to the higher confining effect of the normal pressures, granular temperature decreases but only up to a certain distance from the basal surface, namely $\approx 5d \div 6d$ and $\approx 8d$ in case of sandpaper bed and granular bed, respectively. This distance can be regarded as a distance of influence of the rough bed. In fact, if the flow depth is higher than the distance of influence, the core region forms. Moreover, the linear trend of the velocity can be observed only far enough from the bed where the effect of the grain agitation induced by the basal roughness is much smaller. If the flow depth is smaller than the distance of influence of the rough bed, the shape of the velocity profile is concave all along the flow depth and the grains exhibits a more collisional behavior. In the experiments with $\alpha = 30°$, because of a lower inclination angle of the chute with respect

to the experiments with α = 35°, the normal pressures and the sidewall resistances are higher. The values of the granular temperature are globally lower and the KBC observed at the bed is of only weak grain rolling, in case of sandpaper beds, and no-slip and no-rolling, in case of granular bed. Granular temperature induced by the bed roughness generally plays a secondary role in determining the flow dynamics. Normal pressures and sidewall resistances are higher and a more frictional-collisional regime could take place. Due to different dissipation mechanisms with respect to the case of α = 35°, velocity profile shapes changed from a linear to a convex one.

In the upper region, with thickness of $\approx 2d \div 4d$, a more collisional regime can be observed in all the experiments. Volume fraction decreases while going toward the free surface and the shape of the velocity profiles is more concave. This reminds to the profiles observed in case of small flow depth, namely where the core region does not develop. Moreover, it is interesting to note that, when the mass flow rate is high, the grains tend to go toward the fixed bed exhibiting a maximum value of the downward velocity approximately in correspondence of the interface between the core layer and the upper collisional layer.

By looking at the free surface velocity profiles, one can observe the effect of the sidewall friction that induces an approximately parabolic shape of the longitudinal velocity profiles. If the mass flow rate is high enough, the grains tend to go toward the sidewalls. By looking at both the transverse velocity at the free surface and the vertical velocity at the sidewalls, it appears that a secondary circulation could take place in the upper collisional within the granular body. This occurs due to the high mass flow rate, namely due to the

high free surface velocities, which could induce momentum fluxes toward the sidewalls.

The experiments performed over erodible bed allowed studying uniform flows. They were carried out in two channels with a width of 8cm and 3cm, respectively. The same range of thickness of the flowing layer, h_{flow}, was investigated in order to analyze only the effect of a different channel width on the dynamics. By increasing h_{flow}, the inclination of the flowing layer increases due to sidewall friction, as shown by the relation found by Taberlet et al. (2003).

In both the experimental campaigns, the volume fraction profiles were very similar. Two regions can be distinguished: a core layer, with approximately constant values of the volume fraction and equal to ≈0.6, which develops from the erodible bed up to $\approx 4d \div 5d$ from the free surface and an upper collisional zone, where volume fraction is lower than 0.6 and velocity profiles are more concave.

In both the experimental campaigns, the longitudinal velocity profiles exhibited the typical shape already observed for this configuration by other experimental works: a lower convex shape and an upper linear shape. Moreover, it was found that the velocity profiles related to different runs collapse into a unique master velocity profile. This master profile is different in case of different channel width. The same can be said in case of granular temperature profiles. No modification of the profile shapes can be observed if the flow depth increases, as observed in the experiments over fixed bed. The only quantity that changes is the inclination angle of the flowing layer. Moreover, it increases with the mass flow rate. These interesting findings

provide that, in all the experiments, the granular flow finds its own equilibrium by only changing the inclination of the flowing layer. By comparing the master curves related to the two channels, we found that the master curve related to the narrow channel could be simply obtained by scaling the master curve of the 8cm-wise channel of a factor of ≈1.7. The scaling of the master curve is a very interesting result but needs to be confirmed by other experimental measurements in order to find an explanation on the physical meaning of the scaling factor.

The numerical integration performed in Chapt. 7 provided that the $\mu(I)$ rheology was capable to approximately reproduce the shapes of the velocity profiles both in uniform and steady flow conditions. However, some features of the granular flow dynamics, such as the collapse of the velocity profiles in case of uniform flow condition and the linearization of the velocity profiles in case of steady granular flows, were not fully captured by the model. This could be due to both the employed rheology and the approximations used for modelling the sidewall resistances. In fact, the $\mu(I)$ rheology does not take into account non-local effects, such as the force chains, which could arise in the granular body when the flow depth is high enough. Moreover, the rate-independent Coulomb law with a constant earth pressure coefficient used for modelling the sidewall resistances, could be too simplistic.

By concluding, the study of the dynamics of chute dry granular flows at laboratory scale highlights that different flow regimes may coexists. The joint information of the velocity and the volume fraction are necessary to better comprehend the dissipation mechanisms within a granular flow.

The basal roughness is a source of fluctuation kinetic energy and it strongly affects the shape of the velocity profiles. Therefore, further experimental campaigns should be performed in order better comprehend the role of both the granular temperature and the basal roughness. Specifically, it would be interesting to investigate higher inclination angles of the chute but also the shape of the bed roughness, which could probably affect the KBC at the bed. In case of erodible bed, it was found that the inclination of the flowing layer was probably the only flow quantity that represents all the dissipative forces occurring within the granular flows and at the boundaries. In fact, a master curve of the sidewall profiles was found and it probably depends only on the channel width. Therefore, in the future, more experiments should be carried out in channels of different width in order to check if there is a physically based relation between the channel width, namely the sidewall friction forces, and the shape of the sidewall velocity profile.

A small part of this research was conducted during my research period abroad and it was devoted to the study of granular flows at catchment scale. The study site was the Rebaixader catchment, located in the South Central Pyrenees. The monitoring station in the channelized zone was equipped with geophones, for measuring ground vibrations, a radar, for measuring flow depth and a rain gauge, to measure and detect precipitation. In the triggering zone, piezometer, soil moisture and suction sensors were buried into the soil along different verticals to monitor the rainfall infiltration.

Main goal of this research was to detect and classify all the processes occurred in 2017 in the study site in order to properly distinguish the triggering rainfalls. Three kinds of process were identified: debris flow

processes, *DBF*; fluvial sediment transport processes, *FST*; erosion and accumulation processes at the end of the scarp, *EAC*. The classification system was based on the ground vibrations and on the flow depths recorded by the geophones and the radar, respectively. The mean value of the impulses per minutes recorded by the two uppermost geophones was used to avoid false detection of a process. The maximum value of the impulses per second recorded by the lowermost sensor was used to detect a debris flow. The maximum value of the flow depth recorded by the radar was used to identify the other types of process that occurred in this catchment. This classification system, simply based on ground vibration and flow depth thresholds, was capable to capture the main characteristics of the processes during the propagation phase. Typical shapes of the flow depth time series can be related to each detected process. In case of *DBF* process, a "peak-tail" shape, corresponding to an abrupt increase and a subsequent long tail trend of the flow depth, was observed. In case of *FST* process, a "smooth increase-decrease" shape, which stands for a slightly increase of the flow height, was found for the two waves of sediment and water that characterize this process. In case of occurrence of *EAC* processes, no variation in the flow depth time series were observed since boulders and blocks stopped at the beginning of the propagation zone.

Rainfall data analysis was performed to provide preliminary information on the triggering rainfalls. A rainfall event was detected if the minimum amount of precipitation recorded by the rain gauge in 5 minutes was higher than 0.6mm. The rainfall event was characterized by using the maximum floating intensity, I_{max}, defined as the maximum value of the intensity evaluated on

floating time intervals of different durations *d* centred at a certain instant *t* between the beginning and the end of the precipitation. By comparing I_{max} with the maximum flow depth recorded by the radar during the occurrence of a process, we found that a higher rainfall intensity produces a higher flow height in the channel. Moreover, by choosing a threshold of ≈50 mm/h on the I_{max} evaluated on 5 minutes, it was possible to distinguish rainfall that triggered flow processes, namely *DBF* an *FST*, from the rainfall that did not trigger any process or *EAC* processes. This means that a relation between the occurrence of the process and the rainfall peak in this catchment could exists and I_{max} evaluated on 5 minutes could be one the most suitable parameter to characterize triggering precipitations. However, since the dataset is very small, these results can be considered only preliminary.

The soil remained in unsaturated condition during the whole observation period. The analysis of the volumetric water content (*VWC*) measurements focused on the detection of the *VWC* increments in order to find a relation between the occurrence of a process and an increase in soil moisture. We analyze also the response time of the sensors located along the same vertical. The response of the soil to a given rainfall event was different depending on the analyzed vertical. This could be probably due to the strong heterogeneity of the soil in the triggering zone, which induced the formation of preferential paths through which rainfall infiltrates. We found that most of the sensors recorded a *VWC* increase in case of occurrence of flow processes. However, not a clear relation between the *VWC* increase and the occurrence of a process was found.

An important result of the field study at catchment scale is the methodology

for the identification of different phenomena, as this is the base for the analysis of the link with the corresponding triggering rainfall. The analysis of the data recorded in this short observation period, provided useful indication for the further experimental campaigns. In fact, since the soil was found to be strongly heterogeneous, in the future, one could investigate more soil verticals and located in a wider area in order to better understand which main infiltration mechanisms of the rainfall occurs in the initiation zone of this catchment. Moreover, since the soil remained in unsaturated conditions in the whole observation period, one could focus only on suction and soil moisture measurements without installing any further piezometers.

References

[1] Abancó C., Hürlimann M., Fritschi B., Graf C., Moya J. (2012). Transformation of ground vibration signal for debris-flow monitoring and detection in alarm system. Sensors, v. 12, pp. 4870-4891.

[2] Abancó C., Hürlimann M., Moya J. (2014). Analysis of the ground vibration produced by debris flows and other torrential processes at the Rebaixader monitoring site (Catalan Pyrenees, Spain). Natural Hazards and Earth System Sciences, vol. 14, pp. 929-943.

[3] Ahn H., Brennen C. E., Sabersky R. H. (1991). Measurements of velocity, velocity fluctuation, density, and stresses in chute flows of granular materials. Journal of Applied Mechanics, v. 58(3), pp. 792-803.

[4] Ancey C. (2001a). Debris flows and related phenomena. In: Balmfort N., and Provenzale A., (eds.), Geomorphological Fluid Mechanics, Springer, Berlin Heidelberg, New York, pp. 528-547.

[5] Ancey C. (2001b). Dry granular flows down an inclined channel: Experimental investigations on the frictional-collisional regime. Physical Review E, v. 65(1), 011304.

[6] Ancey C., Coussot P., Evesque P. (1999). A theoretical framework for granular suspensions in a steady simple shear flow. Journal of Rheology, v. 43(6), pp. 1673-1699.

[7] Ancey C., Evesque P. (2000). Frictional-collisional regime for granular suspension flows down an inclined channel. Physical Review E., v. 62(6), 8349.

[8] Arattano M. (2000). On the use of seismic detectors as monitoring and warning system for debris flows. Natural Hazards, v. 20, pp. 197-213.

[9] Arattano M., Moia F. (1999). Monitoring the propagation of a debris flow along a torrent. Hydrological Sciences Journal, v. 44(5), pp. 811-823.

[10] Armanini A., Fraccarollo L., Larcher M. (2008). Liquid-granular channel flow dynamics. Powder Technology, v. 182(2), pp. 218-227.

[11] Armanini A., Capart H., Fraccarollo L., Larcher M. (2005). Rheological stratification in experimental free-surface flows of granular-liquid mixtures. Journal of Fluid Mechanics, v. 532, pp. 269-319.

[12] Artoni R., Richard P. (2015.) Effective wall friction in wall-bounded 3D dense granular flows. Physical Review Letters, v. 115(15), pp. 158001.

[13] Artoni R., Santomaso A., Canu P. (2009). Effective boundary conditions for dense granular flows. Physical Review E., v. 79(3), pp. 031304.

[14] Artoni R., Santomaso A. C., Go M., Canu P. (2012). Scaling laws for the slip velocity in dense granular flows. Physical Review Letters, v. 108(23), pp. 238002.

[15] Badoux A., Graf C., Rhyner J., Kuntner R., McArdell, B. W. (2009). A debris-flow alarm system for the Alpine Illgraben catchment: design and performance. Natural hazards, v. 49(3), pp. 517-539.

[16] Bagnold R. A. (1954). Experiments on a gravity-free dispersion of large solid spheres in a Newtonian fluid under shear. Proceedings of the Royal Society of London. Series A. Mathematical and Physical Sciences, v. 225(1160), pp. 49-63.

[17] Baker J. L., Barker T., Gray J. M. N. T. (2016). A two-dimensional depth averaged μ(I)-rheology for dense granular avalanches. Journal of Fluid Mechanics, v. 787, pp. 367-395.

[18] Barbolini M., Biancardi A. Natale L., Pagliardi M. (2005). A low cost system for the estimation of concentration and velocity profiles in rapid dry granular flows. Cold Regions Science and Technology, v. 43(1-2), pp. 49-61.

[19] Bel C., Liébault F., Navratil O., Eckert N., Bellot H., Fontaine F., Laigle D. (2017). Rainfall control of debris-flow triggering in the Réal Torrent, Southern French Prealps. Geomorphology, v. 291, pp. 17-32.

[20] Berti M., Genevois R., LaHusen R., Simoni A., Tecca P. R. (2000). Debris flow monitoring in the Acquabona Watershed on the Dolomites (Italian Alps). Physics and Chemistry of the Earth, Part B, Hydrology, Oceans and atmosphere, v. 25(9), pp. 707-715.

[21] Bonamy D., Daviaud F., Laurent L. (2002). Experimental study of granular surface flows via a fast camera: A continuous description. Physics of Fluids, v. 14(5), p. 1666.

[22] Brunetti M. T., Peruccacci S., Rossi M., Luciani S., Valigi D., Guzzetti F. (2010). Rainfall thresholds for the possible occurrence of landslides in Italy. Natural Hazards and Earth System Sciences, v. 10(3), pp. 447-458.

[23] Caine N. (1980). The rainfall intensity: duration control of shallow landslides and debris flows. Geografiska Annaler, Series A, Physical Geography, v. 62, pp. 23-27.

[24] Capart H., Young D. L., Zech Y. (2002). Voronoï imaging methods for the measurements of granular flows. Experiments in Fluids, v. 32, pp. 121-135.

[25] Carleo L., Sarno L., Papa M. N., Tai Y.-C., Villani P. (2018). Measurements of solid volume fraction and velocity in steady granular chute flows. (Submitted to Advanced Powder Technology).

[26] Chevoir F., Prochnow M., Moucheront P., da Cruz F., Bertrand F., Guilbaud J. P., Coussot P., Roux J. N. (2001). Dense granular flows in a vertical chute. In: Kishino Y., (ed.), Powder and Grains 2001, Balkema, Amsterdam, pp. 399-402.

[27] Coe J. A., Kinner D. A., Godt J. W. (2008). Initiation conditions fordebris flows generated by runoff at Chalk Cliffs, central Colorado. Geomorphology, v. 96, pp. 270-297.

[28] Comiti F., Marchi L., Macconi P., Arattano M., Bertoldi G., Borga M., Theule J. (2014). A new monitoring station for debris flows in the European Alps: first observations in the Gadria basin. Natural hazards, v. 73(3), pp. 1175-1198.

[29] Coussot P., Meunier M. (1996). Recognition, classification and mechanical description of debris flows. Earth-Science Review, v. 40, pp. 209-227.

[30] Coussot P., Laigle D., Arattano, M., Deganutti, A., Marchi L. (1998). Direct determination of rheological characteristics of debris flow. Journal of Hydraulic Engineering, v. 124(8), pp. 865-868.

[31] da Cruz F., Emam S., Prochnow M., Roux J. N., Chevoir F. (2005). Rheophysics of dense granular materials: Discrete simulation of plane shear flows. Physical Review E, v. 72(2), 021309.

[32] Delannay R., Valance A., Mangeney A. Roche O., Richard P. (2017). Granular and particle-laden flows: from laboratory experiments to field observations. Journal of Physics D: applied physics, v. 50(5), 053001.

[33] Doyle E. E., Hogg A. J., Mader H. M. (2010). A two-layer approach to modelling the transformation of dilute pyroclastic currents into dense pyroclastic flows. Proceedings of the Royal Society A: Mathematical, Physical and Engineering Sciences, v. 467(2129), pp. 1348–1371.

[34] Dunne T., Black R. D. (1970). An experimental investigation of runoff production in permeable soils. Water Resources Research, v. 6(2), pp. 478-490.

[35] Eckart W., Gray J. M. N. T., Hutter K. (2003). Particle Image Velocimetry (PIV) for granular avalanches on inclined planes. In: Hutter K., Kirchner N., (eds), Dynamic response of granular and porous materials under large catastrophic deformations. Lecture notes

in applied and computational mechanics, Springer, New York, v. 11, pp. 195-218.

[36] Fredlund D. G., Morgenstern N. R., Widger R. A. (1978). The shear strength of unsaturated soils. Canadian Geotechincal Journal, v. 15(3), pp. 313-321.

[37] GDR MiDi (2004). On dense granular flows. European Physical Journal, v. 14, pp. 341-365.

[38] Gray J. M. N. T., Wieland M., Hutter K. (1999). Gravity-driven free surface flow of granular avalanches over complex basal topography. Proceedings of the royal society of London. Series A: Mathematical, Physical and Engineering Sciences, v. 455, pp. 1841-1874.

[39] Gregoretti C., Fontana G. D. (2008). The triggering of debris flow due to channel-bed failure in some alpine headwater basins of the Dolomites: Analyses of critical runoff. Hydrological Processes: An International Journal, v. 22(13), pp. 2248-2263.

[40] Grudzień K., Niedostatkiewicz M., Adrien J., Tejchman J., Maire E. (2011). Quantitative estimation of volume changes of granular materials during silo flow using X-ray tomography. Chemical Engineering and Processing, v. 50(1), pp. 59-67.

[41] Guzzetti F., Peruccacci S., Rossi M., Stark C. P. (2007). Rainfall thresholds for the initiation of landslides in central and southern Europe. Meteorology and Atmospheric Physics, v. 98, pp. 239-267.

[42] Heiser M., Scheidl C., Eisl J., Spangl B., Hüb, J. (2015). Process type identification in torrential catchments in the eastern Alps. Geomorphology, v. 232, pp. 239-247.

[43] Horton R. E. (1933). The role of infiltration in the hydrological cycle. Transactions of the American Geophysical Union, v. 14, pp. 446-460.

[44] Hürlimann, M., Abancó, C., Moya, J., Raimat, C., Luis-Fonseca R. (2011) Debris-flow monitoring stations in the Eastern Pyrenees. Description of instrumentation, first experiences and preliminary results. In: Genevois R., Hamilton D. L. , Prestininzi A., (eds.), 5th International Conference on Debris-Flow Hazards Mitigation: Mechanics, Prediction and Assessment. La Sapienza Unniversity, Roma, pp. 553–562

[45] Hürlimann M., Abancó C., Moya J. (2012). Rockfalls detached from a lateral moraine during spring season. 2010 and 2011 events observed at the Rebaixader debris flow monitoring site (Central Pyrenees, Spain). Landslides, v. 3, pp. 385–393.

[46] Hürlimann M., Abancó C., Moya J., Vilajosana I. (2014). Results and experiences gathered at the Rebaixader debris-flow monitoring site, Central Pyrenees, Spain. Landslides, v. 11(6), pp. 939–953.

[47] Hungr O. (1995). A model for the runout analysis of rapid flow slides, debris flows, and avalanches. Canadian Geotechnical Journal, v. 32(4), pp. 610-623.

[48] Hungr O., Leroueil S., Picarelli L. (2014). The Varnes classification of landslide types, an update. Landslide, v. 11(2), pp. 167-194.

[49] Hunt M. L., Zenit R., Campbell C. S., Brennen C. E. (2002). Revisiting the 1954 suspension experiments of R. A. Bagnold. Journal of Fluid Mechanics, v. 452, pp. 1-24.

[50] Hutter K., Siegel M., Savage S. B., Nohguchi Y. (1993). Two dimensional spreading of a granular avalanche down an inclined plane. Part I. Theory. Acta Mechanica, v. 100, pp. 37-68.

[51] Iverson R. M., Reid M. E., LaHusen, R. G. (1997). Debris-flow mobilization from landslides. Annual Review of Earth and Planetary Sciences, v. 25, pp. 85-138.

[52] Iverson R. M. (2000). Landslide triggering by rain infiltration. Water Resources Research, v. 36(7), pp. 1897-1910.

[53] Iverson R. M., Denlinger R. P. (2001). Flow of variably fluidized granular masses across three-dimensional terrain: 1. Coulomb mixture theory. Journal of Geophysical Research, v. 106(B1), pp. 537-552.

[54] Jenkins J. T., Savage S. B. (1983). A theory for the rapid flow of identical, smooth, nearly elastic, spherical particles. Journal of Fluid Mechanics, v. 130, pp. 187-202.

[55] Jesuthasan N., Baliga B. R., Savage S. B. (2006). Use of particle tracking velocimetry for measurements of granular flows: review and application. KONA Powder and Particle Journal, v. 24, pp. 15-26.

[56] Johnson P. C., Nott P., Jackson R. (1990). Frictional-collisional equations of motion for particulate flows and their application to chutes. Journal of Fluid Mechanics, v. 210, pp. 501-535.

[57] Jop P. (2015). Rheological properties of dense granular flows. Comptes rendus physique, v. 16(1), pp. 62-72.

[58] Jop P., Forterre Y., Pouliquen O. (2005). Crucial role of sidewalls in granular surface flows: consequences for the rheology. Journal of Fluid Mechanics, v. 541, pp. 167-162.

[59] Jop P., Forterre Y., Pouliquen O. (2006). A constitutive law for dense granular flows. Nature, v. 441, pp. 727-730.

[60] Keane R. D., Adrian R. J. (1990). Optimization of particle image velocimeters. Part I: Double pulsed systems. Measurement Science and Technology, v. 1, pp. 1202-1215.

[61] Krahn J., Fredlund D. G., Klassen G. M. (1989). Effect of soil suction on slope stability at notch hill. Canadian Geotechnical Journal, v. 26, pp. 269-278.

[62] Kobayashi T., Saga T., Segawa S. (1989). Multipoint velocity measurement for unsteady flow field by digital image processing. In: Reznicek R. (ed.), Flow Visualization V, Hemisphere, New York, pp. 197-202.

[63] Komatsu T. S., Inagaki S., Nakagawa N., Nasuno S. (2001). Creep motion in a granular pile exhibiting steady surface flow. Physical Review Letters, v. 86(9), p. 1757.

[64] LaHusen R. (2005). Debris-flow instrumentation. In: Jakob M., Hungr O., (eds), Debris-flow hazards and related phenomena, Springer, Berlin, pp. 291-304.

[65] Laigle D., Coussot P. (1997). Numerical modeling of mudflows. Journal of Hydraulic Engineering, v. 123(7), pp. 617-623.

[66] Lambe T. W., Whitman R. V. (1969). Soil mechanics. John Wiley, New York.

[67] Lanzoni S., Gregoretti C., Stancanelli L. M. (2017). Coarse-grained debris flow dynamics on erodible beds. Journal of Geophysical Research: Earth Surface, v. 122(3), pp. 592-614.

[68] Lueptow R. M., Akonur A., Shinbrot T. (2000). PIV for granular flows. Experiments in Fluids, v. 28(2), pp.183-186.

[69] Lun C. K. K., Savage S. B., Jeffrey D. J., Chepurniy N. (1984). Kinetic theories for granular flow: inelastic particles in Couette flow and slightly inelastic particles in a general flowfield. Journal of Fluid Mechanics, v. 140, pp. 223-256.

[70] Marchi L., Arattano M., Deganutti A. M. (2002). Ten years of debris-flow monitoring in the Moscardo Torrent (Italian Alps). Geomorphology, v. 46(1-2), pp. 1-17.

[71] McArdell B. W., Bartelt P. Kowalski J. (2007). Field observations of basal forces and fluid pore pressure in a debris flow. Geophysical Research Letters, v. 34(7).

[72] Mills P., Loggia D., Tixier M. (1999). Model for a stationary dense granula flow along an inclined wall. Europhysics Letters, v. 45(6), pp. 733-738.

[73] Mueth D. M., Debregeas G. F., Karczmar G. S., Eng P. J., Nagel S. R., Jaeger H. M. (2000). Signatures of granular microstructure in dense shar flows. Nature, v. 406, pp. 385-389.

[74] Nakagawa M, Altobelli S. A., Caprihan A., Fukushima E., Jeong E.-K. (1993). Non-invasive measurements of granular flows by magnetic resonance imaging. Experiments in Fluids, v. 16, pp. 54-60.

[75] Nedderman R. M., Tuzun U., Savage S. B., Houlsby G. T. (1982). The flow of granular materials—I: Discharge rates from hoppers. Chemical Engineering Science, v. 37(11), pp. 1597-1609.

[76] Ng C. W. W., Shi Q. (1998). A numerical investigation of the stability of unsaturated soil slopes subjected to transient seepage. Computer and Geotechnics, v. 22(1), pp. 1-28.

[77] O'Brien J. S., Julien, P. Y. (1985). Physical properties and mechanics of hyperconcentrated sediment flows. In: D. S. Bowles, (ed.), Specialty conference paper, Delineations of landslide, flashflood, and debris flow hazards in Utah, Logan, Utah, pp. 260-279.

[78] Pouliquen O., Gutfraind R. (1996). Stress fluctuations and shear zones in quasistatic granular chute flows. Physical Review E., v. 53(1), p. 552.

[79] Pouliquen O. (1999). Scaling laws in granular flows down rough inclined planes. Physics of Fluids, v. 11(3), pp. 542.

[80] Pudasaini S. P., Hsiau S.-S., Wang Y., Hutter K. (2005). Velocity measurements in dry granular avalanches using particle image velocimetry technique and comparison with theoretical predictions. Physics of Fluids, v. 17(9), 093301.

[81] Rahardjo H., Lim T. T., Chang M. F., Fredlund D.G. (1995). Shear-strength characteristics of a residual soil. Canadian Geotechnical Journal, v. 32(1), pp. 60-77.

[82] Rickenmann D., Laigle D., McArdell B. W., Hübl J. (2006). Comparison of 2D debris-flow simulation models with field events. Computational Geosciences, v. 10(2), pp. 241-264.

[83] Sarno L., Papa M. N., Martino R. (2011). Dam-break flows of dry granular materials on gentle slopes. In: 5th Int. Conf. on Debris-Flow

Hazards Mitigation: Mechanics, Prediction and Assessment. Casa Editrice Università La Sapienza, Rome, pp. 503-512.

[84] Sarno L., Carravetta A., Martino R., Tai Y.-C. (2013). Pressure coefficient in dam-break flows of dry granular matter. Journal of Hydraulic Engineering, v. 139(11), pp. 1126-1133.

[85] Sarno L., Carravetta A., Martino R., Tai Y.-C. (2014). A two-layer depth averaged approach to describe the regime stratification in collapses of dry granular columns. Physics of Fluids, v. 26(10), 103303.

[86] Sarno L., Papa M. N., Villani P., Tai Y.-C. (2016). An optical method for measuring the near-wall volume fraction in granular dispersions. Granular Matter, v. 18(4), p. 80.

[87] Sarno L., Carleo L., Papa M. N., Villani P. (2018a). Experimental investigation on the effects of the fixed boundaries in channelized dry granular flows. Rock Mechanics and Rock Engineering, v. 51(1), pp. 203-225.

[88] Sarno L., Carravetta A., Tai Y. C., Martino R., Papa M. N., Kuo C. Y. (2018b). Measuring the velocity fields of granular flows–Employment of a multi-pass two-dimensional particle image velocimetry (2D-PIV) approach. Advanced Powder Technology, v. 29(12), pp. 3107-3123.

[89] Savage S. B. (1979). Gravity flow of cohesionless granular materials in chutes and channels. Journal of Fluid Mechanics, v. 92(1), pp. 53-96.

[90] Savage S. B. (1984). The mechanics of rapid granular flows. Advances in Applied Mechanics, v. 24, pp. 289-366.

[91] Savage S. B., Hutter K. (1989). The motion of a finite mass of granular material down a rough incline. Journal of Fluid Mechanics, v. 199, pp. 177-215.

[92] Savage S. B., Hutter K. (1991). The dynamics of avalanches of granular materials from initiation to runout. Part I: Analysis. Acta Mechanica, v. 86(1–4), pp. 201-223.

[93] Savage W., Baum R. (2005). Instability of steep slopes. In: Debris-flow Hazards and Related Phenomena. Springer Praxis Books. Springer, Berlin, Heidelberg.

[94] Schofield A., Wroth P. (1968). Critical state soil mechanics. London, McGraw-Hill.

[95] Sheng L.-T., Kuo C.-Y., Tai Y.-C., Hsiau S.-S. (2011). Indirect measurements of streamwise solid fraction variations of granular flows accelerating down a smooth rectangular chute. Experiments in Fluids, v. 51, pp. 1329-1342.

[96] Spinewine B., Capart H., Larcher M., Zech Y. (2003). Three-dimensional Voronoï imaging methods for the measurement of near-wall particulate flows. Experiments in Fluids, v. 34, pp. 227-241.

[97] Spinewine B., Capart H., Fraccarollo L., Larcher M. (2011). Laser stripe measurements of near-wall solid fraction in channel flows of liquid-granular mixtures. Experiments in Fluids, v. 50(6), pp. 1507-1525.

[98] Taberlet N., Richard P., Valance A., Losert W., Pasini J. M., Jenkins J. T., Delannay R. (2003). Superstable granular heap in a thin channel. Physical Review Letters, v. 91(26), p. 264301.

[99] Takahashi T. (2014). Debris flow: mechanics, prediction and countermeasures (2nd edition). CRC press/Balkema, Taylor and Francis group, London, United Kingdom.

[100] Tarboton D. G., (2003). Rainfall Runoff Processes. Civil and Environmental Engineering Faculty Publications. Paper 2570.

[101] Taylor D. (1948). Fundamentals of soil mechanics. Chapman And Hall, Limited.; New York.

[102] Terzaghi K. (1943). Theoretical soil mechanics. John Wiley & Sons, New York.

[103] Thielicke W., Stamhuis E. J. (2014). PIVlab–Towards user-friendly, affordable and accurate digital particle image velocimetry in MATLAB. Journal of Open Research Software, v. 2(1), e30.

[104] Tognacca C., Bezzola G. R., Minor H. E. (2000). Threshold criterion for debris flow initiation due to channel bed failure. In: Wiezczorek G. F., Naeser N. D., (eds.), Debris-Flow Hazards Mitigation: Mechanics, Prediction, and Assessment, Balkema, Rotterdam, The Netherlands, pp. 89–97.

[105] Uemura T., Yamamoto F., and Ohmi K. (1989). A high speed algorithm of image analysis for real time measurement of two-dimensional velocity distribution. In: Khalighi B., Braun M., Freitas C., (eds.), Flow Visualization, ASME, NewYork, pp. 129-134.

[106] Varnes D. J. (1978). Slope movement types and processes. In: Schuster R. L., Krizek R. J., (eds.), Landslides, analysis and control, special report 172: Transportation research board, National Academy of Sciences, Washington D.C., pp. 11-33.

[107] Wieczorek G. F., Glade T. (2005). Climatic factors influencing occurrence of debris flows. In Debris-flow hazards and related phenomena. Springer, Berlin, Heidelberg, pp. 325-362.

[108] Willert C. E., Gharib M. (1991). Digital particle image velocimetry. Experiment in Fluids, v. 10(4), pp. 181–193.